POLITECNICO DI MILANO

Dipartimento di Ingegneria Aerospaziale
Doctoral Programme in Aerospace Engineering

Laboratory Hypersonic Jets

Doctoral Dissertation of:
Mohsen Mirzaei

Supervisor:
Prof. Marco Belan
Tutor:
Prof. Sergio Ricci
The Chair of the Doctoral Programme:
Prof. Luigi Vigevano

Year 2013/XXV cycle

Table of contents

List of Figures

Abstract

Context. The free hypersonic jets can be found in several technological applications and even in astrophysical observations. The astrophysical context is that of the jets issuing from Young Stellar Objects (YSOs). In the present dissertation the propagation of hypersonic jets in a laboratory vessel has been mainly studied.

Aims. In order to have a further insight into the jets from YSOs, a set of experiments is performed in the range of Mach numbers from 7 to 20 and for jet-to-ambient density ratios from 0.85 up to more than 100, using different gas species and observing jet lengths in the order of 100 initial radii or more. Exploiting the scalability of the hydrodynamic equations, we intend to reproduce the YSO jet behaviour as far as the diagnostic quantities as head velocities and elapsed times are concerned.

In some cases, we have made comparisons between our experimental results and the existing numerical ones and also made comparisons with the observed morphologies obtained by other research groups. Also the jet morphology after the impact at the end of the vessel and the interaction with the backward flow has been investigated.

Methods. In the experiments the gas pressure and temperature are increased by a fast, quasi isoentropic compression by means of a piston system coupled with de Laval nozzles; it is performed by means of special facilities where the jet Mach numbers (in the range of 10 to 20) and the jet to ambient density ratios (in the range of 0.1 up to values exceeding 100) can be set independently of each other, what permits the investigation of a wide parameter range in the relevant physics. The visualizations and measurements are based on the electron beam technique: the jets are weakly ionized, and then a fast camera captures fluorescent images. Indications about the jets propagation and their resulting morphologies are obtained by means of several image processing techniques carried out on fluorescent images in order to denoising and measurement.

Results. Our experimental results in long scale jets, owing to their originality, could be served as a benchmark for existing and future numerical simulations and also a reference for future experimental investigation on the long scale jets. These results, showing the collimated jet flow, has given an answer to the famous issue of the jet morphology: " the jet shape, including the pumping phenomena, is just due to fluid dynamics and does not require magnetic confinement, periodic energy pumping or any other complex causes". In some cases the results are compared with the existing numerical simulations, and their agreements, included the jet head advance speed, the formation of knots, the travelling structures after the jet impact with the vessel end, and also their density distribution, are fairly good in the majority of comparisons.

Conclusions. Pressure-matched hypersonic jets maintain their collimation for long distances in terms of the initial jet radii, without including magnetic effects,

leading to a qualitative good agreement with the observed YSO jets morphologies. Also their evolution with regard to the effective variables, the combination of the Mach number and density ratio, has allowed the global morphologies.

Chapter 1

1. Introduction

The free hypersonic jet flow is the name given to the fluid dynamics phenomenon produced by a jet exhausting with a hypersonic velocity in the unbounded stationary surrounding medium.
In the last decades, hypersonic jets have received much interest from researchers because of their importance both in basic fluid dynamics and in applications for aeronautical and mechanical industries. One industrial sample of hypersonic jets is high speed compressible flows inside a scramjet. Scramjet is the proposed engine design for propelling aircrafts to hypersonic speeds. The engine has no moving parts as with the ramjet, with the added distinction that the flow through the engine remains supersonic. This flow is considered as an under expanded jet resulting from a high-pressure reservoir exhausting into a low-pressure quiescent environment [1,2].

In the natural phenomena also we have this kind of flow which is more interesting for astrophysics; Highly-collimated, oppositely directed jets are observed to originate from a variety of astrophysical. Young stars are the case of these astrophysical phenomena which are characterized by a rich and peculiar morphology. These compact objects and galactic supermassive black holes often generate astrophysical jets. These are narrow, complex projection flows along which mass, momentum, energy, and magnetic flux are transported through the ambient, either in the interstellar or the intergalactic medium. They display different luminosities, from the most powerful examples that have been observed to emerge from Active Galactic Nuclei (AGNs) down to the jets associated with low-mass young stellar objects within our own Galaxy [3,4,5,6], see figure 1.1 and figure 1.2. In astrophysics, there is a consensus about a common set of morphological properties, which are shared by most of these outflows, despite their physical scales and power differing by many orders of magnitude, from young stellar objects to neutron stars and black holes, to active galactic nuclei.
Images obtained with the Hubble Space Telescope have revealed intricate details in high Mach number gas dynamical flows of astrophysical jets [7], including shock wave patterns and Kelvin-Helmholtz vortex roll up.

Recent reviews of the observational and structural properties of the YSO jets can be found in Reipurth and Bally [8] (see also de Gouveia Dal Pino[9]; Reipurth, 1999[10]; de Gouveia Dal Pino and Cerqueira[11]; Raga et al. [12]; de Gouveia Dal Pino et al.[13]; Cerqueira and de Gouveia Dal Pino[14]). Reviews of the properties of the AGN jets and the relativistic galactic jets from X-ray binaries and micro quasars are presented in, e.g., Shibata [15], Pringle [16], Livio[17,18], Mirabel and Rodriguez [19,20], and Massaglia[21].

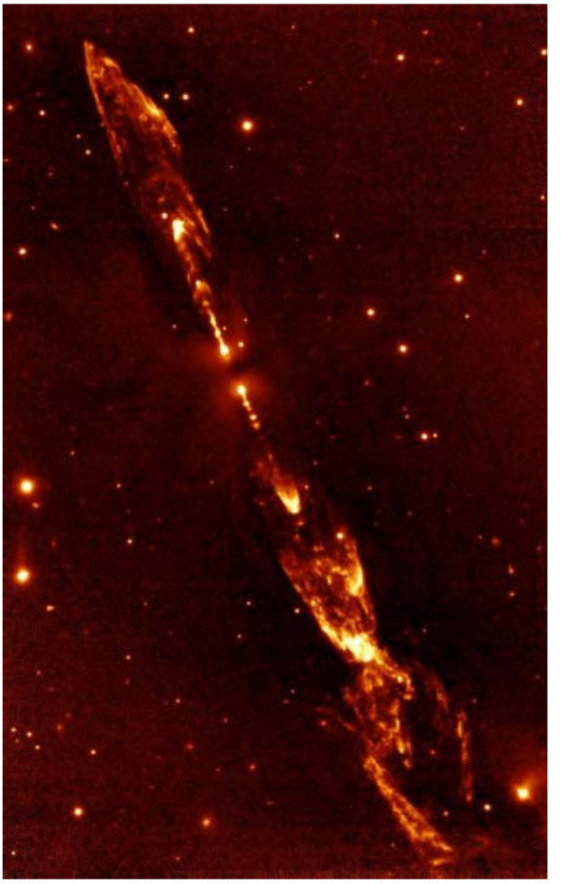

Figure 1.1: The HH212 jet, imaged in the $\lambda = 2.122 \mu m$ emission line of $H_2$with the VLT[22].

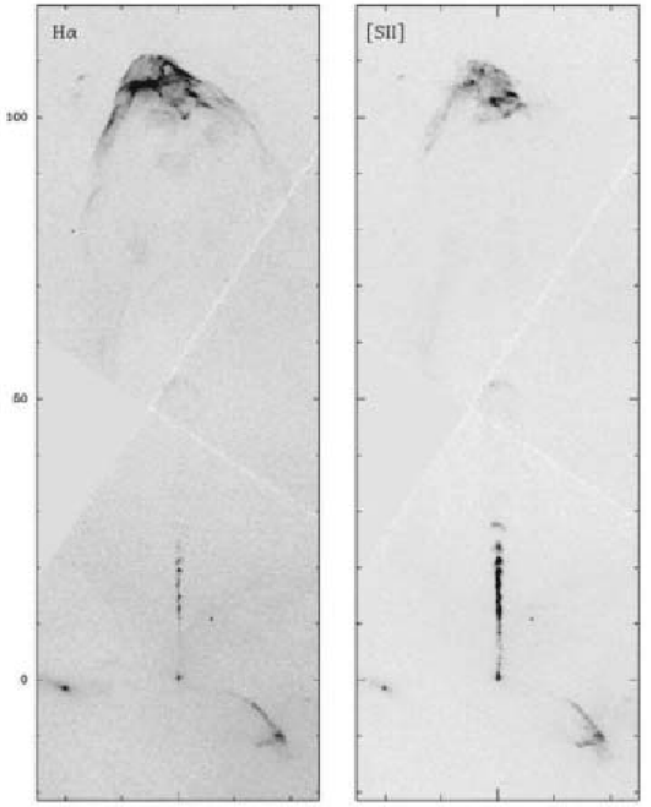

Figure 1.2: The YSO jet HH 34. Reproduced from Reipurth et al [23].

Recent theories and calculations [24] imply that the jets might also play a principal role in the explosion of core collapse supernovae. The observations of core collapse supernovae provide evidence that the explosion is intrinsically asymmetric.

All these observations have shown that astrophysical jets are collimated, having a sequence of bright high density regions (a chain of more or less regularly spaced emission knots) and may end in intense radiation emission areas (with line emission in the case of YSO jets and synchrotron continuum emission in the hot-spots of FRII radio jets). The latter are the regions where the jets impact against the ambient medium, and are called “working surface” in the jet literature.

There are many facets of jets which are not yet fully understood; in particular the processes by which the strongly collimated flows are driven. This has important implications for the range of jets and the manner in which their material and energy content is deposited, as well as for the entrainment and acceleration of material in their envelopes.

Evidence of accretion of matter onto central compact gravitating objects via an accretion disk suggests that the jets may have a common origin. The mechanism proposed for jet acceleration requires the crucial contribution of magnetic fields. In the case of AGN jets, it is expected that the fraction of energy flux due to magnetic fields dominates over the kinetic energy flux in the initial regions of the jet only. Stability issues and observations imply that they become mass dominated further out (Sikora et al 2005[25], Giannios and Spruit 2006 [26]).

Khokhlov[27] has developed an explosion model which assumes that bi-polar, non-relativistic jets form via a magneto-rotational mechanism during a core collapse, and these results in the production of a highly asymmetric supernova envelope.

Simulations at high Mach numbers are essential for achieving a detailed agreement with the astrophysical observations. The gas flows in the HH 1–2 astrophysical jets [28] are at about Mach 80, and other astrophysical jets are at even higher Mach numbers.

Numerical simulations [29,30]at high Mach numbers (up to 80) with radiative cooling have been performed to provide physical insights into these flows.

In the astrophysical setting, sometimes the jet gas is on the order of ten times the density of the ambient gas (heavy jets). These heavy jets (which are nearly "ballistic") are simulated by Youngsoo Ha · Carl L. Gardner [31]. In their investigation, the evolution of high Mach number astrophysical jets with radiative cooling using a positive scheme is simulated.

Another numerical simulation has done by Radulescu and Law [32] who simulated under-expanded jets. Under-expanded jets occur when a high-pressure gas suddenly discharges into a lower-pressure gas through an orifice or nozzle. They have studied the hydrodynamic evolution of highly under-expanded jets and formulated an approximate similarity solution for the jet evolution in a short scale jet. The used parameters in their simulations correspond to the release of pressurized hydrogen gas into ambient air, with pressure ratios varying between approximately 100 and 1000 and their simulations confirm the similarity laws derived theoretically and indicate that the head of the jet is laminar at early stages, while complex acoustic instabilities are established at the sides of the jet, involving shock interactions within the vortex rings, in good agreement with previous experimental findings.

The literature about these topics is huge from the early works of Love et al. (NASA Tech Report R-6, 1959)[33] and Ashkenas and Sherman (in Rarefied gas dynamics, Academic, NY, 1966)[34] to the innumerable papers published today[5,35,36,37], because of the numerous attempts to simulate numerically the stellar jets known from direct observations.

However, simulations can never fully capture the detail of a physical system. Approximations are necessary to make the problem computationally tractable: the simulations have a finite resolution (and are often artificially limited to the gross symmetry of the problem), and many physical processes must either be assumed to not be relevant or be treated by very approximate methods. The initial and

boundary conditions are also often poorly constrained by observation: the jet source may vary in speed or mass input rate, and the surrounding medium may be highly structured.
On the other hand, also there are several experimental results in hypersonic jets, dealing in general with short jets involving magneto-hydrodynamics effects, as pulsed, short convergent flows of plasma [38], or plasma jets created by laser ablation of shaped targets [39, 45].
An experimental platform using the Omega laser [40] to generate astrophysically relevant jets has been developed to better understand the physics of jets. Kauffman et al[41]andLindl[42] used a laser-heated hollow cylindrical gold hohlraumto radioactively drive the targets. However, axial plasma stagnation within the hologram generates additional pressure on the target which perturbs the hydrodynamics of the jet because of using the direct laser drive. There is also another experiment at Omega, which developed large field-of view imaging at the Z pulsed-power facility (SNLA) using a monochromatic curved crystal imager [43]. This experimental configuration offers the exciting potential of increased effective spatial resolution.
Ampleford et al. [44] presented a laboratory technique to produce rotating convergent plasma jet flows which is a modification of the conical wire array z-pinch [45,46]. Angular momentum is believed to be an integral part of the dynamics of proto-stellar jets, so this new technique has done to introduce angular momentum into radiativelycooled, highly supersonic jets in the laboratory.
The presence of angular momentum results in a hollow density profile in both the standing conical shock and the jet and the results indicates that the presence of rotation significantly affects the dynamics of both the jet forming shock and the jet, most notably producing a hollow density profile.
Almost all these experiments have been performed for short scale jet flows and done research reveal a need for experimental studies of free hypersonic jets on long scales.
In hypersonic jets, several physical parameters, expressed as non-dimensional similarity numbers, affect the physical behaviour; in the long term evolution, Mach number, jet-to-ambient density ratio, Reynolds number and heat flow numbers are in general important. In particular, in a stellar jet Reynolds number and temperatures can reach huge values, impossible to scale in a laboratory, whilst the other crucial parameters, namely the Mach number and the jet-to-ambient density ratio, can be matched in a real experiment. Here we have focused our investigation on these two crucial parameters that describe the hydrodynamics of YSO jets, i.e. the Mach number M and the density ratio η.
The present research project is mainly devoted to visualizations and measurements on hypersonic jets, in such a way as similar to natural phenomena, i.e. the stellar jets known in astrophysics, extending on length scales in the order of hundreds of initial diameters and travelling in a medium not necessarily made of the same gas of the jets.

The used experimental apparatus is the evolution of an existing system successfully employed in studies on strongly under expanded supersonic jets and rarefied flows [47,48] which produces the jets by means of a fast piston coupled with de Laval nozzles.
By our experiment, the Mach number M and the jet to ambient density ratio $\eta = \rho_j/\rho_a$ can be set independently each other to find the effect of each parameter on the jet behaviour. The Mach number of the jets ranges for 5, 10 and 20; the density ratio η, which plays an important role in the jets morphology, can be set from 0.1 up to values exceeding 100. These two parameters are in similitude with astrophysics parameters in the hydrodynamic limit. As a consequence of the setup, the Reynolds number cannot be set independently; it ranges from $1.7\times10^5$to 5×10^5.
A long-standing issue about stellar jets was also the possible effect of magnetic fields on the jets morphology, but this problem is not considered in the present study because our experiment has been designed to investigate the universal phenomenology in Newtonian dynamics, regardless of the presence of electromagnetic forces. So the originality of these results is outstanding; they have given an answer to the famous issue of the jet morphology: "Is the jet shape due just to fluid dynamics or it requires magnetic confinement, periodic energy pumping and other complex cases?". These results could serve also as a benchmark for existing and future numerical simulations.
The plan of this dissertation is as follows: in chapter 2 the physics of Hypersonic jets is presented, chapter 3 is about the experimental apparatus setup, chapter 4 is dedicated to visualizations and measurement techniques, chapter 5 gives some selected experimental results and the conclusions are drawn in chapter 6.

Chapter 2

2. The Physics of hypersonic jets

Many physical relationships in engineering and especially in aerodynamics are, by nature, extremely complex. It is much more complicated for astrophysical jets that are impossible to reproduce in any laboratory. In these cases often a phenomenon is too hard to find the relationship between variables, so dimensional analysis is used to identify variables which can be combined in groups which are definitely related. Experiments can then be completed to find this relationship between these groups and allow determination of the actual performance characteristics of real world systems.

Dimensional analysis is a remarkable tool in so far as it can be applied to any and every quantitative model or data set; recent applications include the most fundamental theories of physics. The results of dimensional analysis can be of greater or lesser value. It is most useful, indeed almost indispensable, for problems having no solvable theory. Dimensional analysis can always make a little progress towards a solution, and some of these, the universal spectrum of inertial-range turbulence and the log-layer profile of a turbulent boundary layer, are landmarks in fluid mechanics.

2.1. Dimensional analysis for hypersonic jet flow

This part describes a three-step procedure of dimensional analysis to be applied to all quantitative models and data sets of hypersonic jet flows. In order to introduce the physical independent and effective parameters on the jet flow, we consider a jet, issuing from a nozzle to surrounding ambient,which is observed at a specific distance from the nozzle exit. The first step of the analysis is beginning by listing the variables presuming relevant to the aspect of the jet.

2.1.1. Effective Physical Variables on the Jet Flow

When the velocity in the flow is greater than the sound speed (M > 1) important qualitative changes in the flow occur. A prominent change is the occurrence of the shock waves. The strength of the shock is also proportional to the flow velocity. So the most important parameter should be the jet velocity; its velocity in the jet source (nozzle exit) is considered as the first parameter.
There is a consensus about a common set of morphological properties of hypersonic jets, which are shared by most of these outflows, despite their physical scales and power differing by many orders of magnitude; if the jet comes from a small orifice or the exhaust of supersonic aircraft or from a stellar object, the kinetic power is remarkably different, so the jet size is a significant variable and can be represented by the jet diameter at the source; D.
In hypersonic jets,when the jet pressure is mismatched with the ambient pressure, there is a remarkable change in the flow structure [1, 22, 23]. If the pressure of surrounding gas is highly different from jet pressure, surrounding medium is unable to equalize the upstream pressure due to the very highly jet velocity. Therefore it is probable the exiting gas pressure goes significantly below or very greatly above ambient pressure, leading to under or over expanded jets; these conditions play a more significant role for the long term jet flows than short term ones[it is explained in 2.2.1]. Hence jet and ambient pressures are other important parameters influencing on the jet flow. Figure 2.1 shows a basic schematic of the jet morphology; the jet ends at a working surface, where impact against the ambient medium.

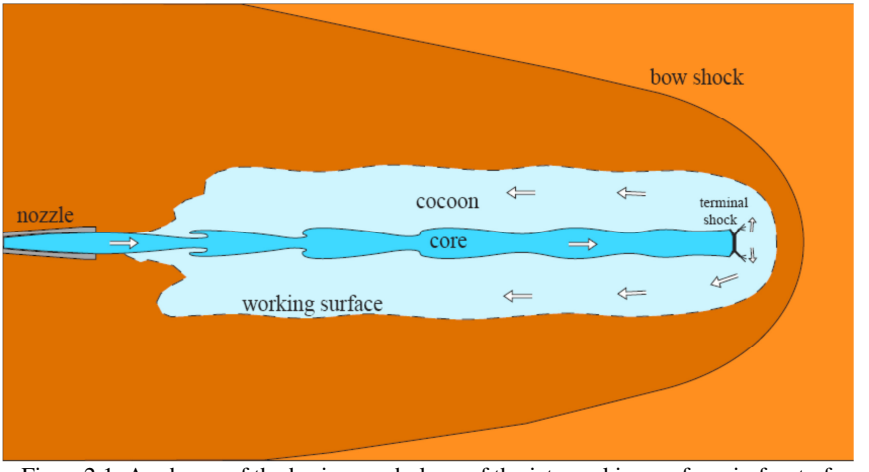

Figure2.1: A scheme of the basic morphology of the jet; working surface, in front of shacked jet, compressed gas feeds a backward flow along the sides of the jet.

The working surface of the jet moves outward with respect to the nozzle exit and enters the surrounding ambient and pulls over the ambient gas. Ambient medium resists against the jet flow; so if the ambient is lighter than the jet gas, there is less resistance against the jet motion,and for the heavier ambient there is more resistant. This opposition between the jet gas and ambient medium can change the jet shape. It means ambient and jet densities are two other affective variables in the jet morphology.

The strength of the shocks and jet kinetic energy slow down with increasing distances from the outflow source, also the viscosity around the jet boundaries damps and distorts the jetcollimation. Hence the jet shape is presumed to be a function of the jet length, and this effect is denoted by L; jet length from the outflow source. The reason for decreasing kinetic energy of the jet flow is due to overcomingover viscosity energy on the boundaries. Therefore the effect of the flow viscosity, shown by μ, is another noticeable parameter.

About gravity; this would be important for the low speed and also highly heavy jets (such as liquid jet into the gas ambient), because in these cases gravitational energy bends the jet path toward the gravitational source. But when the jet velocity is high, kinetic energy overcomes the gravitational energy and doesn't affect on the jet morphology. In our case, laboratory hypersonic jet, which velocity is very high and density ratio is not so high (almost less than 100), gravity effect is negligible.

There are a lot of aerodynamic phenomena in hypersonic jet flows which can be calculated by the thermodynamics formula, such as shock strength, shock thickness, and etc.which are a function of thegas type; monoatomic, diatomic, polyatomic. For instance pressure gradient in shocks is a function of specific heat ratio or adiabatic index ($\gamma=C_p/C_v$) which relates to the freedom degrees of a gas molecule (f) by the equation:

$$\gamma = \frac{f+2}{f} \qquad (2.1)$$

Monoatomic gas molecules possess only 3 translational degrees of freedom, while diatomic gases possess 3 translational and 2 rotational degrees of freedom at near standard conditions. In other words γis related to the gas type. Therefore the type of the jet gas is considered as the last affective variable on the jet flow and is denoted by γ; ratio of specific heats (adiabatic index).

All these variables are:

- V: Jet velocity
- D: jet diameter
- P_{jet}: jet pressure
- ρ_{jet}: jet density
- P_{amb}: ambient pressure
- ρ_{amb}: ambient density
- L: the distance from jet source

- μ: Jet gas viscosity
- Jet gas type: adiabatic index (γ)

The premise of dimensional analysis is that a complete equation made from this list of variables, will be independent of the choice of units. This leads to the second step, calculation of a null space basis of the corresponding dimensional.Any physical situation can be described by certain familiar properties e.g. length, velocity, pressure, temperature, etc. These are all known as dimensions. Of course dimensions are of no use without a magnitude being attached. It must be known more than that something has a length, it must also have a standardized unit - such as a meter, a foot, a yard etc. Dimensions are properties which can be measured. Units are the standard elements using to quantify these dimensions. In dimensional analysis only the nature of the dimension is concerned i.e. its quality not its quantity. The following common abbreviations are used:

Length = L
Mass = M
Time = T
Force = F
Temperature = Q

All the physical properties can be presented by L, T and one of M or F (F can be represented by a combination of LTM). These notes always use the LTM combination. The following table lists the dimensions of some common physical quantities which we need:

Table 2.1:Dimensions of some common physical quantities.

Quantity	SI Unit		Dimension
Length	M		L
Mass	Kg		M
Time	S		T
Velocity	m/s	ms^{-1}	LT^{-1}
Temperature	Joule J N m, kg m^2/s^2	kg m^2s^{-2}	ML^2T^{-2}
pressure	Pascal P, N/m^2, $kg/m/s^2$	Nm^{-2} kg $m^{-1}s^{-2}$	$ML^{-1}T^{-2}$
Density	kg/m^3	kg m^{-3}	ML^{-3}

specific weight	N/m^3 $kg/m^2/s^2$	$kg\ m^{-2}s^{-2}$	$ML^{-2}T^{-2}$
relative density	a ratio no units	.	1
Viscosity	$N\ s/m^2$ $kg/m\ s$	$N\ sm^{-2}$ $kg\ m^{-1}s^{-1}$	$M\ L^{-1}T^{-1}$
adiabatic index	a ratio no units	.	1

The non-dimensional variables are themselves a basis set and in most cases their form is not determined by dimensional analysis alone. Our goal is to convert all dimensional variables to non dimensional ones. So continue to third step.

The third and in some respects the most interesting step is to choose an optimal form for the basis set. A very useful strategy is to nondimensionalize the dependent variable by a physically motivated 'zero order' solution. When carried to completion, this leads naturally to a scaling analysis in which the non-dimensional variables of a model equation are O(1) in some relevant limit. The remaining nondimensional variables can then be formed in ways that define the geometry of the problem or that correspond to the ratios of terms in a model equation, e.g., the Reynolds number or Mach number often arises in models of aerodynamics.

Before doing any analysis, we seem to arrive at the conclusion that the jet shape depends on six quantities:

$$£ = \phi\ (V, D, P_{jet}, P_{amb}, \rho_{jet}, \rho_{amb,} L, \mu, \gamma) \qquad (2.2)$$

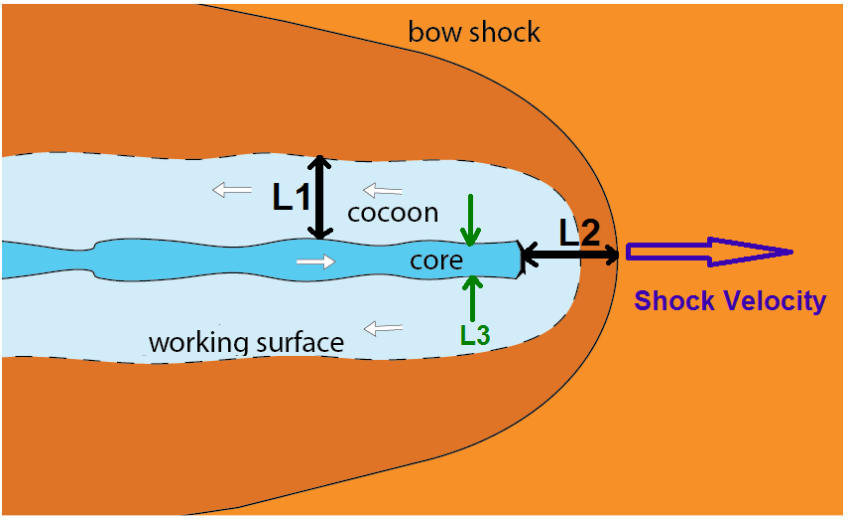

Figure2.2: Some physical measurable parameter to specify the behaviour of the working surface of the jet flow.

Where £ could be some physical measurable parameter to specify the behaviour of the working surface in the distance L from the jet source, such as jet head velocity, the angle of bow shock or some thicknesses to identify the shape of working surface; here £ is defined as L1 showing the thickness of cocoon or L2 illustrating the distance between the bow shock and terminal shock, or also L3 representing the beam width (see figure 2.2). The procedures for non dimensional analysis of head velocity and structures (L1, L2 or…) are almost the same, so here £ is considered as the length to specify the structure of the working surface.

Now Buckingham's π theorem is applied for nondimensionalization; The Buckingham π theorem gives a good generalized strategy for obtaining a solution as is outlined below.

A relationship between 9 variables (physical properties such as velocity, density etc.) can be expressed as a relationship between 9 non-dimensional groups of variables called π groups. Each π group is a function of n governing or repeating variables plus one of the remaining variables.

2.1.2. Selecting Repeating Variables

Repeating variables are those supposing to be appeared in all or most of the π groups, and are an influence in the problem. Before commencing analysis of the problem, one must choose the repeating variables. There is considerable freedom allowed in the choice.

From the 2nd theorem there can be n (= 3) repeating variables. The repeating variables should be chosen to be measurable in an experimental investigation and also to be of major interest. Here for laboratory hypersonic jet, we take P_{jet}, D and viscosity of the jet gas as the three repeating variables. This freedom of choice results in there being many different π groups which can be formed and all are valid. There is not really a wrong choice.
£=some thickness or length specifying the structure of the working surface
$£ = \phi (V, D, P_{jet}, P_{amb}, \rho_{jet}, \rho_{amb}, L, \mu, \gamma)$

So by combinations of these three repeating variables, each parameter is normalized by combination of other ones:

$$\Pi 1 = P_{jet}^{a1} D^{b1} \mu^{c1} \times V \quad (2.3)$$

$$\Pi 2 = P_{jet}^{a2} D^{b2} \mu^{c2} \times P_{amb} \quad (2.4)$$

$$\Pi 3 = P_{jet}^{a3} D^{b3} \mu^{c3} \times \rho_{jet} \quad (2.5)$$

$$\Pi 4 = P_{jet}^{a4} D^{b4} \mu^{c4} \times \rho_{amb} \quad (2.6)$$

$$\Pi 5 = P_{jet}^{a5} D^{b5} \mu^{c5} \times L \quad (2.7)$$

$$\Pi 6 = P_{jet}^{a6} D^{b6} \mu^{c6} \times \gamma \quad (2.8)$$

For the first group π1:

$$M^0L^0T^0 = [ML^{-1}T^{-2}]^{a1} \times [L]^{b1} \times [M L^{-1}T^{-1}]^{c1} \times [L T^{-1}] \quad (2.9)$$

For each dimension (M, L or T) the powers must be equal on both sides of the equation, so:
a1= -1, b1= -1, c1=1
Giving π_1 as; $P_{jet}^{-1} \times D^{-1} \times \mu^1 \times V$ or $\pi_1 = \frac{V \mu}{P_{jet} D}$ (2.10)

And a similar procedure is followed for the other π groups.
For π_2 group:

a2=-1, b2=0, c2=0
Giving π_2 as; $P_{jet}^{-1} \times D^0 \times \mu^0 \times P_{amb}$ or $\pi_2 = \frac{P_{amb}}{P_{jet}}$ (2.11)

For π_3 group:
A3=1, b3=2, c3=-2
Giving π_3 as; $P_{jet}^{1} \times D^2 \times \mu^{-2} \times \rho_{jet}$ or $\pi_3 = \frac{\rho_{jet} D^2 P_{jet}}{\mu^2}$ (2.12)

For π_4 group:

A4=1, b4=2, c4=-2
Giving π_4 as; $P_{jet}^{1} \times D^2 \times \mu^{-2} \times \rho_{amb}$ or $\pi_4 = \frac{\rho_{amb} D^2 P_{jet}}{\mu^2}$ (2.13)

For π_5 group:
A5=0, b5=-1, c5=0
Giving π_5 as; $P_{jet}^{0} \times D^{-1} \times \mu^0 \times L$ or $\pi_5 = \frac{L}{D}$ (2.14)

And finally for π_6 group:
a5=0, b5=0, c5=0
Giving π_6 as; $P_{jet}^{0} \times D^0 \times \mu^0 \times \gamma$ or $\pi_6 = \gamma$

Finally we can rewrite:

$$\pi_0 = £/D = £" = \phi(\pi_1, \pi_2, \pi_3, \pi_4, \pi_5, \pi_6) = \phi\left(\frac{V\mu}{P_{jet}D}, \frac{P_{amb}}{P_{jet}}, \frac{\rho_{jet} D^2 P_{jet}}{\mu^2}, \frac{\rho_{amb} D^2 P_{jet}}{\mu^2}, \frac{L}{D}, \gamma\right)$$

(2.15)

2.1.3. Manipulation of the π groups

Once the identified manipulation of the π groups is permitted, these manipulations do not change the number of involved groups, but may change their appearance drastically.
Taking the defining equation as: £"=ϕ (π_1 , π_2 , π_3 …… π_6)
Then the following manipulations are permitted:

1. Any number of groups can be combined by multiplication or division to form a new group which replaces one of the existing. For example π_1 and π_2 may be combined to form $\pi_{1a} = \pi_1 / \pi_2$ so the defining equation becomes
   £"=ϕ (π_{1a} , π_2 , π_3 … π_6)
2. The reciprocal of any dimensionless group is valid.
   So £"=ϕ (π_1 ,1/ π_2 , π_3 … $1/\pi_6$) is valid.
3. Any dimensionless group may be raised to any power.
   So £"=ϕ ($(\pi_1)^2$, $(\pi_2)^{1/2}$, $(\pi_3)^3$…… π_6) is valid.
4. Any dimensionless group may be multiplied by a constant.

In this step these manipulations are applied to obtain new and meaningful non-dimensional groups which are performed in the following formulas (2.16 to 2.22).

$$\pi_0 = £/D = £" = \phi(\pi_1, \pi_2, \pi_3, \pi_4, \pi_5, \pi_6) = \phi\left(\frac{V\mu}{P_{jet}D}, \frac{P_{amb}}{P_{jet}}, \frac{\rho_{jet} D^2 P_{jet}}{\mu^2}, \frac{\rho_{amb} D^2 P_{jet}}{\mu^2}, \frac{L}{D}, \gamma\right)$$

(2.16)

$$\pi_{1a} = \pi_1 \times \pi_3 \rightarrow \frac{\rho_{jet} V D}{\mu} \tag{2.17}$$

$$\pi_{2a} = \frac{1}{\pi_2} \tag{2.18}$$

$$\pi_{3a} = \frac{\pi_{1a}}{\sqrt{\pi_3 \pi_6}} \rightarrow \sqrt{\frac{V^2 \rho_{jet}}{\gamma P_{jet}}} \tag{2.19}$$

$$\pi_{4a} = \frac{\pi_3}{\pi_4} \rightarrow \frac{\rho_{jet}}{\rho_{amb}} \tag{2.20}$$

So:

$$£" = \phi\left(\frac{\rho_{jet} V D}{\mu}, \frac{P_{jet}}{P_{amb}}, \sqrt{\frac{V^2 \rho_{jet}}{\gamma P_{jet}}}, \frac{\rho_{jet}}{\rho_{amb}}, \frac{L}{D}, \gamma\right) \tag{2.21}$$

or:

$$£" = \phi\left(\mathrm{Re}, \frac{P_{jet}}{P_{amb}}, M, \frac{\rho_{jet}}{\rho_{amb}}, \frac{L}{D}, \gamma\right) \tag{2.22}$$

Here 9 independent variables have been reduced to 6 ones;

- Reynolds number: inertial over viscous force ratio
- Pressure ratio: jet to ambient pressure ratio
- Mach number: Local gas velocity over local sound speed in the surrounding medium
- Density ratio: jet to ambient density ratio
- Length scale number: jet length to jet diameter ratio
- Jet gas type: adiabatic index (γ)

The last π group, γ, indicating jet gas type, has a second order effect on the jet behaviour and if all jet gases are the same type, it will vanish. The used gases for all jets in our experiment are mono atomic; Helium, Argon and Xenon which γ is constant for all of them (γ=5/3). This condition leads to reduce the independent parameters to five one:

$$£" = \phi\left(\mathrm{Re}, \mathrm{K}, M, \eta, \frac{L}{D}\right) \tag{2.23}$$

Here η is density ratio ($\frac{\rho_{jet}}{\rho_{amb}}$) and K is the pressure ratio ($\frac{P_{jet}}{P_{amb}}$), all these independent non-dimensional parameters have a first order effect on jet flow. As mentioned in chapter one, there are several experimental works in laboratory hypersonic jets which almost all of them deal generally with short scale jets [36 - 44]; small L/D (about 10). Numerical simulations and direct observations of astrophysical jets prove that jet structures extend coherently up to long distance

but there is not any experimental study about long term hypersonic jets. In our research we have focused on the long scale jets which the jet length is in the order of hundred of its diameter. Hence the Length scale number (L/D) is limited in the specific range (long term jets);regarding this condition, the length scale number is vanished, and just Mach number, density ratio, pressure ratio, and Reynolds number are expressed as effective non-dimensional similarity numbers on the long term jet flow.
It is difficult to find the effect of all these groups on the experimental investigation of the jet morphology, therefore must limit ourselves to identify those groups that are the crucial ones in controlling the overall jet behaviour in order to rescale the laboratory simulations accordingly. In particular, in a stellar jet, Reynolds number can reach huge values [26], impossible to scale in a laboratory, whilst the other crucial parameters, namely the Mach number, density ratio and pressure ratio, can be matched in a real experiment. Hence in laboratory hypersonic jets, three non-dimensional parameters could be presented:
1. Mach number
2. Pressure ratio
3. Density ratio
So: £”=ϕ (K, η , M)

2.2. Reduction of the Main Non dimensional Parameters

This section focuses on the three main and effective non dimensional parameters on the jet morphology. In the following, the influence of pressure ratio is explained and the effect of Mach number and density ratio are clarified in the section 2.3.

2.2.1. Influence of pressure ratio; K

The jet is called under-expanded, when pressure ratio is greater than one (K>1) which means the jet pressure at the nozzle exit is greater than the ambient gas pressure. If K $\prec$ 1 it is over-expanded and if K=1, it is pressure matched.

2.2.1.1. Under Expanded Jet

In the laboratory a supersonic under expanded jet can be generated from a compressed gas exhausting from a nozzle into an environment with a lower static pressure [45,46]. When the jet pressure is more than ambient pressure, at the nozzle exit, the flow follows a Prandtl-Meyer expansion to match it with the surrounding gas, which makes it accelerate and turn away from the centreline. The

expansion waves, propagating throughout the jet, are reflected as compression waves from the constant-pressure free boundary. For small pressure ratios, the compression waves reflect from the free boundary into the new expansion waves, thereby giving rise to a multi-cell barrel-shaped structure [49, 50].
For higher pressure ratios, the compression waves coalesce to form an axisymmetric curved incident shock, which propagates across the centreline. The flow undergoes a double shock wave over a short distance, leading to a double pressure increase [1,50]. The first shock is called the incident shock and the second shock can be regarded as a "*reflected shock*" from the centreline.

2.2.1.1.1. Regular Reflections

Figure 2.3 shows the simulated flow structure of the jet for a slightly under-expanded supersonic. This complicated axisymmetric structure has several notable features. First, the jet boundary oscillates as the jet gas periodically over-expands and re-converges in its attempt to match the ambient pressure. The gas continually overshoots the equilibrium position because the effects of the boundary are communicated to the interior of the jet by sound waves, which, by definition, travel more slowly than the bulk supersonic flow. There is the second remarkable feature of the jet, formed by characteristic paths of the sound waves; the network of crisscrossed shock waves or shock diamonds. These standing shocks alternate with rarefaction fans (blue lines). The shades of blue in Figure 2.3 shows the gas in the jet interior expands and cools as it flows through the rarefaction fans and the shades of black indicates it is compressed and heats as it passes through the shock diamonds [51]. The figure clearly illustrates that the jet interior is always out of step with the jet boundary. For example, the positions of greatest gas compression do not coincide with the positions of minimum jet diameter. The streamlines in the figure 2.3 show the flow paths of the gas. The gas bends out toward the boundary by passing through rarefaction fans and bends back toward the axis by passing through shock fronts. The compression and expansion waves could occur periodically for a free jet. Figure 2.4 shows the formation of the shock structure in Figure 2.3 in terms of characteristics. As the gas issues the nozzle, it expands and causes to emanate the rarefaction fan (diverging blue characteristics) at the nozzle exit. When the gas over expands, the pressure of the ambient gas in the boundary pushes back the jet gas toward the axis, creating the black characteristics. This phenomenon leads to converging conical shock. When this so called incident shock reaches the jet axis it undergoesa regular reflection; that is, it forms a diverging shock. At the point where this reflected shock reaches the jet boundary, it knocks the boundary outward, creating a new rarefaction fan, and the process goes on [51].

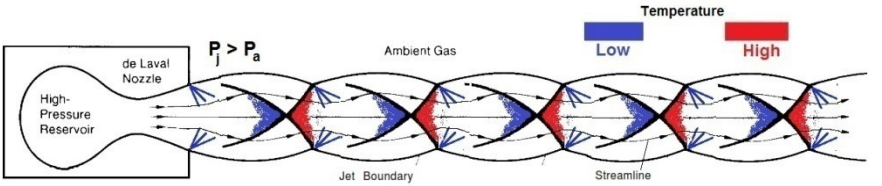

Figure 2.3: Idealized steady-state structure of slightly under expanded supersonic jet[51].

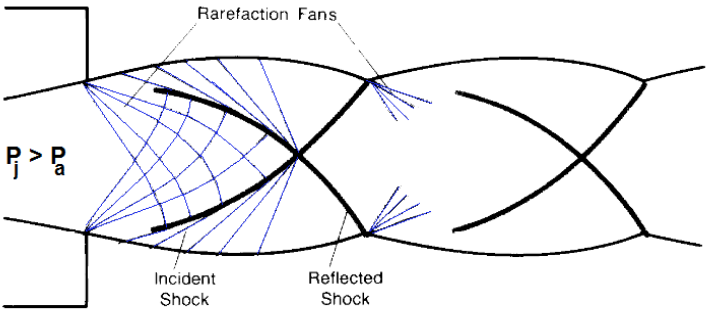

Figure 2.4: Regular reflection in a slightly under expanded jet.

2.2.1.1.2. Mach Reflections (high under expanded jet)

Sometimes there is a remarkable change in the flow structure when the pressure mismatch at the nozzle exit is too much (K>>1 or K<<1), as shown in figure 2.5.
For very large pressure ratio, the separating distance between the incident and the reflected shocks, decreases so much that a strong shock forms around the centerline, similar to a normal shock wave and called the Mach disk [1]. By considering the angle between the incident shock and the jet axis, the type of reflection can be determined: if the angles of incidence are small [52,53], it yields the regular reflections shown in Figures 2.3 and 2.4, and if it is large angle, yields Mach reflections shown in figure 2.5. As the gas crosses the shock, the velocity component normal to the shock is greatly reduced but its parallel component remains unchanged. So the shocks with large incidence angles are much stronger for slowing down the flow than shocks with small angles of incidence. The critical angle for transition from regular reflectionsto Mach reflections is approximately the angle that yields a sonic relative velocity of the gas downstream of the shock [53].
Downstream of the Mach disk, the flow becomes subsonic and the pressure is raised up approximately to the static ambient pressure. The subsonic core flow is

bounded by a slip stream emanating from the triple point and may or may not become supersonic again, depending on how strong the Mach disk is (see Figure 2.5). The slip streamline is where the flow velocity, density, and temperature are discontinuous across this contact surface (figure 2.5). This slip discontinuity arises because the thermodynamic pathway through the incident and reflected shocks does not equal the pathway through the Mach disk.

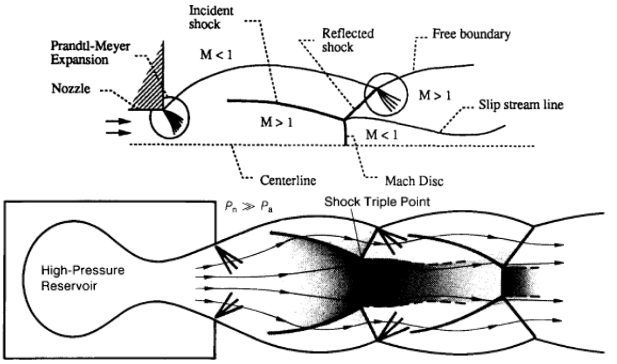

Figure 2.5: The under expanded jet for high pressure ratio (K>>1) [1].

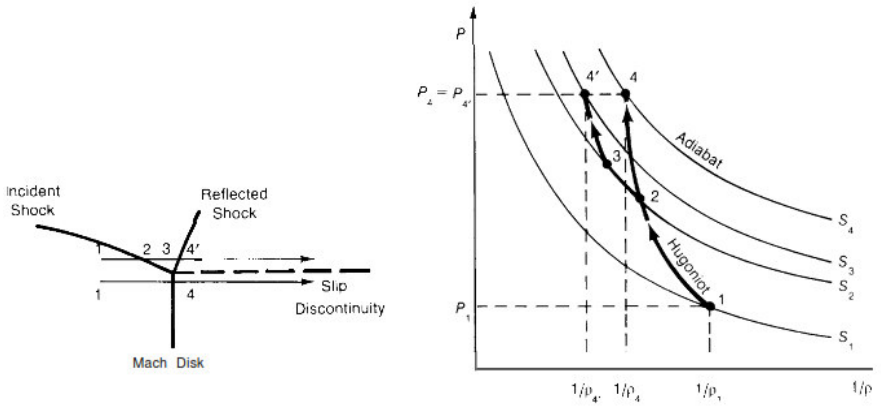

Figure 2.6: Shock Triple Point and its thermodynamic history [51].

Figure 2.6 shows two parallel streamlines passing through both sides of the shock triple point and their thermodynamics pathways is illustrated on the left side of the figure. Adjacent fluid elements at some initial point on either streamline have the same state variables and the same total (kinetic plus internal) specific energy, that is, energy per unit mass. This quantity is given by

$$\frac{1}{2}v^2 + \frac{\gamma}{\gamma-1}\frac{P}{\rho} \qquad (2.1)$$

According to the Bernoulli's principle, the total specific energy remains constant along a streamline, so if we follow both adjacent fluid elements arriving at points 4 and 4' in Figure 2.6, they must still have the same total specific energy and also the same pressure because they are still adjacent. However, from Figure 2.6 it is obvious that their densities and entropies are not the same. The fluid element at point 4 has passed shock-heated along a Hugoniot and reached to a higher entropy and lower density than the fluid element that passed through the incident and reflected shocks along points 2 and 3 to point 4'. The density of the fluid element at point 4 is lower than point 4' which implies that its internal energy (which is proportional to P/ρ) is greater than that of the fluid element at point 4'. Bernoulli's principle then implies that the fluid element at point 4 must have a correspondingly lower kinetic energy (flow velocity) than the adjacent element at point 4'. A slip discontinuity results from this difference in flow velocities [51].

2.2.1.2. Over Expanded Jets

In over expanded jets, the nozzle exit pressure is lower than the surrounding pressurewhich leads to the compression wave occurs at the nozzle exit, so the flow is inflexed and the pressure increase. Figure 2.7 shows idealizations of the jet structures. The numerical results [53, 54,55] and also experimental ones [56] confirmed the occurrence of Mach disk formation in high over expanded jet as well (figure 2.8 and 2.9).

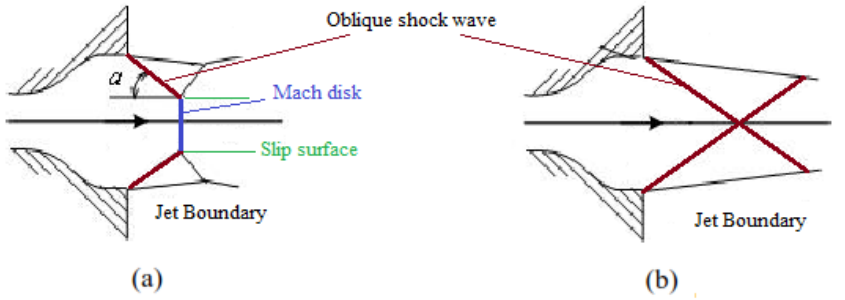

Figure 2.7: Schematics of jet structure of over expanded jet.

a)K<<1 b) K<1

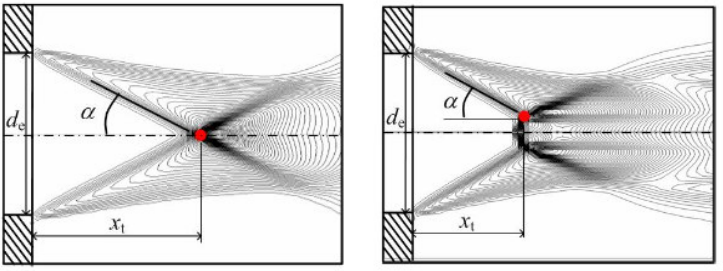

a) b)

Figure 2.8: Numerical simulation of over expanded at M=4[53];

a) K<1 b) K<<1

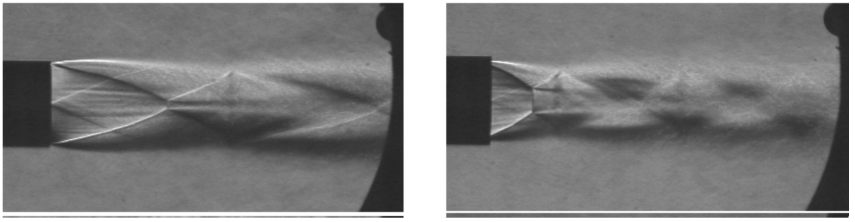

a) b)

Figure 2.9: Numerical simulation of over expanded at M=3 [56];

a) K=0.74 b) K=0.30

2.2.2. Laboratory Supersonic Jets

Figures 2.3, 2.4 and 2.7 show idealizations of the jet structures which here the real supersonic jets do not have sharp, stable boundaries but turbulent boundaries where jet and ambient gases are mixed.

In figure 2.10 a more realistic steady-state structure for an over expanded laboratory jet is shown; because of large pressure mismatches at the nozzle exit, Mach reflections occur, but further downstream the reflections are regular. Similarly, for an over-expanded jet, the compression and expansion waves occur, and pressure is increased due to compression, or decreased due to expansion.More downstream mixing layers, growing by Kelvin-Helmholtz (shear) instabilities, progressively are combined with the supersonic core of the jet and after a while this mixing layer reaches the jet axis and then the flow is fully turbulent and subsonic. It is then susceptible to twisting and bending motions, and in other

words the wave structures within the supersonic core are not steady since they are buffeted by the turbulent boundary layer [51].

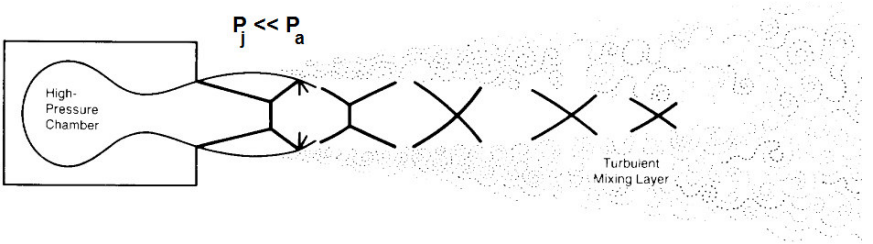

Figure 2.10:Realistic steady-state structure of an over expanded supersonic jet(K<<1) [51]

In this research, laboratory hypersonic jet, we have focused on long term jet lasting to hundreds of initial jet diameter, so if jet pressure is highly different from ambient pressure (K>>1 or K<<1) it will be distorted by mismatch conditions and cannot last to such a long distance. Also according to the astrophysical information taken from x-ray data from satellites, hot thermal gas pervades intergalactic space which in most cases is equal to the pressure confining the jets. Hence to have long scale laboratory hypersonic jet to simulate astrophysical jets, jet pressure is set to nearly ambient pressure; pressure ratio is fixed about unity (K≈1). This flow is called "*Nearly Matched jet flow*". By this assumption, another non-dimensional number vanishes and just two main numbers are considered as effective ones on "**long scale nearly matched hypersonic jet flow":** Mach number and Density ratio.

2.3. Jet Morphology

Figure 2.11 shows the simulation of hypersonic jet [51] which is well defined and started with the equations for compressible fluid flow; at t = 0 the jet gas escapes continuously through a narrow orifice into a region filled with static ambient and also the flow is assumed to be axisymmetric and non-swirling. So it reduces a three-dimensional problem to two dimensions. One interesting point about this kind of simulations is that it is scale-invariant, which means by changing the dimension (jet diameter), the results can be scaled from laboratory to cosmic dimensions. In this case four scale-invariant (dimensionless) parameters determine the flow; η, K, M and θ. The parameter θ is the opening angle of the jet at the source. For extragalactic jets which have small observed opening angles, it is considered to have a perfectly collimated beam jet at the source (θ=0) and also assumed that the jet gas pressure equals the ambient gas pressure (K=1). So just two remaining parameter set (M,η) defines a solution space. These parameters have scarcely been explored in the laboratory because of the difficulties of achieving very high Mach numbers (M > 10) and low density ratios (η<1). Hence

more explorations on this topic are in numerical simulations than experimental ones.
The jet flow is kind of two-fluid problem which critically depend on the motion of the interface separating boundaries and they are generally driven by shear motion parallel to the interface (subjected to Kelvin-Helmholtz instabilities), and also are driven by accelerations normal to the interface (subjected to Rayleigh-Taylor instabilities) [51]. These instabilities mix two fluids and can modify the jet flow significantly.

2.3.1. A Supersonic Jet Close up

Here the establishment and propagation of a pressure-matched supersonic jet is described according to the simulated jet shown in figure 2.11. This figure shows four snapshots in the time evolution of a low-density jet (η=0.1) at M= 3.

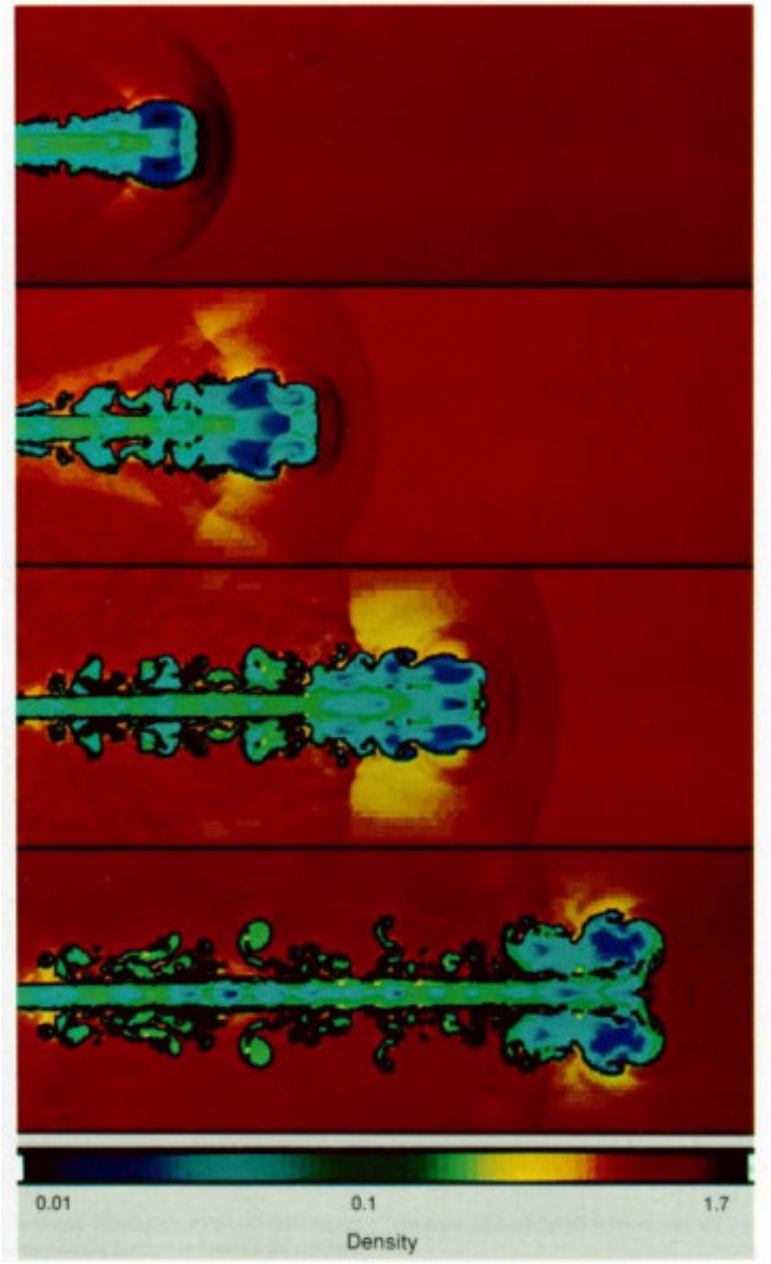

Figure 2.11: Numerical simulation of the time evolution of pressure matched axisymmetric supersonic jet; M=3 and η=0.1 [51].

As it is obvious by the colour-coded density value in these plots, the entire jet is significantly less dense than the ambient gas throughout its evolution. A novel aspect of such jets, already predicted by Blandford and Rees[56] is the establishment of a cocoon; a splashing backward gas from the jet head surrounding the central jet beam. The cocoon is visible in all instances of the jet evolution shown in figure 2.11 as a blue layer around the green supersonic beam. The governing mechanics of jet deflection into the cocoon at the so-called working surface is quite complicated and is discussed below. Nevertheless, the existence of cocoons in low-density jets is easy to understand on simple physical grounds.

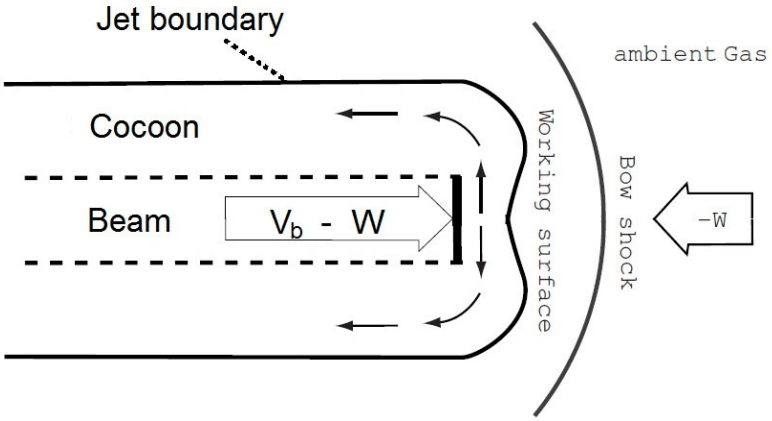

Figure 2.12: Flow schematic of the jet head in the rest frame of the working surface. Here W is the speed of advance of the working surface and V_b is the beam velocity.

As shown in Figure 2. 12, the jet head progresses at a speed can be determined by a balance of ram pressure (or equivalently momentum flux) along the beam axis in the rest frame of the working surface, as follow:

$$\rho_b (V_b - W)^2 = \rho_a W^2 \rightarrow \frac{W}{V_b} = \frac{1}{1+(\rho_a/\rho_b)^{-1/2}} = \frac{\sqrt{\eta}}{1+\sqrt{\eta}} \qquad (2.2)$$

Here W is the speed of the working surface, then ram-pressure balance is given $\rho_j (V_b\text{-}W)^2 = \rho_a W^2$. According to the obtained equation and using the definition $\eta=\rho_j/\rho_a$, we find that:

$$W = \frac{V_b \sqrt{\eta}}{1+\sqrt{\eta}} \qquad (2.3)$$

Equation 2.3 implies that the jet head of a diffuse jet ($\eta \approx 1$) is less than the beam speed V_b, which means that the beam gas constantly overtakes the jet head. In other words, incoming beam gas rather than accumulate there, after being shock-

decelerated and deflected sideways, continuously escapes into the cocoon at the working surface. The cocoon gas actually flows backward toward the inlet which is a simple consequence of mass conservation.
The relative velocity between the backward flowing cocoon gas and the ambient gas at the cocoon boundary is substantial. For the jet shown in Figure 2.11 it is subsonic. Because of the interaction of two flows, the cocoon boundary is subject to the Kelvin-Helmholtz shear instability which overturns and mixes the cocoon and ambient gases shown in the second and the third snap of the jet in Figure 2.11. As a result of the instability, only a lobe of cocoon gas is left intact at the jet head in the forth snap of Figure2.11. The central supersonic beam nevertheless appears to propagate without significant mixing at its boundary [51].

2.3.2. The Working Surface

As it's obvious in the figure 2.13, working surface has a complex detailed structure included a network of nonlinear waves and flow patterns that propagates as a coherent whole at the head of the jet [51].
Quite generally, the terminal shock system is similar to the triple-shock structure that is formed by Mach reflection in steady-state jets (see inset (a) in Figure 2.13), except that the structures downstream of the Mach disk (the reflected shock and rarefaction zones) are swept back by the oncoming ambient gas.

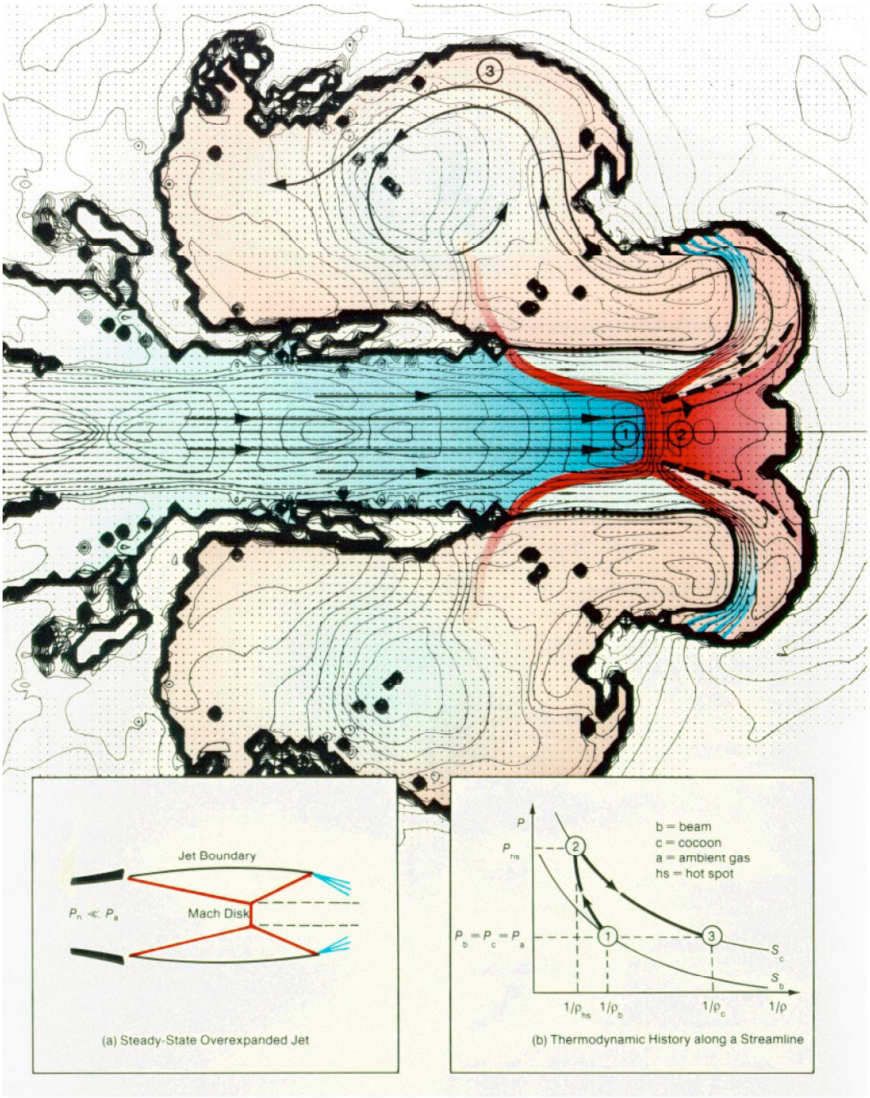

Figure 2.13:The working surface of a supersonic jet; the incident shock, the Mach disk, and the reflected shock are dark red, and the rarefaction fan is dark blue. This terminal shock structure is similar to the Mach reflection in a steady-state overexpanded(K< 1) jet shown in inset (a)[51].

Upon passing through the Mach disk, beam gas is virtually brought to rest with respect to the leading contact discontinuity, which is itself advancing into the ambient gas. The Mach disk converts the directed kinetic energy of the beam into

internal energy, thereby creating a region of very high pressure and temperature between the Mach disk and the contact discontinuity. Because of the confined longitudinally by the ram pressure of the opposing beam and ambient streams, this high pressure gas can escape sideways. Once beyond the radius of the beam, however, a fluid element will be blown back into the cocoon by the ram pressure of the ambient gas, which is there not balanced by the ram pressure of the beam. As the gas expands into the cocoon, its pressure decreases until it reaches the ambient pressure. Inset (b) in figure 2.13 traces the irreversible thermodynamic evolution of a fluid element following the streamline in figure 2.6 that passes through the Mach disk and into the cocoon. A key consequence of the irreversible nature of the terminal shock front is that the cocoon gas is generally less dense than the beam gas after pressure balance has been re-established. Vorticity is generated at the shock triple point in the form of a slip discontinuity (the dashed line in Figure 2.13), is carried into the cocoon, and contributes to the formation of a large-scale toroidal vortex surrounding the beam. The streamline in Figure 2.13 that flows above the shock triple point circles the vortex to produce a forward flowing stream of high-pressure cocoon gas [51].
This high-pressure environment in the cocoon drives the oblique incident-shock component of the beam's terminal triple shock. This intimate relation between the flow structures at the working surface and the adjacent cocoon constitutes a nonlinear self-consistent solution to the problem of flow deceleration and deflection in supersonic jets.

2.3.3. General Morphology

Figure 2.14 shows several simulated jets according to their values of M and η. Two general trends are apparent; scanning the third column from high to low density ratios, a marked thickening of the jet is seen. For the jets with low density ratios ($\eta < 1$), we have a thick cocoon of backward flowing gas around itself as it propagates, whereas for the jets with a high density ratios ($\eta > 1$) it is just a naked beam lacking a cocoon altogether.
Scanning the third row from low Mach number to high Mach number, the spatial extent of the cocoon increases is seen. At low Mach numbers the cocoon is but a lobe of material at the head of the jet, whereas at high Mach numbers the cocoon surrounds the central supersonic beam along its entire length. These behaviours of the jet can be understood with the help of a few simple concepts and equations. As mentioned earlier, the cocoon is supplied by gas that flows through the jet head at a rate proportional to $V_b - W$. Equation 2.2 shows obviously that this rate is small in high η jets, since $W \approx V_b$ for $\eta >> 1$ and large in low η jets, since $W << V_b$ for $\eta << 1$. Thus on kinematic grounds alone one would expect an inverse correlation between the density ratio and the size of the cocoon.
This inverse correlation is enhanced due to the shock heating of the jet gas at the terminal shock. The amount of shock heating at the terminal shock is related to

M_w^2, where the relative Mach number M is defined as $(V_b–W)/C_b$. Again if look at Eq.2.2 and also by the definition of M, it is found that $M_w = \frac{M}{1+\sqrt{\eta}}$. We can see that

for a given M, M_w, and thus the amount of shock heating, is largest when η is smallest. The greater the shock heating, the more gas flowing into the cocoon must expand to match the ambient pressure. So a small η leads to not only a large rate of flow into the cocoon but also a greater expansion of the shock-processed gas. The result, in agreement with simulations, is a cocoon with a relatively large volume and low density.

If η is held fixed, we will have larger Mach numbers implying greater shock heating, greater pressure differences between the working surface and the ambient gas, and thus cocoons with larger volumes. For the low Mach number jets, the extent of cocoons tends to be limited by shear instabilities on the cocoon boundary. The gas in the cocoon generally flows back toward the source which is resisted by corrugations in the cocoon boundary, such as the Kelvin-Helmholtz instability. At low Mach numbers, the combined effects of low pressure difference and induced instability cause to have the cocoon gas in a lobe near the jet head. Due to the above explanations, the trends in morphology on a qualitative level could be understood, but our attempts to quantify these effects analytically have not been successful Nonlinear and time-dependent effects are just too complicated. For example, the terminal shock structure is complex and time dependent indicating the cocoon is highly inhomogeneous. These inhomogeneitics lead to mass motions (vortices) within the cocoon that perturb the central beam and ultimately contribute to the unsteadiness of the terminal shock [51].

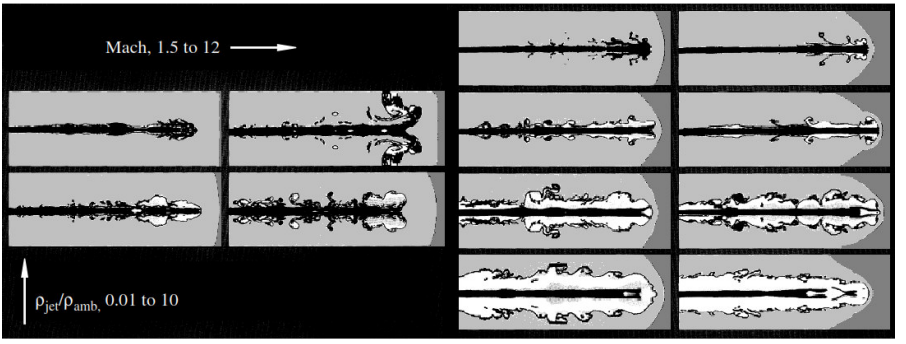

Figure 2.14: Dependence of the flow morphology of pressure- matched supersonic jets on the dimensionless parameters M and η [51].

At high Mach numbers the backflow within the cocoon could be also supersonic, and components of this momentum flux normal to the beam drive oblique shock waves into the beam. The perturbations are associated with toroidal vortices within the cocoon that drift back toward the source.

The final and general conclusion for matched hypersonic jet is as follows; For the jets with low density ratios ($\eta < 1$), it is expected to have a thick cocoon of backward flowing gas around the jet beam, and by increasing the density ratio, the thickness of cocoon decreases and finally for the jets with a high density ratio ($\eta > 1$) it is just a naked beam lacking a cocoon altogether. At high Mach numbers the cocoon surrounds the central supersonic beam along its entire length whereas at low Mach numbers the cocoon is but a lobe of material at the head of the jet. The combined effect of these trends is that only jets with low density ratios and high Mach numbers possess extensive cocoons.

Chapter 3

3. The experiment: setup

The equipment is designed and built specifically for the generation, control and display of hypersonic jets. The first version of this system was already employed to study the properties of highly under-expanded jets, making use of truncated nozzles and colour CCD cameras, detailed information can be found in the works by Belan et al. [57, 58]. In the present work the system was reconfigured, by adding and improving devices for the present purpose, i.e. long scale nearly matched jets. It also needed the new calibrations which are different for each given Mach number (see section 3.4).

Before describingthe experimental setup in details, a general view is explained as follows: the jets travel inside a modular vacuum vessel, with a maximum length of 5m and a diameter of 0.5m, much larger than the diameter of the jets. The required ambient inside the vessel is obtained by means of a valve system that sets the ambient density, at pressures ranging from 1.5 to 100 Pa, using a gas in general different from the jet gas.Density ratiocan range from 0.01 to more than 100. Actually in our results, the density ratio is in the range of 0.82 to 102. The visualizations and measurement system is based on an electron gun equipped with a deflection system, which creates an electron sheet. This sheet intercepts the jet under test, generating a plane fluorescent section of the flow, which is imaged on an intensified camera, and after the flow is analyzed by Image processing methods.

In particular, we want to achieve the possibility to compare a jet of gas in the environment, but the similarity between their lines needs considering the number as an argument of similarity of Mach, with regard to the jets isentropic, from known relations for isentropic flow one-dimensional, it is clear that it is determined by the ratio of stagnation pressure and the pressure of the generated gas in the casting itself.

$$\frac{P_0}{P_j} = \left(1 + \frac{\gamma - 1}{2} M^2\right)^{\frac{\gamma}{\gamma - 1}} \qquad (3.1)$$

where P_0 is the stagnation pressure and P_j is the pressure of the gas at the nozzle exit. Table 3.1 shows pressure ratio for ideal mono atomic gas:

Table 3.1: Ideal pressure ratio at matched conditions for mono atomic gas.

Mach Number	P_0/P_i (isentropic flow)
10	6907
15	50354
20	209151

From table 3.1, it is evident in order to generate a jet with a high Mach number in an ambient atmospheric pressure would be required very high stagnation pressure. Therefore to obtain the pressure ratios indicated in the table 3.1must combine a decrease in ambient pressure and increase of stagnation and so the best solution is to use of a vacuum chamber together with a driving system (see section 3.2) to be able to compress the gas to the required level of the stagnation pressure. The ambient pressure level; the pressure of the surrounding due to the jet generation in the casting itself, is obtained by means of a vacuum vessel, which is purposely designed.

3.1. Vacuum vessel

The jets under study are created inside a modular vacuum vessel. The vacuum is obtained through two vacuum pumps, a lobe pump and a vane pump in cascade configuration; these two devices are capable to lower the internal pressure down to 0.5–1 pa. All parts of the vessel are designed according to the correct principles of vacuum technology [59]. The figure 3.1 and 3.2 show the schematic and real vacuum vessel respectively. At one end of the vessel, a fitting is designed to set a nozzle to generate the jet flow due to imposing a given pressure ratio between the compressed gas to the ambient pressure; it is explained in the section 3.2.

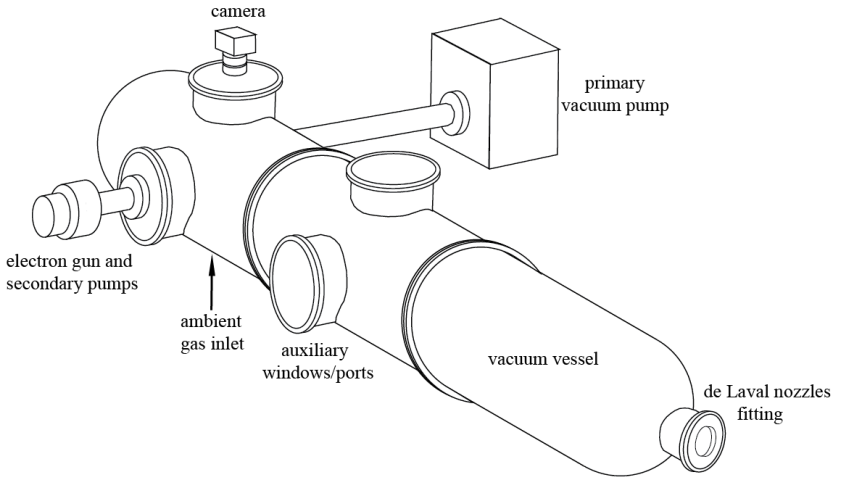

Figure 3.1:The schematic vacuum vessel.

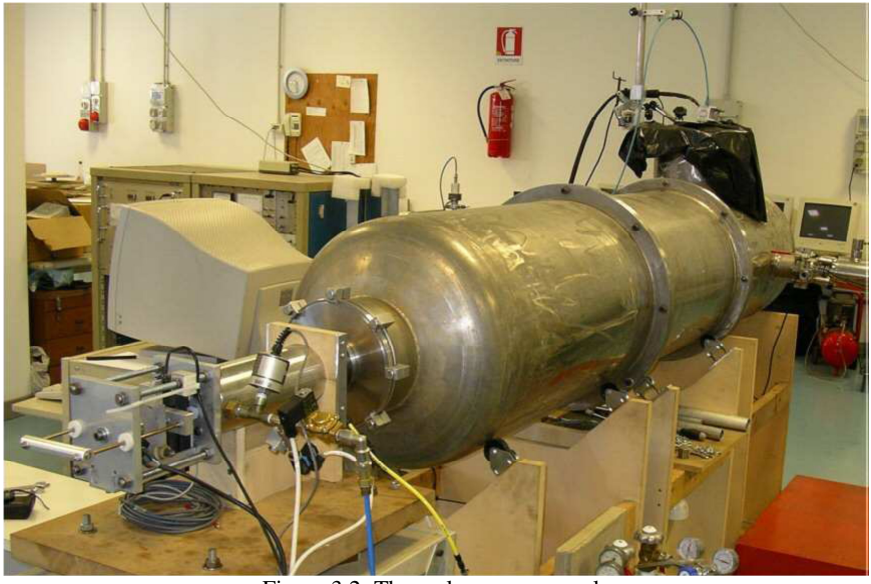

Figure 3.2: The real vacuum vessel.

The jets are created within a vacuum chamber modular steel 0.5m diameter and the changeable length from 1m to 5m. The vessel diameter is much larger than the jet diameter (see the output diameter of the nozzles in table 3.2), so the lateral walls effects are negligible and the jets can be considered as the free jets until they hit the vessel's end. The full version of the vessel (figure 3.3) is composed of three cylindrical sections (2, 3, and 4) plus a head and a tail section (1 and 5). The modularity of the apparatus involves the considerable advantage of fitting the total volume and length depending on the needs of the individual tests: as mentioned in chapter 2, in this experiment we plan to fix the length number (jet length to its diameter) in the range of hundred, and also regarding the jet diametersthat aredifferent for each given Mach numbers (table 3.2), the desirable jet length is different for each range of the Mach number. Hence a longer size of the vessel is needed to monitor the development of high Mach jets, and for the low Mach jet, a shorter length is needed.The head segment has a port for the connection of an electron gun, an optical window for a camera and service ports for vacuum pump, ambient gas inlet and electrical connections; these devices are for visualization and also control system which is explained in section 3.3 and 3.4. One of the intermediate sections of vacuum vessel is also provided with similar ports.

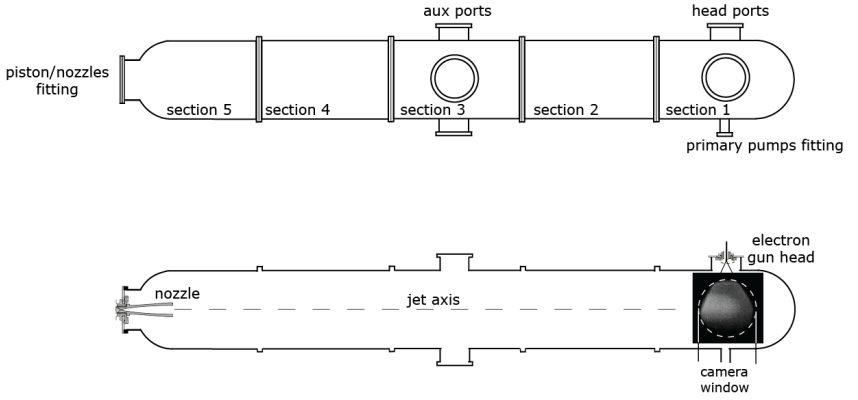

Figure 3.3: The full version of the vessel.

In reality that has occurred, three sections are extreme enough for Mach 10 and 15, and four sections for Mach 20 (figure 3.4). The required ambient inside the vessel is obtained by means of a valve system which sets the desired ambient density (at pressures in the range 1.5 to 100 Pa) using a gas in general different from the jet gas (explained in section 3.3.3). Pressures inside the vessel are monitored by means of two 0.25% accuracy transducers, ranging from 0.01 to 10 Pa and from 0.1 Pa to 100 Pa.

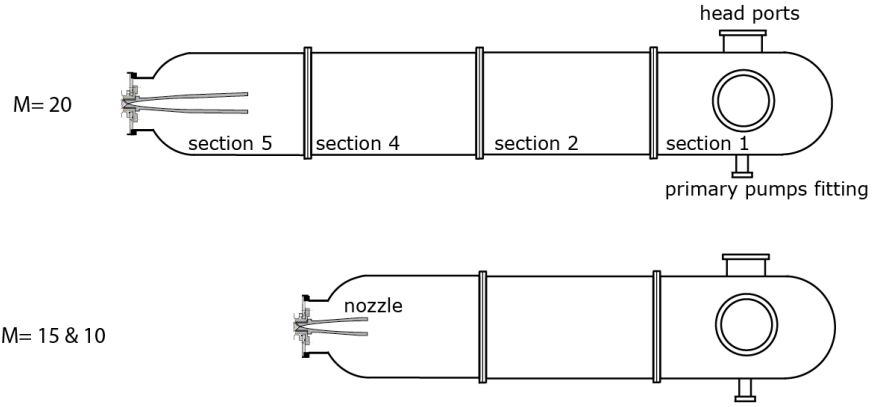

Figure 3.4:The schematic version of the vacuum vessel for different Mach numbers.

3.2. Nozzles and gas injection

The set of nozzles used in this experiment was designed to take into account the real gas properties. The pressure ratios taken in table 3.1 are the ideal pressure ratios, so the ideal pressure ratios were corrected by numerical calculations of boundary layer and heat exchange. The resulting pressure ratios are slightly different from the corresponding ideal ratios, and are reported in the table 3.2. The nozzles are de Laval nozzles and all have the same converging section and throat (diameter=2mm), whilst the diverging section depends on the Mach number, the relevant output diameters are also reported in table 3.2.

Table 3.2: Real pressure ratio at matched conditions.

Mach Number	P_0/P_j	Output diameter [mm]
10	6667	24.0
15	47620	71.4
20	178600	121.9

The appropriate de Laval nozzles are resin machined to high precision (tolerance on the radius of less than $2\,\mu m$). Each de Laval nozzle, shown in figure 3.5, operates at a single nominal Mach number (slight adjustments are possible), which is obtained by imposing a given pressure ratio between the compressed gas to the ambient pressure.

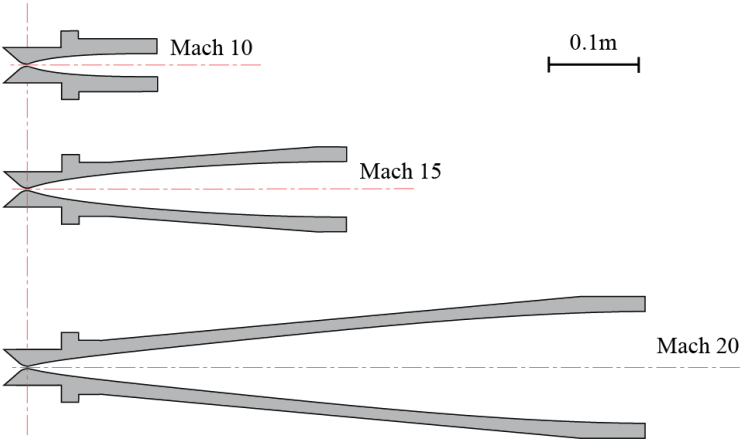

Figure 3.5: Three different de Laval nozzles operating at nominal Mach number 10, 15 and 20.

At higher Mach numbers, the apparatus which feeds the nozzles must be able to increase significantly the enthalpy of the gas, while reaching the desired stagnation pressure and temperature. For this purpose, we use a purely mechanical system, which is called Fast piston system.

3.2.1. Fast Piston System

The fast piston system is a purely mechanical system which compresses the jet gas to stagnation pressure in the 0.1 to 0.7 MPa range. It has an annular shape and it slides between two coaxial cylinders, as shown in figure 3.6. The piston is provided with a forward cylindrical extension having a set of ports. The inner cylinder is connected to the nozzle inlet by a second set of ports. The two port sets form a valve system which is closed during the piston run, and open when the compressed gas reaches the desired stagnation conditions.

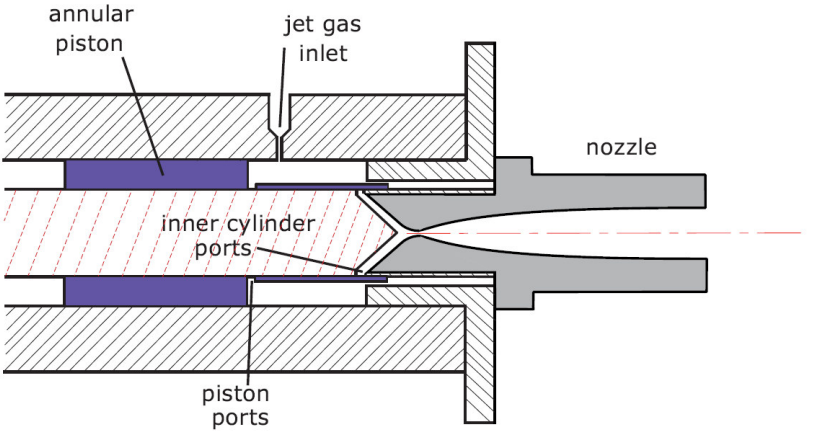

Figure 3.6:schemoffast piston system.

When the piston reaches this position, the two sets of ports match each other and the compressed gas flows into the nozzle. These processes are illustrated in figure 3.7. The thrust required to compress the inert gas is ensured by the compressed air in the back of the piston which is maintained continuously under pressure during the rest. It is normally held by an electromagnet and the starting time can be programmed on an electronic timer (see section 3.3.3.1). Electronic timer also controls opening time for the valves connected to vacuum vessel (for the ambient gas) and fast piston system (for the jet gas).

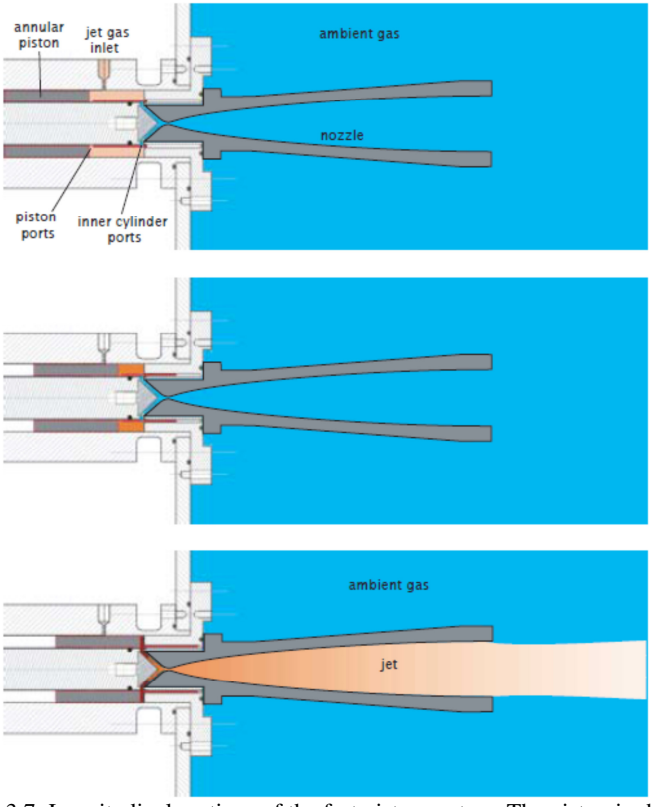

Figure 3.7: Longitudinal sections of the fast piston system. The piston is shown at 3 positions in sequence. Top panel: initial position, after the jet gas loading. Second panelan intermediate time instant of the gas compression. Bottom panel: final position, when the sets of ports match each other and the compressed gas flows into the nozzle.

The proper use of the piston requires well defined procedures for timing and loading of the jet gas, they are described in the section 3.3.3. Load pressures are measured by means of 1% accuracy transducers. A separate transducer is available to check stagnation pressures: when it is needed, can be assembled in place of the nozzle. The resulting repeatability of the jets at each piston run is very good. Of course, the valves require a finite time to pass from the closed to the open condition; therefore the jet mass flow Q has an increasing and a decreasing phase. At the end of compression run, owing to the valve opening, the outflow increases to a maximum value, which is in the order of the mass flow of the same nozzle under steady conditions, then it diminishes as the residual gas contained in the piston is used up. Figure 3.8 shows a typical gas injection curve and the method to obtain mass flow curveis explained in the calibration part (section 3.4).

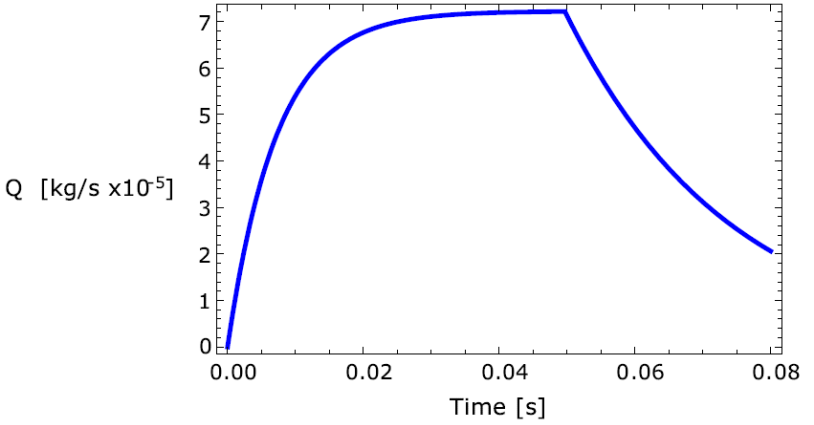

Figure 3.8: Jet gas injection: an example of mass flow vs time for an Helium jet at Mach 10.

3.3. Electron gun and Image Acquisition

The fact of operating at very low pressures hasled the adoption of electron beam technique to display the jet. The electron sheet intercepts the jet under test, so that the absorption of the light from a population of gas molecules raises their energy level to a brief excited state. As they decay from this excited state, they emit fluorescent light, as shown in figure 3.9. This fluorescent light generates a plane fluorescent section of the flow.

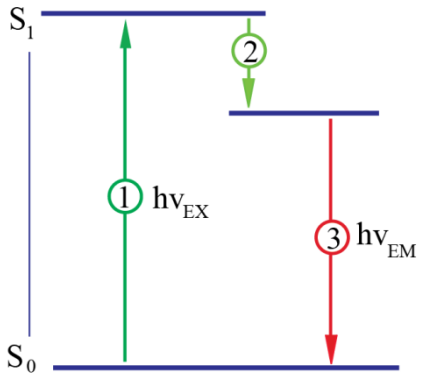

Figure 3.9:Jablonski diagram illustrating the processes involved in creating an excited electronic singlet state by optical absorption and subsequent emission of fluorescence.①Excitation; ② Vibrational relaxation; ③Emission.

This system required a long process of planning and development, have done mostly on investigation dealing with truncated nozzle [57,58]. The performing workin this thesis has been limited to simple maintenance, such as the realignment of the deflection coils, the waste removal and replacement of the tungsten filament and here it shows only a general description of the principles of electron gun operation, while the construction details. First, it must be said that lowering the gas density in the performance room of the system improves considerably, both in terms of efficiency (most free path for electrons of the beam) and also the duration of reliable life of its members (most of life filament). For these reasons two turbo-molecular pumps have been installed in the area of the gun to lower the pressure at least two orders of magnitude in the area of the gun (10^{-5} mbar). Here is a T-fitting allows the entry of high voltage cable, and placing a vacuum gauge ionization (figure 3.10).

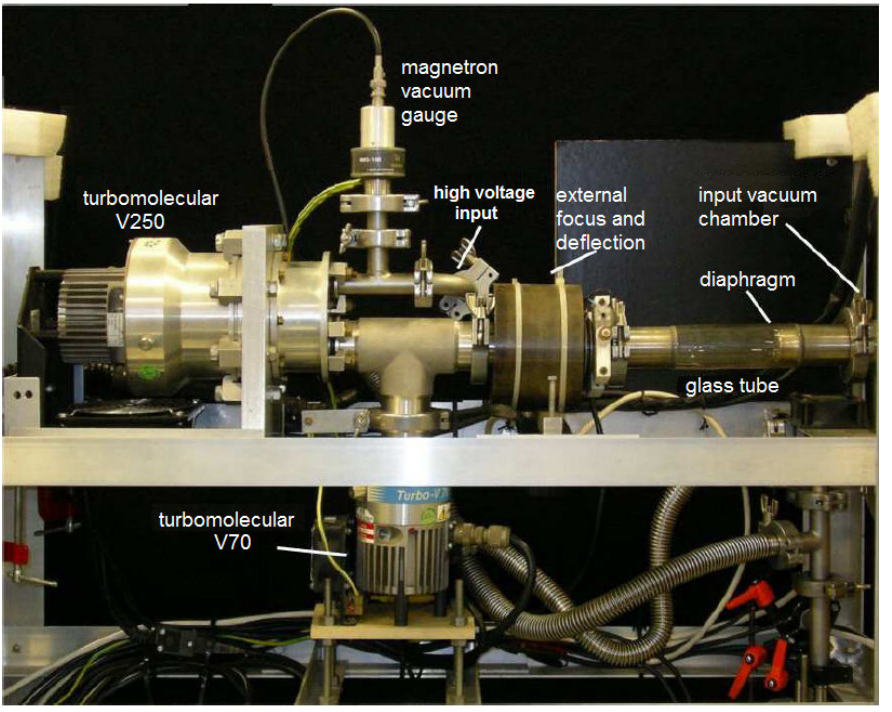

Figure 3.10. the system of the electron gun.

The electron beam, produced by the filament, propagates in a cylinder, on which there are the focusing and deflection coils, built in part of metal and glass one. This character is necessary to direct the beam at the entrance of the room: due to the strong heating which is caused by the impact of the electrons, it has been

realized that in a particular type of ferrous alloy nickel-cobalt, Kovar, having the same expansion coefficient of borosilicate glass, allows minimizing the thermal stresses. The whole is connected to the vacuum chamber through a hole with a diameter of 2.7 mm, sufficient for the passage of the beam, but small enough to avoid a sudden increase of pressure in the area of the gun (see figure 3.11). After passing the beam into the hole, it passes again one focusing coil with variable frequency, leading to collimate the beam, and finally two pair of deflection coils moves the beam in the desired position, which results an oscillating sheet in to view the portion of the jet of major interest (figure 3.11). So at the end we have an adjustable electron sheet which intercepts the jet under test.

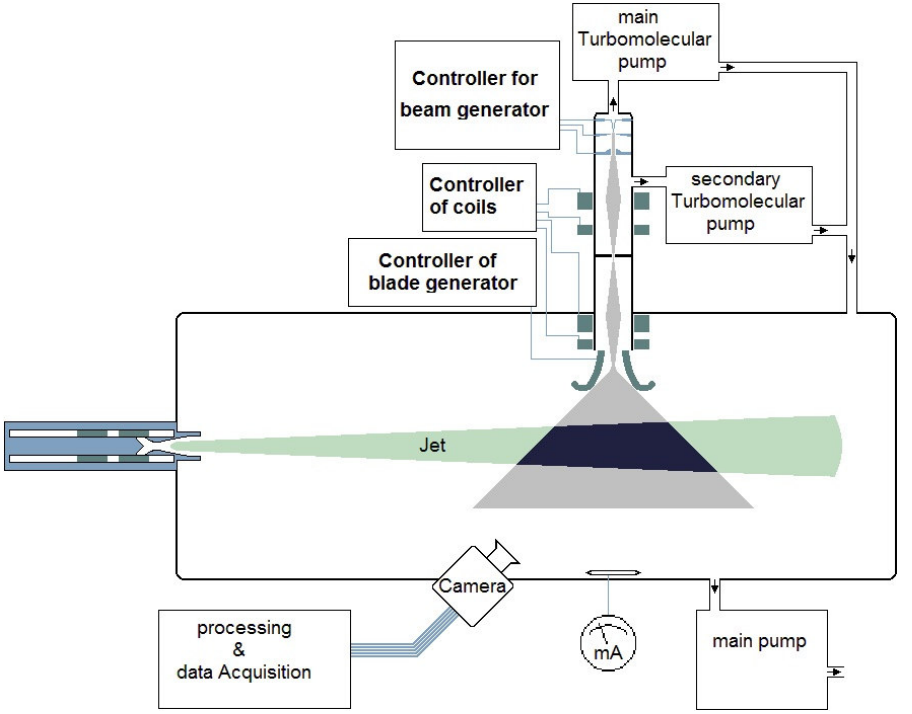

Figure 3.11: Diagram of the apparatus used for the creation of electron sheet.

Figure 3.12 shows the working principle of visualization which is created dueto crossing of the electron sheetby the jet under test. The Intercept of the electron sheet to the jet generates a plane of fluorescent section in the flow and the images of this fluorescent zone can be acquired with different kinds of cameras equipped bythe intensifier.

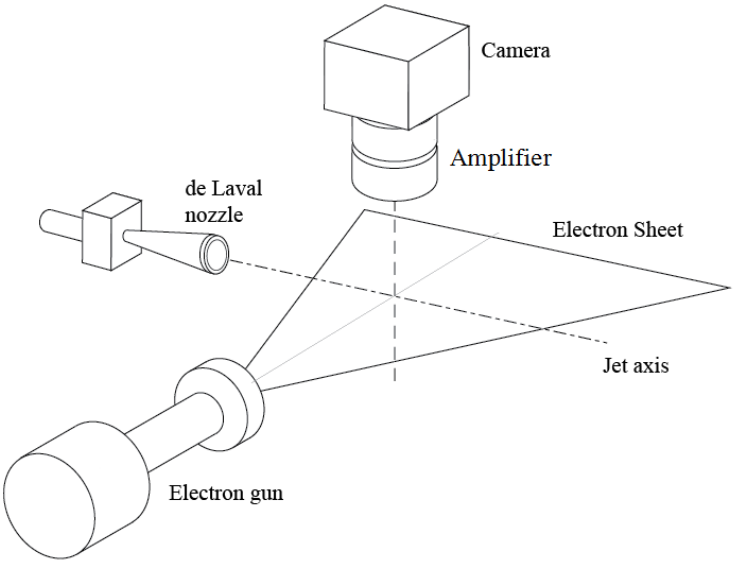

Figure 3.12: Working principle of visualization.

The use of this technique has, in turn, influenced the choice of gas for the jet and ambient, and limits it to only inert gases, because of chemical reactions that can be triggered by the electron beam. We also have necessitated the use of a camera with high sensitivity. These limitations are partially rewarded by the return to a single longitudinal section of the jet, which makes it easier. In fact, the analysis and processing of images are acquired over the three-dimensional case. In this experiment a fast CMOS camera (Phantom V5.2 and Phantom V710) has been used which captures 512x512 or 768x768 monochromatic images at frame rates of 2000 to 8000fps, with an exposure time of 195 to 898µs. Under the extreme conditions of the present experiment, it is necessary to balance two opposite needs, namely a short exposure to obtain sharp images and a long exposure to obtain a sufficient light level.

The camera is equipped with image intensifier which amplifies light from fluorescent images in low-light areas, to generate visible images in darkness. Through this process, an image can be intensified by a desirable factor depending on the quality of the recorded images which is a function of exposure time and sampling frequency among electron beam intensity. Achievable light gain of the intensifier, Hamamatsu V8070U, is more than 1000 (more details are reported in [59]).

To display the jet flow, images are captured and then its behaviour is analysed by image processing methods (explained in chapter 4).

3.4. The control system

The whole system for the jet generation, visualization and imaging need to be controlled and also synchronized among their operations. The control system could be devoted to three parts; jet generation part, visualization part and imaging part.

3.4.1. Jet Generation Part

For the jet generation, control instrumentation is collected in two separated units; one is a mobile rack located near the electron gun system and refers to pressure measurement and timing system. Another unit, placed under the piston system, which deals with controlling position system.

3.4.1.1. Timing system and pressure measurement

Figure 3.13 shows the pressure measurement and timing system, this rack also includes a control system for intensifier (middle section in figure 3.13) which is described in 3.3.1. Here two other sections related to the jet generation are explained (the numbering refers to Figure 3.13):

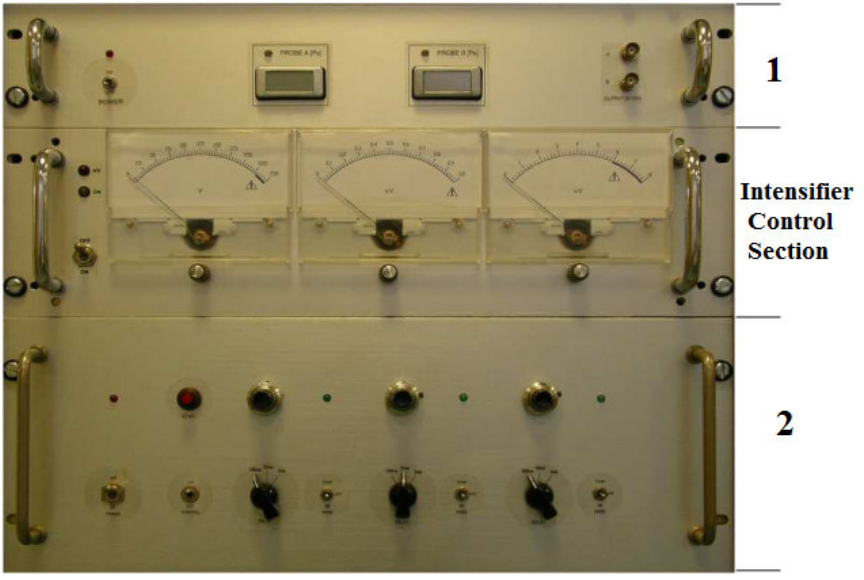

Figure 3.13:Top part: Pressure transducers, middle part: control intensifierBellow part: timing controler.

No. 1: Pressure transducers

The pressure inside the vacuum vessel is measured by two pressure transducers MKS, the characteristics of high resolution and repeatability. These two transducers, owing to the different full scale (0 -10 Pa and 0 - 100 Pa respectively), allow a good compromise between the range of measurable pressures and high resolution in the measuring range of interest (normally below 20 Pa).

No. 2: Timer (timing control system)

The apparatus consists of three identical and independent timers which are side by side as sequential stages to control the solenoid valves. In the present experimental setup, the three timers are connected in series with each other: the first (left) controls the opening of the solenoid valve for ambient gas, the second (middle) controls the valve to load the jet gas in the compression chamber of the piston, the third (right) releases and run the piston due to stopping the current to the magnet; in fact, the piston is held by the magnet which resists against the high air-pressure in the back of the piston, when the magnet-current is stopped, the piston runs (see section 3.2.1 and 3.4.1.2). The sequence is initiated manually by the operator due to pressing the buttons that are placed on the left of the potentiometers or remote button located near fast piston system. For a more detailed explanation regarding the pattern timing, see [59].

3.4.1.2. Piston Control

In addition to the rack illustrated in figure 3.13, which is necessary to control the sequence of the operation, another specific unit also is needed to control and manage the piston. This unit is shown in Figure 3.14.

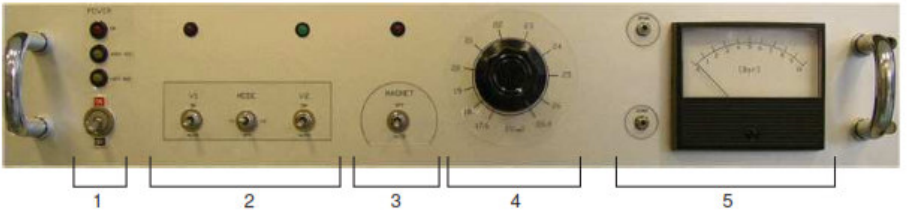

Figure 3.14: Control unit of the piston.

The control unit, with reference to the numbering of figure 3.14, consists of:

No. 1: Switch and power lights

This unit respectively allows powering rack and monitoring status of the equipment as well as the presence of auxiliary power supplies.

No. 2: Control valves of compressed air

To retract the piston at the end of each test, it is necessary to discharge the pressure-thrust of the piston; otherwise the operator would not be able to win the approximately 130 kg of necessary force to fulfill operation. Therefore this selector allows manually closing the valve that connects the piston to the compressed air line. This also allows opening a small service valve at the same time that discharges the air trapped between the valve and the piston into the atmosphere.

No. 3: Control magnet

Via this selector, the magnet, besides being controllable externally (by the timer), may alternatively be operated in full manual mode. It has been provided to encourage and enable easier shutdown during the dead time, so the magnet can get cool without shutting down the entire system.

No. 4: Power electromagnet

This potentiometer allows varying the voltage applied to the electromagnet; in fact, it is not possible to always try to maintain the pressure thrust as high as possible in order to obtain a more rapid compression of the gas (in order to limit any loss), because it has been verified that, in particular conditions of power, it is able to launch the piston without notice. Then it is possible to intervene supercharging slightly the magnet.

No. 5: Supply pressure

This part allows having a quick read of the supply pressure of the compressed air line, propelling the piston.
For more technical details of the instruments and operating procedures, please refer to the manual of the entire system ([59]).

3.4.2. Visualization Part

The instrumentation system to control the visualization part is collected in a rack which is made up of the following parts (the numbering refers to Figure 3.15):

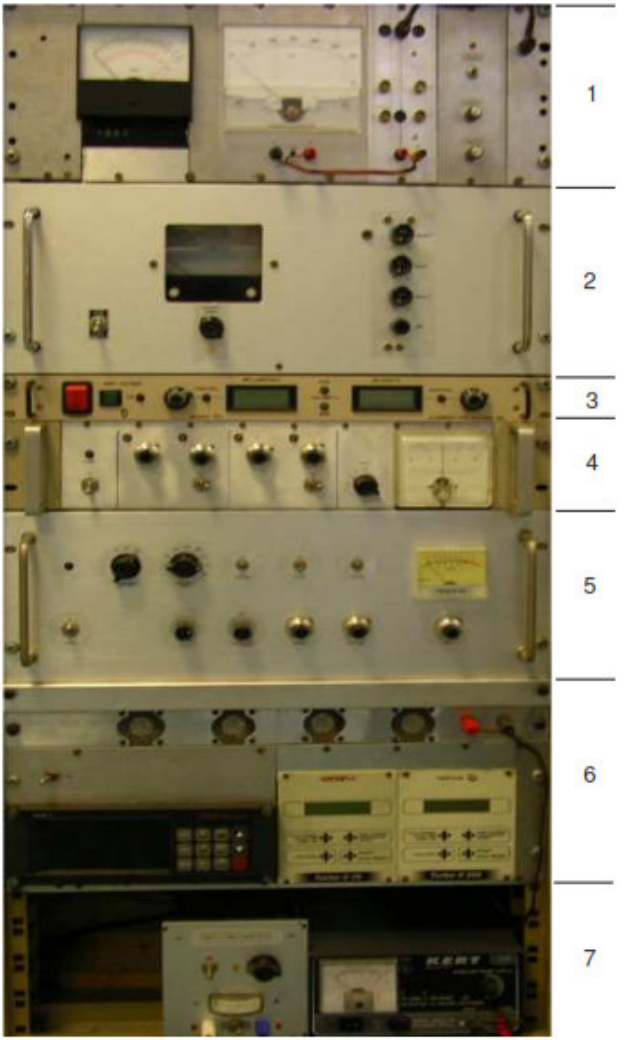

Figure 3.15: Control instruments of the electron gun and the vacuum.

No. 1: Ammeter display of the target and the vacuum gauge

A metal plate is located inside the vacuum chamber which the electron beam, after passing through the developing area of the jet, impacts. This is connected to an ammeter (centre) which allows knowing the current emitted from the electron gun; this information is essential to perform a good calibration of the system, because a higher current allows obtaining a brighter picture, to parity of the other

parameters. On the left we can recognize the display of the Pirani vacuum gauge providinga measurement of the vacuum generated in the area of the pumps; the operation of this probe is similar to that of a hot wire, with the difference that the heat exchange is, in the vacuum, takes place mainly by radiation.

No. 2: Control the the beam generator

The display shows the value of the current going through the filament, while below the potentiometer allows adjustment of the voltage across from 0 to 5 V. In the right is the potentiometer for controlling the voltage of the Wenhelt, varied from -150 V to 150 V.

No. 3: High voltage generator

This part allows applying an electric potential difference variable (0 KV to -20 KV) between the anode and the cathode. Normally it is adjusted to a constant voltage of -16 KV, shown in the right display, and a current of about 1 - 2 mA.

No. 4: Control the focalizations and deflections of the beam

This is the subsystem that allows controlling the direction and the shape of the electron beam. The first potentiometer adjusts the coil current of external focus which allows focusing the beam in correspondence of the diaphragm that separates the area of the electron gun from the vacuum chamber. The second controls the first deflection coil, adjustable by hand, which allows entering the beam on the hole in the diaphragm. The third one rules the thickness of the electronic blade, thanks to a coil of focusing inside the chamber, while the last coil acts on the vertical adjustment of the electronic blade. On the right is an ammeter that can be connected alternately to each of the four controllers described above.

No. 5: variables of Deflection

The electronic blade is obtained by swinging the beam between two extremes, what is possible using a deflection coil by alternating current. First it is necessary to choose the waveform, that is a particular movement of the beam between the two extremes of the blade, and secondly to adjust the symmetry; generally using a triangular wave symmetry of 50%, corresponding to a constant velocity motion. It is possible to control the oscillation frequency, typically of the order of kilohertz, that is the opening angle of the blade. It should be chosen carefully, for instance an oscillation too slow compared to the time of a taken exposure, would result in uneven illumination of the jet. Finally superimposing a constant current to the alternating deflection gives a constant horizontal deflection.

No. 6: Vacuum control for the secondary chamber

The two tools at the right control the two turbo-molecular pumps, providing the state of operation in the form of rotation speed, current consumption and operating temperature. By connecting directly to the vacuum gauge, it is possible to get also the automatic start-up to below a certain pressure. The instrument on the

left,controls the ionization vacuum gauge acting to measure the pressure in the area of the electron gun.

3.4.3. Imaging Part

Imaging part consists of the camera, intensifier and lens, which imaging process is controlled and accomplished by using a PC and the Phantom software. The starting time to record is manipulated by the manual button, “capture”, in the software; when the button is clicked, images are recorded on internal memory which is connected via Gigabit line. They are recorded in a continuous recording loop. So just before issuing the jet, record is started and some second after piston run (about 4Sec), another button, “trigger”, is clicked to stop recording. In other words, recording is continuously updated in the internal RAM of the camera; when the “trigger” key is hit, the recording is stopped, and then captured images can be retrieved in the memory.
Digital imaging provides multiple triggering and recording modes that can be tailored specifically for the most interesting parts of the jet movies. Image files are easily converted to TIFF formats using the included software package to make ready for image processing. Depending on the quality and the jet velocity, desirable sampling frequency and exposure time are chosen. The imaging system is also included lenses to enlarge the effective camera window, and the usable optical window depends on the camera lens; it can be adjusted between 0.2 and 0.4m regarding the given Mach number (jet size).
As mentioned the camera is coupled with an image intensifier to capture visible images of the jet in the dark surrounding conditions inside the vessel. The model of the used intensifier is Hamamatsu V8070U, and it is controllable due to the middle part of a rack placed near the electron gun system, shown in the figure 3.13; the middle part of the rack, controlling the intensifier, consists of three independent power supplies and a photo sensor. The first power supply (left) controls the voltage of the cathode (working voltage: 150 -230 V), the second (centre) controls the voltage of the MCP (working voltage: 600-1000 V) and the third (in the right) controls the tension of the phosphors (working voltage: 6.5 KV); by changing the MCP voltage, the multiplication factor, providing bright, is directly controlled. The sensor was installed instead as a precaution to protect the intensifier because too intense exposure to light sources is able to irreparably damage intensifier. The three feeds described above are enabled only if the photo sensor detects the intensity ambient light complies with the intensifier.
Through this process in the experiments, images were intensified almost by a factor more than 1000.

3.5. Calibrations

In each run at a given Mach number, a pair of gases is selected for the jet and ambient. The available gases are helium, argon, xenon and air, only the first three ones are used for the jet since the nozzle is designed for monoatomic gases. The required ambient inside the vessel is obtained by means of a valve injection system which sets the desired ambient density (at pressure in the 1.5 to 20 Pa range) by using a gas in general different from the jet gas.

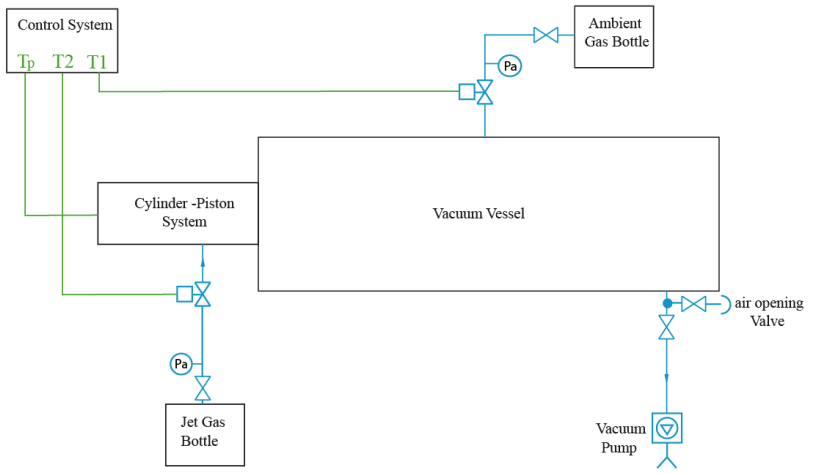

Figure 3.16: The general Sketch of the system.

Here timing control system lets control the opening times of solenoid valves. In the general (standard) procedure two solenoid valves must be controlled; one is connected from ambient gas bottle to the vacuum vessel (ambient gas valve) and another one from jet gas bottle to the fast piston system (jet gas valve), as shown in figure 3.16. They are operated in sequence due to the adjustment of the time intervals T1 and T2 in the electronic timer: T1 is the opening time of the first valve which lets ambient gas enters the vessel and T2is the opening time for loading jet gas in the piston system. Immediately after them the third timer stage T_p acts and piston moves (magnet releases), until the compressed jet gas is injected to the nozzle. The electron gun is turned on before starting the sequence, and the camera stays always on recording mode; it is stopped by a manual post-trigger, which retrieves the movie in camera RAM after theexperiment (see section 3.4.3). The relevant timing diagram is shown in figure 3.17.

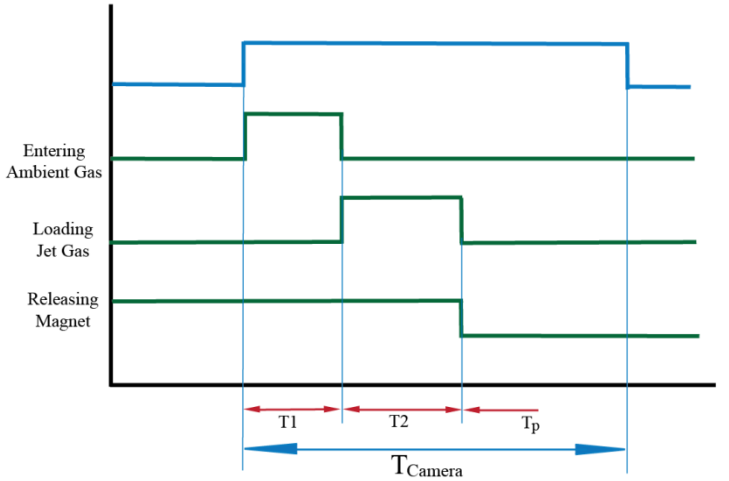

Figure 3.17: Time diagram of the valve system, fast piston system and camera.

In the sequence described above, the pressure inside the vessel increases in a characteristic way, shown as a sample in Figure 3.18, and this curve turns out to be particularly useful for calibration purposes.

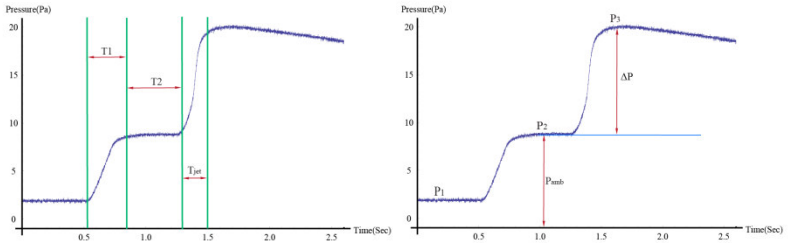

Figure 3.18: Pressure diagram inside the vacuum vessel during a run.

By operating the time-controlled system (analog timer) the pressure inside the vessel increases, as is shown in figure 3.18. Obviously, the curve doesn't start from zero, since the vessel is not ideal, and there is always residual air due to unavoidable small leakages. When the first stage of the timer acts, the first solenoid valve is opened for T1 second; during this time ambient gas enters the vessel, so the pressure goes up from P_1 (residual gas) to P_{amb}, then during the time for loading the jet gas inside the cylinder (T2), ambient gas reaches to the steady state. Just after T2 (Sec), magnet releases the piston and after a fast compression, lasting a measurable time, the jet gas escapes through the nozzle. The jet flow

leads to increase rapidly the pressure to the maximum value(=P3) and finally, at the end of the test, the pressure begins to slowly decrease owing to vacuum pumps (Figure 3.18).

About ambient pressure, there are two technical points:

1- The pressure of residual air is about 2 Pa and ambient gas should overcome the residual (air).

2- The best working condition for the electron gun is under 15 Pa, because for the higher pressure and consequently higher density, the noises are increased due to sparks which are created by the particles ofthe dense gas crossing electron sheet.

Hence for a typical test, 10 Pa is pre-assumed as the ambient pressure for each test.

In the first step, the relationship between opening time of the first solenoid valve (T1) and the ambient pressure (and subsequently ambient density) is obtained, so here just T1acts and T2 is deactivated. For each given ambient gas, the pressure of the ambient gas bottle is kept fixed and the pressure inside the vessel is measured with high precision pressure transducer which is located inside the vessel wall. Figure 3.19 shows a sample of pressure behaviour of Helium gas, which T1 is set on 200ms and gas bottle pressure of 1.2 bars.

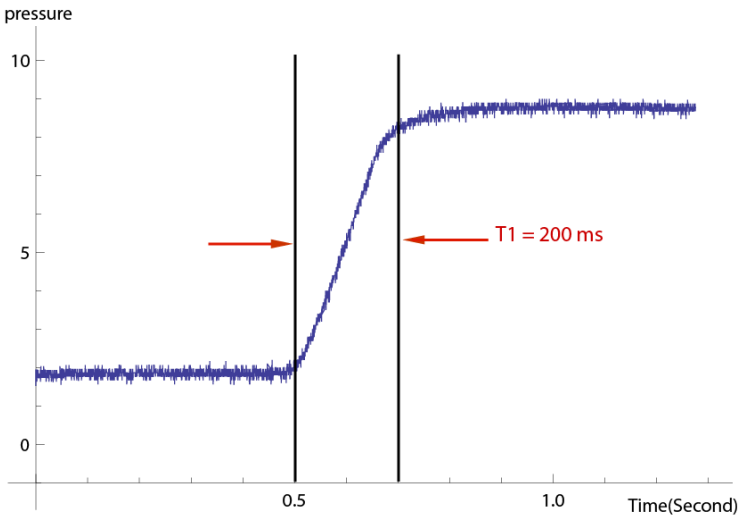

Figure 3.19: Helium gas, T1: 200ms and gas bottle pressure: 1.2bar.

As mentioned the curve is started from residual air pressure (about 2 Pa) and with opening the valve, rapidly grows up. The pressure increases slightly even after closing the valve, because the residual ambient gas in the pipe passes to the vessel, and then the gas reaches on the steady condition. In this case (figure 3.19) about 100ms after closing the valve, the curve reaches to the steady pressure which is

9Pa. Indeed this curve is the first part of the pressure curve in figure 3.18 where the pressure increases from P1 to P2. This process is repeated for other opening times (T1) and final ambient pressure is obtained. Figure 3.20 shows the ambient pressure inside the vessel via valve opening time (T1) for Helium gas with 1.2bar pressure of the gas bottle.

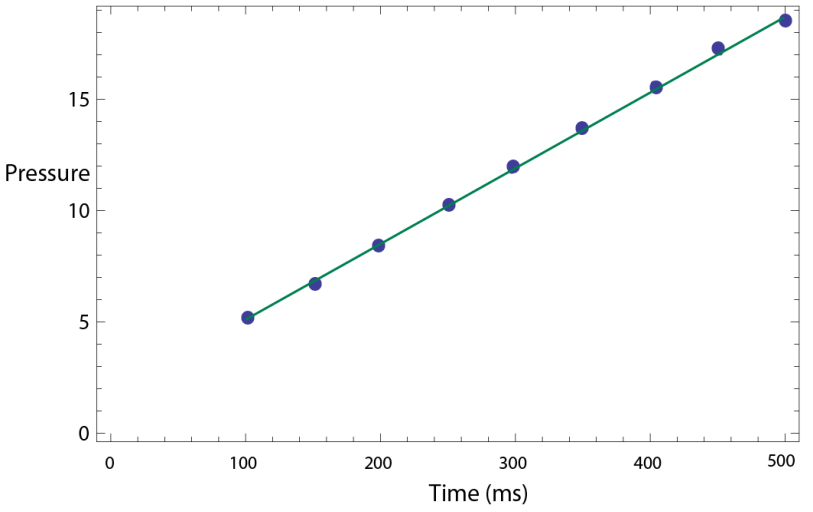

Figure 3.20: Ambient pressure via opening time of valve for Helium gas, 1.2bar bottle pressure

In this way for a fixed pressure of the gas bottle, desirable ambient pressure is acquired due to adjustment of the opening times of the valve which has an almost linear relationship (figure 3.20). This procedure is repeated for different pressure of the gas bottle, because whenambient and jet gases are the same, they are fed from the same bottle. It means the pressure of the ambient gas bottle cannot be fixed on unique pressure; it should be chosen according to the required stagnation pressure for the jet gas. Hence this procedure is repeated for several bottle pressures and yields other graphs via T1. Figure 3.21 illustrates the helium ambient pressure via opening time (T1) for different pressures of the gas bottle. The pressure diagram gives a complete calibration of the system for ambient pressure and consequently ambient density. About the ambient pressure, it is almost immediate to find calibration charts in the form:

$$P_a = F(P_{as}, T1) \qquad (3.2)$$

where P_{as} (ambient supply pressure) is the pressure fed by the ambient gas bottle.

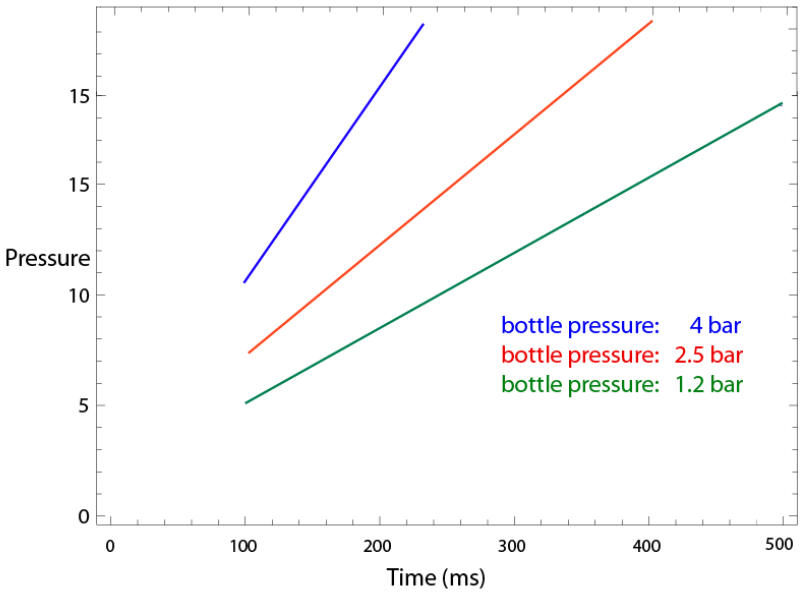

Figure 3.21: Ambient pressure via opening time of valve for Helium gas, different bottle pressures.

Due to the timing diagram, described in figure 3.17, after the injection of the ambient gas, the jet gas is loaded inside the cylinder; the duration of this stage is T2 and as much as the jet gas is loaded inside the cylinder, the stagnation pressure of the jet gas, at the end of compression,is increased. The last stage of timing diagram (figure 3.17) is releasing the magnet; just after T2, the magnet releases the piston, making a fast compression, and the jet gas escapes through the nozzle (see section3.2.1). The thrust required to compress the inert gas in ensured by the compressed air in the back of the piston which ismaintained continuously under pressure during the test. This pressure for Mach 15 and 20 is about 6.8 bar and for Mach 10 is about 5bar. But how long should be the duration of this step (T2), in other words how can obtain the suitable stagnation pressure for the jet gas by adjusting T2?

To answer this question come back to the figure 3.18 showing pressure variation inside the vessel. As it is clear, in the sequence of timing control system (figure 3.17) the pressure inside the vessel increases in a characteristic way. Figure 3.21 shows a sample of pressure variation; this curve turns out to be particularly useful for calibration purposes.

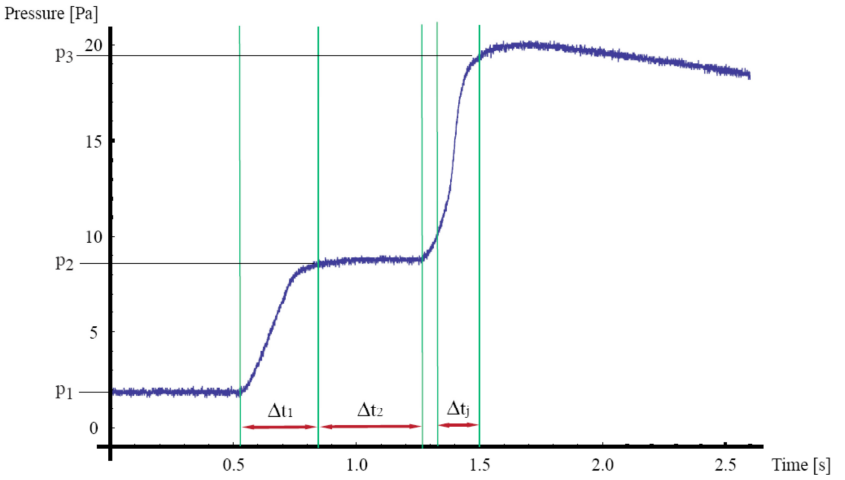

Figure 3.22: Pressure diagram inside the vacuum vessel during a sample run.

Let shortly explain the sample of pressure diagram, shown in figure 3.22: when the first timer stage is done (T1), the pressure grows up to P2, then during second stage, loading of the jet gas in the cylinder (T2), ambient gas reaches a steady state. Just after T2, the magnet releases the piston and after a fast compression, the jet gas flows through the nozzle. The jet travels through the vacuum vessel in the subsequent time interval ΔT_j, also called jet lifetime. It can be shown that the duration of the jets in this experiment is well longer than their physical time scale, defined as the sound crossing time on a jet radius (it is explained in section 5.1.1), so the jets may be considered nearly steady. However, on the time scale of the operation procedure their lifetime appears always much shorter than the gas loading times T1 and T2. ΔT_j can be estimated directly by the pressure curve as illustrated in figure 3.22, but the final value is safely measured from the movie, since the camera has a very good temporal resolution, working at frame rates in the order of thousands per second.

The pressure transducers, monitoring the pressure (figure 3.22), are located at the vessel wall. Previous measurements obtained by moving the transducers to different ports have shown that the unperturbed ambient pressure can be considered constant along the vessel, since the effects of the distributed leakages and of the pumping are spatially balanced. Here it is also assumed that the ambient pressure in front of the bow shock(figure 2.1) is constantduring the jet imaging, since the time scale involved in creating a time-varying ambient pressure is much longer than the very fast jet injection time.

By pressure diagram, a complete calibration of the system is stated. About the ambient pressure, for each given gas, desirable pressure is achievable by formula 3.2 obtained from calibration charts.

About the jet pressure, the calibration of time T2 and piston supply pressure Ps, in order to obtain a matched jet having the desired properties, is much more complicated as shown in what follows. In the throat of a de Laval nozzle, gas flow is choked, so the equation for the jet mass flow rate can be written in the ideal case by means of standard gas dynamic relations:

$$\dot{m} = A_c \rho_0 c_0 \left(\frac{2}{\gamma+1} \right)^{\frac{\gamma+1}{2(\gamma-1)}} \tag{3.3}$$

where A_c is cross-sectional area of the throat whilst P_0 and T_0 are stagnation pressure and temperature (shown in figure 3.23).

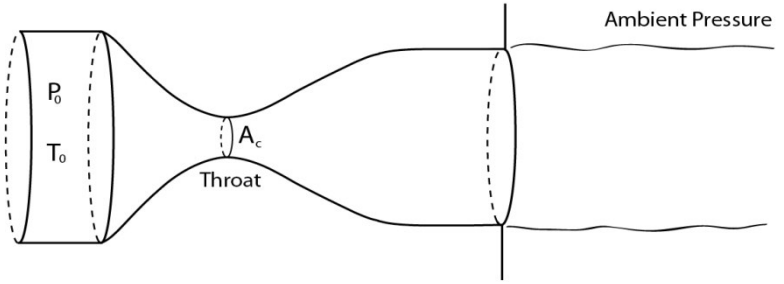

Figure3.23: Sketch of a nozzle with a choked flow in throat.

This formula can be rewritten in terms of stagnation pressure and temperature by means of the ideal gas law $P = \rho R_j T$:

$$\dot{m} = A_c P_0 \left(\frac{\gamma}{R_j T_0} \right)^{\frac{1}{2}} \left(\frac{2}{\gamma+1} \right)^{\frac{\gamma+1}{2(\gamma-1)}} \tag{3.4}$$

At the end of the experiment, the jet gas is completely mixed with the ambient gas and it can be assumed that the mixture has the room temperature T_a, because the mass of the ambient gas is much greater than the one of the jets and because of the fast effect of heat radiation from the vessel walls. Thus the pressure increase due to the jet $\Delta p = P3 - P2$ shown in figure 3.21 can be related to the density increase $\Delta\rho$ inside the vessel volume V and to the jet mass flow:

$$\frac{\Delta P}{R_j T_a} = \Delta\rho = \frac{m}{V} = \int_{\Delta t_j} \frac{\dot{m}}{V} dt \tag{3.5}$$

Now by replacing (3.4) in (3.5) and rearrange the formula it is found:

$$\Delta P = \frac{A_c T_a}{V} \int_{\Delta t_j} P_0 \left(\frac{R_j \gamma}{T_0} \right)^{\frac{1}{2}} \left(\frac{2}{\gamma+1} \right)^{\frac{\gamma+1}{2(\gamma-1)}} dt \qquad (3.6)$$

Here the crucial parameters P_0 and T_0 are not independent since they are due to the compression in the piston. For a fast ideal isentropic compression they can be related to the supply pressure Ps and temperature $T_s = T_a$, i.e. P and T of the gas loaded from the bottle into the piston,

$$T_0 = T_s \left(\frac{P_0}{P_s} \right)^{\frac{\gamma-1}{\gamma}} \qquad (3.7)$$

The combination of (3.5) and (3.6) leads to:

$$\Delta P = \frac{A_c T_a}{V} \int_{\Delta t_j} P_0 \left(\frac{P_s}{P_0} \right)^{\frac{\gamma-1}{2\gamma}} \left(\frac{R_j \gamma}{T_a} \right)^{\frac{1}{2}} \left(\frac{2}{\gamma+1} \right)^{\frac{\gamma+1}{2(\gamma-1)}} dt \qquad (3.8)$$

This formula shows how the final increase in vessel pressure Δp and the jet lifetime Δt_j are related to the pressure P_s of gas initially loaded into the piston and to the stagnation pressure P_0 at the end of the compression. Δp, Δt_j and P_s can be measured directly, so the formula can be used to express P_0, which in turn depends on the gas loading time T2, and finally leads to calibration charts of the kind

$$P_0 = G(P_s, T2) \qquad (3.9)$$

where Δt_j doesn't appear because it is not an independent parameter, actually the jet lifetime for a given nozzle properly working depends on the quantity of gas available, which is automatically set by selecting P_s, T2. Up to now, the derivation of the calibration charts was based on ideal conditions, as a further step accurate calibration chart must then be obtained including corrections for non-ideal effects like small heat losses, depending on the piston driving pressure, frictional effects and progressive opening of the piston valves, so that they take the form

$$P_0 = G(P_s, T2, P_p, k) \qquad (3.10)$$

whereP_p is the piston driving pressure and k is a set of coefficients related to the laboratory conditions.

Pp is different for each test; for Mach 20 and 15 is on maximum pressure which is 6.8 bars, but for Mach 10 is about 5 bars, because for this case required stagnation pressure is less than atmospheric pressure, so if the pressure in the back of the piston (P_p) is too high and in front of the piston is less than atmospheric pressure, magnet cannot hold the piston. Therefore for Mach 10, lower piston driving pressure is used. Finally, the values of P_0 and T_0 yield pressure, temperature and

density at nozzle exit, so that the calibration charts can be used to set the desired properties.
For example, the first step to get a hypersonic jet is to find a good pressure ratio for a given de Laval nozzle (table 3.2). Then, after having set piston driving pressure and supply pressures, changing T1 and T2 gives different pressures for ambient and jet respectively. Typically, for a given nozzle, a set of experiments is performed changing the parameters T1, T2 whilst P_{as}, P_s and P_p are kept constants, in general they are set afresh when a new nozzle is assembled on the system. Furthermore, in a set of experiments T2 can be adjusted to obtain well matched jets or even slightly unmatched jets, having a jet-to-ambient pressure ratio P_j/P_a in an approximated range 0.7 to 1.3, since the boundary layer inside the nozzles has stabilizing effects against the pressure mismatching and prevents the formation of the normal shocks inside the nozzle and at the exit [51,53,56] (for more information see section2.2.1); this gives rise to interesting flow morphologies, appearing as perturbations of a properly matched jet (for slightly unmatched jets it is also possible to calculate corrections to the nominal Mach number). Bringing the pressure ratio outside of this range leads instead to the formation of strong shocks and expansions close to the nozzle exit, i.e. to definitely over or under expanded jets. In general, these jets are greatly affected by turbulence, so that the mixing with the surrounding ambient becomes faster than in matched jets. When this phenomenon takes place, it can be observed in the camera window.
In our experiment the jet injection into the vessel is not ideal, or instantaneous, but follows a time-dependent pattern (see figure 3.8 related to the mass flow curve). We define the values of the parameters corresponding to a nozzle operating in ideal steady conditions as “nominal”. Here the nominal Mach number at the nozzle exit, depending on the given tests, are M= 10, 15 and 20, the Reynolds number, defined as $2r_0$ M C/ν, where C is the speed of sound and r is the jet radius at the nozzle exit, is of the order of 10^4 forMach 10 and of the order 10^5 forMach 15 and 20 which are expected sufficiently high to represent near asymptotic conditions.

3.6. Test Procedures

In this research, owing to the specific needed conditions and also the limitations of the first version of the system which wasalready employed to study the properties of highly under-expanded jets with truncated nozzles [57,58],the system is modified and calibrated for the new purpose,long scale nearly matched hypersonic jet flow.The test procedure and calibration for each part is different due to the required pressure ratio for each given Mach number.
The test procedures are divided into three parts; for each part a nozzle, i.e. a nominal Mach number is chosen, then density ratio is varied due to selecting different gases and/or adjusting the pressure ratio on near unity. In what follows, the first part is Mach 20, second Mach 15 and the third is Mach 10.

3.6.1. MACH 20

The de Laval nozzle for Mach 20 has a large diameter (table 3.2), so that it is necessary to put the vessel in a long configuration in order to observe jets extending for a sufficient number of initial diameters. According to table 3.2, matched pressure ratio P_0/P_j is close to 180000, so for a typical test at ambient pressure P_a up to 10 Pa, stagnation pressure should grow up to about 18 bar, what may create safety problems in our system. The solution is to decrease the ambient pressure to the minimum value (about 1.5 Pa), but as mentioned, vacuum vessel is not ideal and at low pressures residual air becomes predominant. To overcome this problem, the vessel is filled with ambient gas up to more than 20 P_a, then a timer let the vacuum pumps work for a given time, in such a way as when the vessel pressure reaches again the minimum level, the residual gas can be considered almost pure ambient gas. After,the general procedures described in section 3.4and also timing system (figure 3.17), can be followed until the experiment is completed. Timer stage T2 must be set in advance in order to obtain the desired jet.
This system is shown in figure 3.24 and is for the case that jet gas and ambient are not the same.

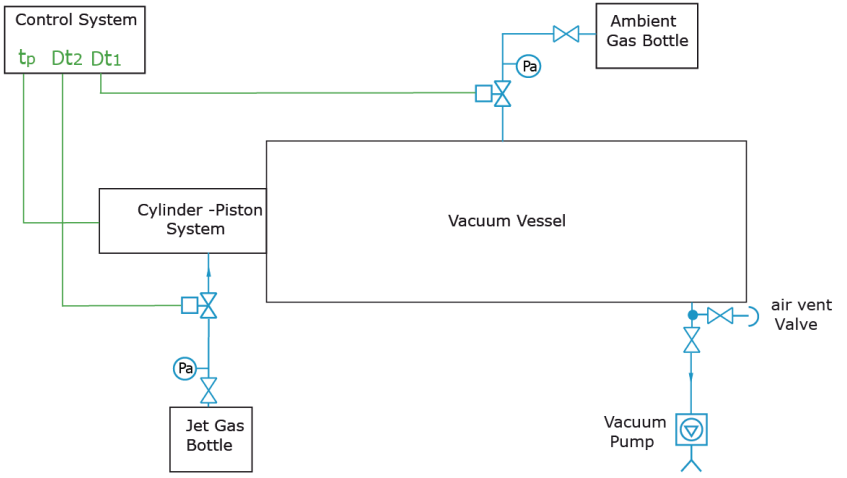

Figure 3.24. General diagram of the system controls and connections

3.6.2. MACH 15

According to table 3.2, the matched pressure ratio P_0/P_j for Mach 15 is about 48000, well afforded by the system in standard configuration. In this case the standard procedure described in section 3.4 can be followed as it stands. But when jet and ambient gases are fed from the same bottle, the system and procedure change. The system is modified by adding a manual solenoid valve to the connecting pipe at a given distance before ambient solenoid valve (red valve in figure 3.25). In this case, first the valve of jet gas bottle is regulated to the pressure to afford thedesirable pressurefor ambient. This pressure is obtained due to the data from calibration; figure 3.21 shows a sample of needed data.While the bottle valve has been opened, the manual solenoid valve is opened for a short time to trap the gas in connecting pipe to the vessel (red pipe in figure 3.25). By this system, we have enough amount of ambient gas in desirable pressure which is kept inside the connectingpipe; in other word the connecting pipe plays a role of reservoir for the ambient gas. Now to afford stagnation pressure of the jet gas, obtaining at the end of compression phase of the piston, supply pressure would be increased to the suitable one due to the calibration charts.

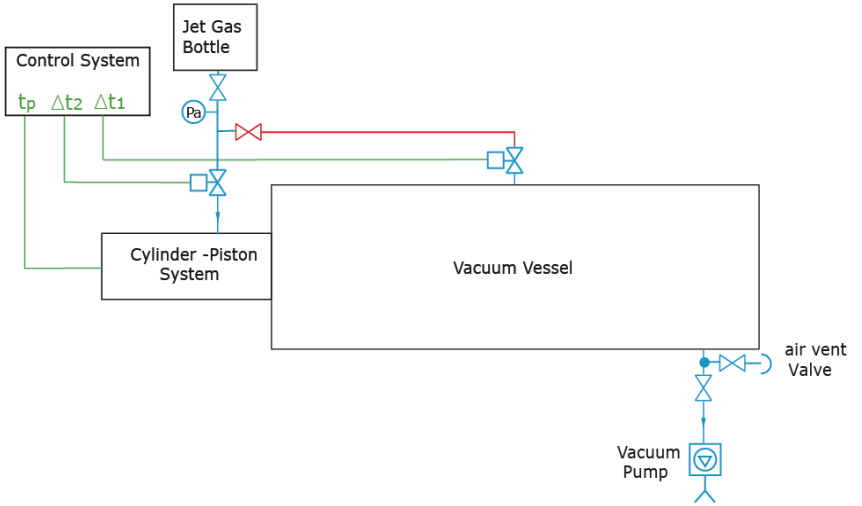

Figure 3.25. General diagram of the system controls and connections when ambient and jet gases are the same

3.6.3. MACH 10

For Mach 10 the calibration and test procedures are more complicated. The main issue is the matched pressure ratio P_0/P_j , which in this case is about 6700. One way to obtain this pressure ratio can be theincrease of ambient pressure, but there is a limitation, because with increasing the ambient pressure, the quality of images worsens. To satisfy the pressure ratio for a typical test at 10Pa of ambient pressure, stagnation pressure should be less than 0.7bar, i.e. less than atmospheric pressure. This condition creates problems in the loading phase of the piston, since it becomes necessary to load low pressure gas and then recompress it to the final P_0< 1bar avoiding contamination from the surrounding ambient. To get the proper stagnation pressures, another system has been designed. As shown in Figure 3.26, a small reservoir has been added to the jet gas pipe to keep inside it some amount of gas; its pressure is a bit more that atmospheric pressure. Once this reservoir is full, the valve of jet gas bottle is closed and by adjusting a precision valve connected to the vacuum pumps, the pressure of jet gas in the reservoir is reduced to the desirable one (in the order of 0.4 bar). This so low pressure of the gas inside the reservoir can deliver a suitable stagnation pressure at the end of compression phase of the piston. Again, the desired pressure ratio is obtained by preceding T1 and T2.

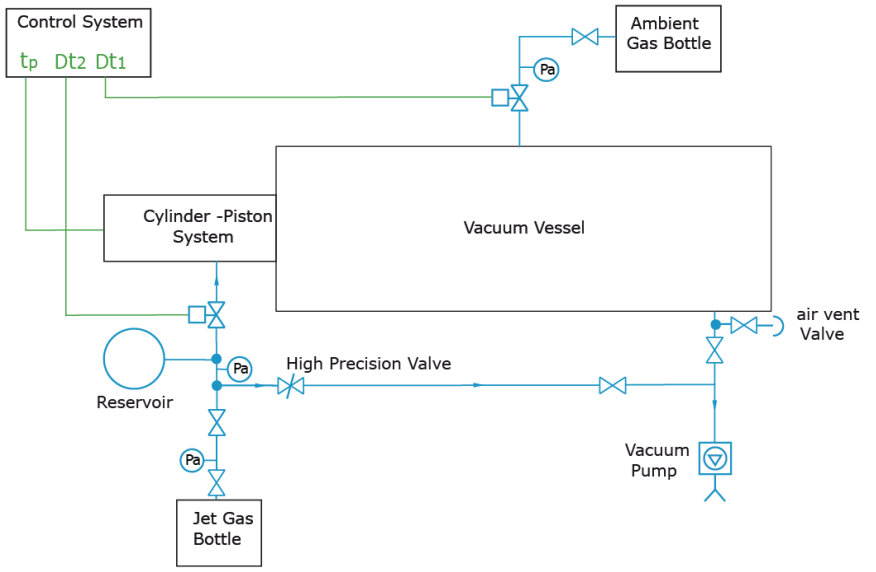

Figure 3.26. General diagram of the system controls and connections when ambient and jet gases are the same

Chapter 4

4. Visualization and measurement techniques

A wide range of visualization techniques has been developed over the years for understanding the physical phenomena of complicated 3D flows. Traditional visualizations are primarily qualitative, yielding limited information on flow structures; any quantification required laborious measurement by hand, typically from photographic film. An important achievement of modern experimental fluid mechanics is the invention and development of digital techniques for visualization and measurement of instantaneous flow velocity and flow formation. In the most part of modern techniques, like particle tracer methods, the flow is illuminated in some manner such that the flow particles in a finite domain are visible; a series of images of the flow are captured to record how the particles move in response to the fluid flow and then the quantitative analyses of the flow, including velocities and structural characterization, is performed by image processingwhich plays an ever-increasing role in fluid mechanics research. The best applied visualization method depends on the tests and sometimes common methods do not work for particular ones and other innovative methods are used. Hypersonic jet flow is one of these topics; over the last decades several experimental systems have been produced to create and visualize this kind of flows, and most of these experiments used innovative techniques for visualization. Some examples are the plasma jets created by laser ablation of shaped targets, or by lasers colliding on aluminum foils [60, 61, 62], the laboratory plasma jets which have been produced involving magneto-hydrodynamics effects [63], the laboratory study concerning the deflection of supersonic jets produced by molecular clouds [64]. In general, these methods could visualize the jet on the short scale lengths. The apparatus used in the present work is completely different from mentioned ones, and as described in the chapter 3, it is built specifically for the generation and visualization of hypersonic jets on the long scales; the main principle of this system is the production of fluorescent images of the flow under test by an electron beam (explained previously in section 3.1); then flow is displayed and analysed by image processing methods. This chapter in the coming section discusses briefly

about the visualization system, which is explained in more details in the last chapter, and mainly the next sections focus on the measurement techniques for moving structures velocities, image processing methods for denoising and reconstruction of jet images, an optical technique for measurements of the jet spreading angles, and finally density measurement technique.

4.1. Visualizations

The visualization technique is explained in details in the chapter 3, and here it is just briefly described. The visualizations are based on the electron beam method: the jet travels along the vessel and intersects an electron sheet. Indeed the electron gun emits an electron beam and the beam, after passing through the six coils performing focusing and deflection, creates electron sheet. When the jet intersects the electron sheet, fluorescence turns out; certain molecules of the gas absorb the light and raise their energy level to a brief excited state. As they decay from this excited state, they emit the fluorescent light (see section 3.1). Here fluorescence takes place and permits to acquire the images. A high speed camera equipped an image intensifier capture these images and then by image processing, the flow is analysed (figure4. 1).

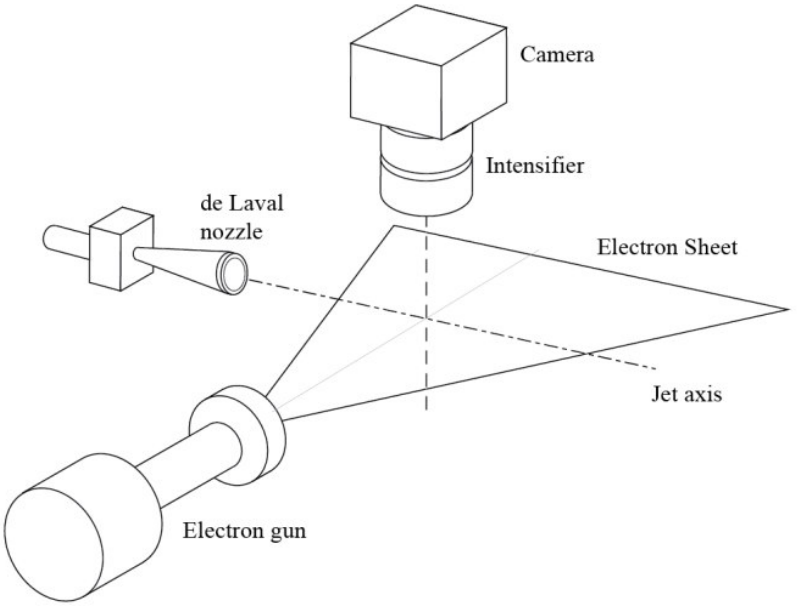

Figure 4.1: Visualization working principle.

In this experiment, focusing on the long scale jets, the electron gun and camera are set on the second ports as shown in figure 4.2. Hence just the first part of the jet, passing the electron sheet, is a free jet and the rest is the interacting jet with the backward flow. This system, which the help of coils, has also the possibility to move the electron beam vertically to capture different 2-D sections from 3-D flow in each desirable vertical position, but here the plane is just set in the middle of the jet flow.

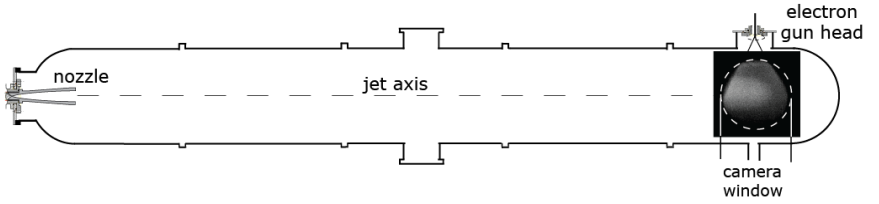

Figure4.2: Schematicview of the vessel; the electron gun and camera can be mounted onto two ports and optical windows.

4.2. Image Processing

Image-based measurement methods and also image processing techniques are becoming increasingly common in fluid dynamics and are seen in applications ranging from low subsonic to hypersonic flows. This section focuses on the use of image processing methods for investigations of hypersonic jet flows; indications about the jets propagation and their resulting morphologies are obtained by means of several techniques carried out on the fluorescent images. The main topics presented in these subsections are treatment of the dark images, an improved measurement technique for the moving structures velocities, an image processing method for denoising and reconstruction of jet images, and finally the technique for measurements of the jet spreading angles and density measurements.

4.2.1. Dark Image Treatment

The resulting images from the camera show that the captured plane, created by the electron sheet, is not perfectly uniform. The left panel of figure 4.3 shows an image of the electron sheet without presenting of the jet. As is obvious an oblique dark strip exists in the imagedue tothe low-response pixels on the CMOS sensor of the camera which leads an output level drop in a narrow area. However, they still absorb some light and thus cause a drop in the illumination level in a narrow area.

This flaw can severely limit the quality of the images when the jet appears. It is removed with a standard technique based on a multiplicative compensating function, because absorption of the light is proportional to the population of the gas molecules and the intensity of the strip varies with the signal intensity. A model for multiplicative function to compensate these distortions is given in the equation below.

$$f(x) = s(x) \cdot n(x) \qquad (4.1)$$

The desirable (uncorrupted) image is denoted by s(x), which in our case s(x) should be a uniform plane, the dark strip processes by n(x), and the acquired image(corrupted) by f(x) (figure 4.3-a). To find uncorrupted image (s(x)), the matrix of dark strip(n(x)), should be found and then by dividing pixel by pixel of f(x) by n(x), uniform image is obtained. Let rewrite the last formula in the new format in 4.2:

$$s(x) = f(x) \cdot n^{-1}(x) \qquad (4.2)$$

which $n^{-1}(x)$ is a compensating matrix. For this purpose s(x) is defined as a uniform image; a matrix with the mean pixel value of acquired image added to the same variance distribution of that image. So if the matrix of a uniform image (figure 4.3-b) is divided (pixel by pixel) by the acquired image (figure 4.3-a), yields the compensating matrix; $n^{-1}(x)$, which is shown in figure 4.3-c. This matrix should multiply to all other images to remove this dark tape (see [65] for further details).

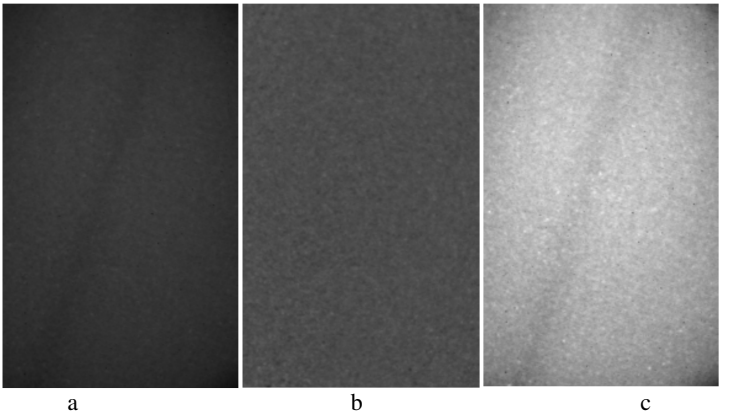

a b c

Figure. 4.3: a) original image, b)desirable uniform image, c) image of compensating matrix

4.2.2. Moving structures velocities

In order to obtain the details of the jet morphology, captured images for each given test, are reconstructed in such a way to display the continuous propagation of the jet flow. For this goal, the movement of structural flows between consecutive images is obtained and then images are juxtaposed according to the flow movements. In other words, it is necessary to know the velocities of the flow among images to reconstruct and display the continuous flow.

In our work, the applied approach in order to measure the flow motions is based on the advanced correlation techniques. It is modified and developed techniques of the correlation techniques used in 2-D PIV. Particle Image Velocimetry (PIV) is a whole-flow-field technique which provides instantaneous velocity vector (two velocity components) for the measurements in a cross-section of a flow. The main principle in PIV is according to the correlation technique applied in sub-sections of the target area of the particle-seeded flow between two light pulses; the flow is seeded by particles and regarding the fluid under test, it is assumed that the particles follow fluid elements without affecting the flow itself. Then the flow is illuminated in the target area with a light sheet. Here the camera captures each light pulse in separate image frames. Once a sequence of two light pulses is recorded, the images are divided into smaller subsections. The subsections areas from each image are cross-correlated with each other; pixel by pixel. The correlation operator produces a signal peak, identifying the common particle displacement. Indeed the main application of this operator is in signal processing which cross-correlation is a measure of similarity of two waveforms as a function of a time-lag applied to one of them. If the signals are vectors, by cross-correlation shifting along vectors is measurable.

An accurate measure of the displacement in PIV-tests and thus also the velocity is obtained by sub-pixel interpolation. In other words the velocity vectors are derived from subsections of the area of the particle-seeded flow with measuring the movement of particles between two light pulses.

In this experiment, the jet flow is not seeded to trace them with the same performing technique in PIV, but an alternative method, based on the similar technique in a two dimensional visualized flow, is used; the illuminated flow due to electron sheet, is visible in such a way that the jet flow in a finite domain can be captured. A series of images of the flow are recorded on consecutive frames (e.g. film). Then cross-correlation technique is used between some rows of consecutive images to find the movement of the flow along the recorded frames.

In general for discrete functions, f and g , the cross-correlation is defined as:

$$(f * g)[n] \overset{def}{=} \sum_{m=-\infty}^{\infty} f^{*}[m]\, g[n+m] \qquad (4.3)$$

In our work, cross-correlation is used for images; For instance consider two consecutive frames where the jet head is appeared, this frame are represented by

the relevant pixel matrices. Here to measure the moving structure, the movement of the intensity of the middle row, marked in figure 4.4, is considered.

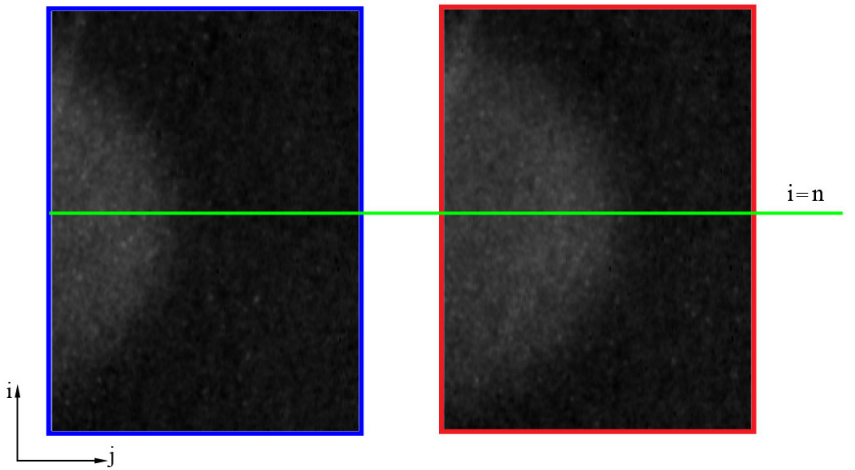

Figure 4.4: A pair of successive images; the middle rows are used for the correlation.

These two rows in consecutive frames actually are two vectors or two discrete functions which call them f and g. Valued vectors f and g differ roughly by an unknown shift along the x-axis (figure 4.5). One can use the cross-correlation to find how much g must be shifted along the x-axis making it identical to f. The formula essentially slides the g function along the x-axis, calculating the integral of their product at each position. When the functions match, the value of (f * g) is maximized. Because when peaks are aligned, they make a large contribution to the integral.

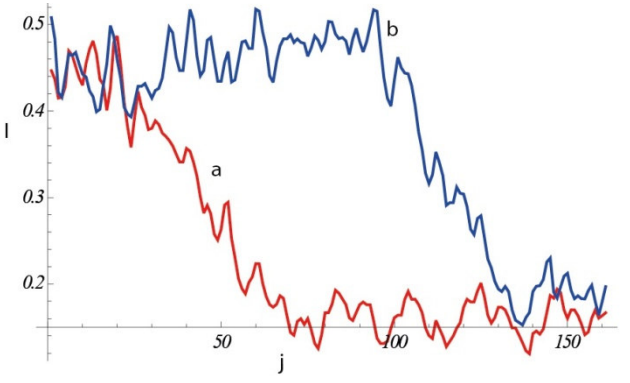

Figure 4.5:Image intensities (pixel values) vs pixel positions of the 2 images inthe middle rows.

Figure 4.6 shows the correlation for these two rows and is obvious the peak is not so certain, because the second curve is not just a translation of the first one and it causes to have wide uncertainty for the intensity-displacement.

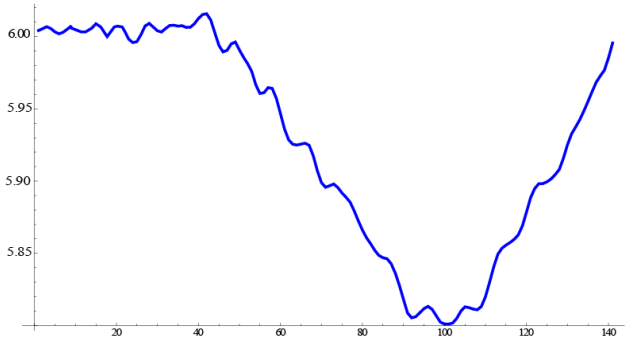

Figure 4.6: The integral correlation curve from curves taken in 4.5.

In order to reduce this uncertainty, another operator,a cross-reflection of the curves, is done with respect to the common origin and this gives rise to the new curves. These new curves as are shown in figure 4.7 are generated by adding another mirrored curve. The correlation can now be calculated as usual, (see figure 4.8),

$$f_j = a_j \mathbf{U}\, R(b_j),\quad g_j = b_j \mathbf{U}\, R(a_j) \qquad (4.4)$$

where R is a reflection or mirrored operator.

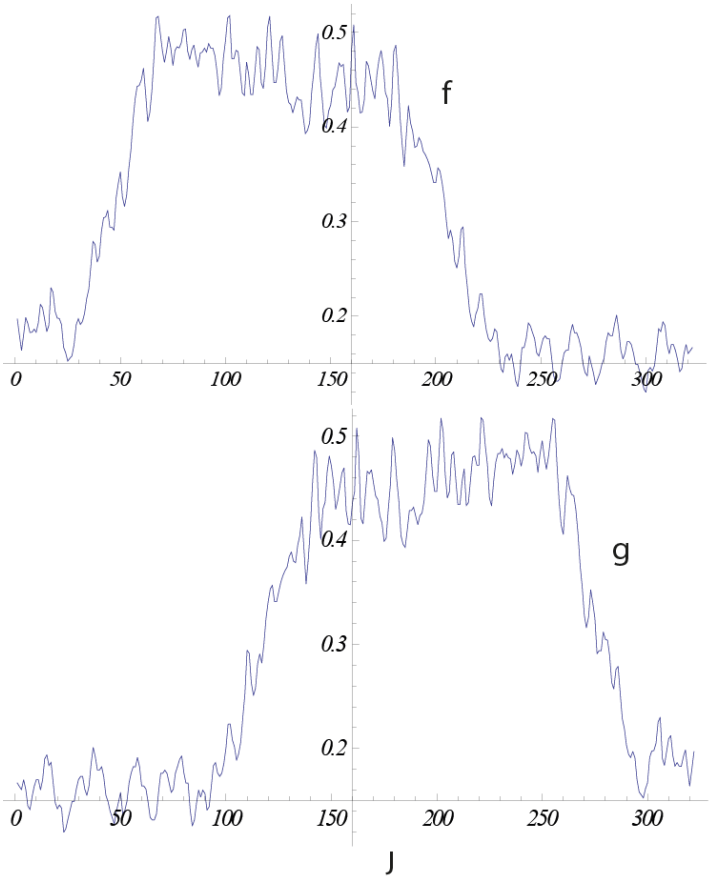

Figure 4.7: Cross-reflection of the curves taken in figure 4.5

Now the correlation between these new curves is obtained and the maximum correlation is clear. When the functions match, the value of Y component is maximized (figure 4.8). The reason for this is that when these two curves, f and g, are aligned, they make a large contribution to the integral.

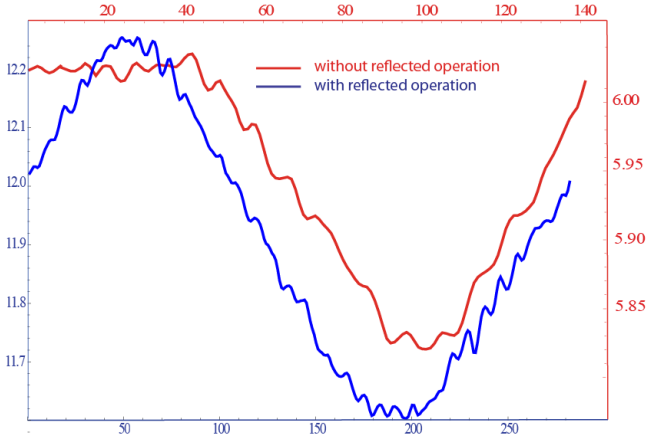

Figure 4.8: The integral correlation curves with and without reflected operation

The X component of the peak shows the shift of two vectors or in other words the displacement of the jet head among two frames, then by juxtaposition, jet image is reconstructed. Resulting velocity is simply obtained by dividing the displacement to interframe time. Figure 4.9 shows two samples of juxtaposed images of two consecutive images.

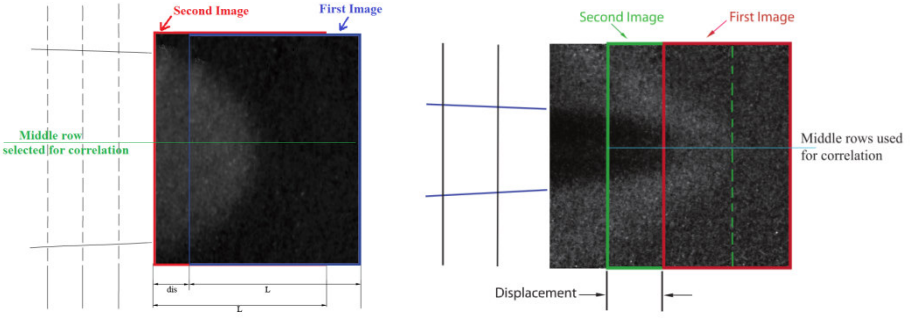

Figure 4.9:Two samples of juxtaposed images of two consecutive images.

The accuracy of this velocity measurement generally depends to a limited extent on the image noise and to a greater extent on the displacement of the structure under test during the image exposure time (influencing theoverlap between two consecutive frames). Here, the exposure cannot be lowered as desired because of the required light level; therefore the uncertainties on the measured velocities may become remarkable, in particular for faster jets. Because of these uncertainties, the

velocity measurement could have maximumuncertainty of 20% which is considered as error in the results of chapter 5.
This technique also is used to measure moving structures in the rest of the jet but for them should care to pick a right row for correlation measurement. There are some instabilities on the mixing layer which are mainly subjected for Kelvin-Helmholtz instabilities (it is explained in chapter 5), and correlated rows should be selected on the mixing layer. Figure 4.10 shows a jet flow after impacting the end of the vessel,which the instabilities are presented. Here two rows are selected on the boundaries, the technique is applied for both and the displacement is the averaged one.

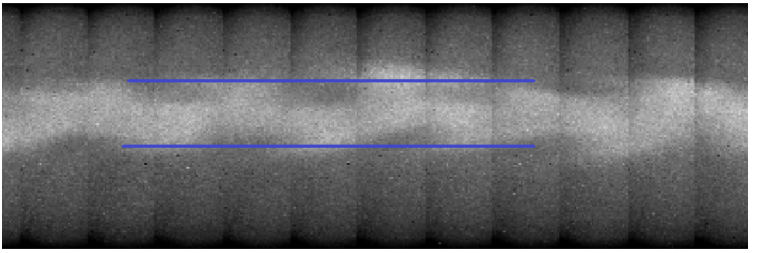

Figure 4.10:Instabilitiesof the flow in the rest of the jet.

But sometimes obtained displacement by this technique is not so accurate, because there are 3-D instabilities rotating and changing shape along the jet. In this case different displacements in different locations must be correctly reported, and the jet structure can be spatially reconstructed by the juxtaposition of shifting parts. Furthermore, the velocity of these instabilities varies along the jet and in the worst case it is so fast that jet structures do not have any overlap in two consecutive frames, so that the shift is greater than the frame width and cannot be measured. In these cases a manual adjustment is performed to find the best juxtaposition which results a continuous development of the flow. Sometimes this manual adjustment is applied to the jet heads which their velocity, regarding the sampling frequency, is very high. Figure 4.11 shows a sample of this kindthat jet head does not have enough overlap in two consecutive frames, so the flow shifting is done manually leading to continuous reconstructed flow.

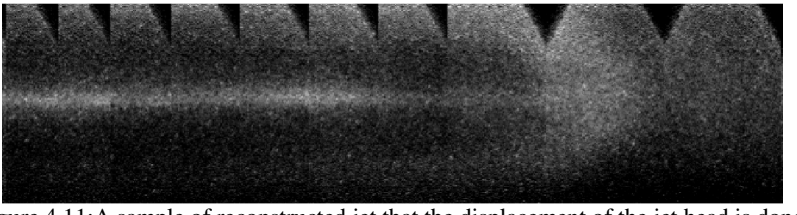

Figure 4.11:A sample of reconstructed jet that the displacement of the jet head is done manually.

In other cases, the structures have shifted lower than the frame width but they fall on the border of the electron sheet: in these cases, the reconstructed image is not continuous and there is an undetected region between frames which appears as a dark border between mosaics of images. The upside of the reconstructed jet taken in figure 4.11 is due to this reason.

4.2.3. Image Filtering

This section focuses on filtering the fluorescent images from the fluctuations. Figure 4.12 shows the raw images of a jet without any treatment.

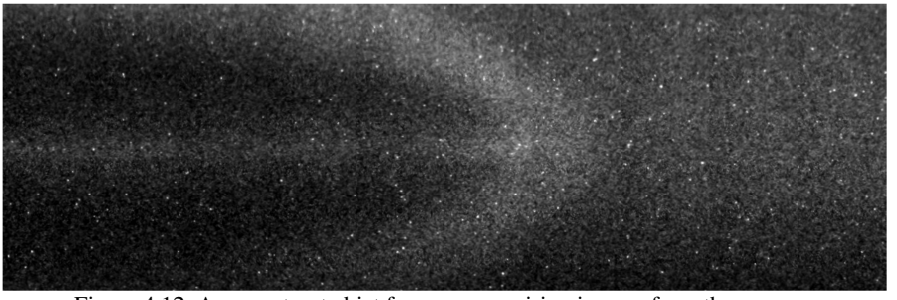

Figure 4.12. A reconstructed jet from raw acquiring images from the camera

As is obvious in figure 4.12, image is not so smooth and is disturbed by some random fluctuations. These noises, defined as the uncertainty of intensity, are due to the statistical and the accumulative nature of photon detection owing to the statistical quantum fluctuations, and are the variation in the number of photons sensed at a given exposure level. These noises may be reduced by increasing the sampling rate of image acquisition or increasing the intensity and frequency of the electron beam, but this approach is often impractical for our imaging because of the problems of jet movements, photo bleaching, and radiation damage. To attenuate this noise, inpainting filter and dynamic high pass filter, are used.
Imageinpainting is almost a new and important topic in image processing which is the technique of reconstruction a damaged image in an undetectable form. In our case, the undetectable regions are the locations of random fluctuations which will be explained in section 4.2.3.1.
Here the common algorithms to restore the damaged images are introduced and after our performing algorithmis described.Reviewing the literatures [66], several restoration algorithms could be found which they address the problem of filling in missing data from different points of view. They can be categorized into four groups:
1.Partial Differential Equation (PDE) based algorithms.

2.Structure-based restoration.
3.Convolution- and filter based methods.
4.Texture synthesis models.

Partial Differential Equation (PDE); it's based algorithms deal with connecting edges and discontinuities. Some complex approaches of this method are proposed to join interpolation of grey levels and gradient/isophotes (line of equal grey values) directions. This method iteratively propagates information from outside of the area along isophotes in the selected region for inpainting. In order to perform propagation in the right direction of the isophotes, the direction of the largest spatial gradient, obtained by computing a discretized gradient vector, is applied. (for more details see [67,68]).

Structure-based restoration: This approach firstly reconstructs edges which separate smooth or texture regions, and then the information, surrounding sketch lines, is restored according to the patch-based matching algorithm. Finally missed regions are reconstructed by exemplar based method which is under constrained of the surrounding sketch(for more details see [69]).

Convolution- and filter based methods; here the inpainting is performed by convolving the damaged image with a proper kernel. A fast digital image inpainting method is proposed which depends on convolution operation and uses a diffusion mask which is repeatedly convolved to the missed regions (for more details see [70]).

Texture synthesis based models; this method tries to fill the damaged regions by a sample of the available data of the image and such that statistics of neighbouring current pixel matches for statistics of the damaged region. One proposedmodel is nonparametric texture synthesis model to inpaint textural images; the similarity between their local neighbourhood and the surrounding neighbourhoods is used to restores missed pixels. In his technique, one is randomly selected from candidate neighbourhoods and the value of central pixel is used at the current location. There is some modification in this method by a patch-based algorithm (for more details see [71]).
In our case the used method isa directional median filter which is the last category; Texture synthesis based models. It is described in the following section.

4.2.3.1. Directional Median Filter

Torestore the damaged regions, due to the fluorescence phenomenon, an algorithm is proposed using statistical information to reformthe noisy pixels.This method simply replaces the value of a pixel with the median of the intensity levels in its neighbourhood; the median value of the known pixels in each direction is

calculated, and then, a damaged pixel is replaced by the median of the obtained values.
The median filter is one of the best-known order-statistic filters in image denoising topic. This filter also could be applied to moderate considerably the impulsive noise. This inpainting methodsmoothens the images while do not destroy edges and other details in the images [66]. Figure 4.13 shows the working principle of a directional median filter; first, it determines the median in different directions. Then, the median of the obtained medians is considered as the output replacing in the missed pixel; due to acting the filter in several directions, instead of a neighbourhood, results better edge preserving than a conventional median filter.

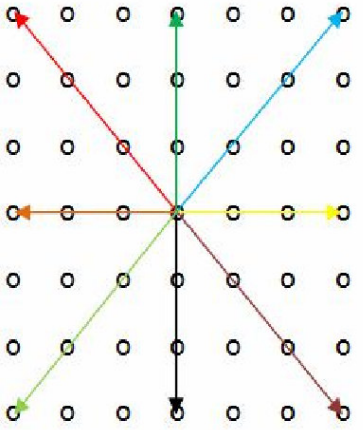

Figure 4.13: Aspect of a directional median filter.

Different steps of the algorithm are as follows: after determining the damaged regions, the algorithm considers two pixel thick boundaries of the distorted region. For each damaged pixel on the boundary, known pixels in different directions are selected. Then, the median value in each direction is determined, and finally, the damaged pixel value is considered to be the median of these medians.
Once, all of damaged boundary pixels are reconstructed, the algorithm has finished its first iteration. In the next iteration, the new boundary, regarding the results of the first iteration, is calculated. Then in a similar manner, the boundary of pixels is reconstructed. The method needs two iterations for an image without complex edges, but for regions with complex edges it will need a larger number of iterations.To evaluate the performance this method, it is tested on a sample of damaged image; the qualitative results for this sample is shown in figure 4.14. Figure 4.14-a shows an image with a large damaged region and figure 4.14.b displays the inpainted image obtained by the proposed algorithm. As it is obvious the proposed algorithm provides very adequate results in the large damaged

regions. To inpaint this image, just three iterations are performed to achieve this acceptable quality as the output in figure 4.14-b.

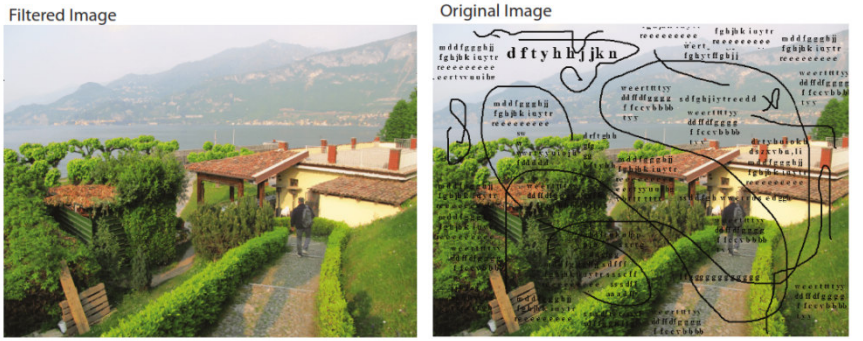

a b

Figure 4.14: a) an image with a large damaged region, b) the inpainted image

In cases where complex edges are included in an image, it is only sufficient to change directions or consider more directions in order to complex edges are preserved. In our images that jet moves horizontally, two vertical directions, up and down, are deactivated to yield better results as the reconstructed jet along its progression.

But about the first step, which is about the determination of the damaged regions, or in other word the locations of the noisy pixels, a gradient filter is used. The gradient filter captures the random fluctuations which are inherently due to the fluorescence phenomenon. When their locations are obtained, inpainting filter is applied to their noisy regions. Figure 4.15 shows this process, and as is obvious, this method perfectly removes the random noises.

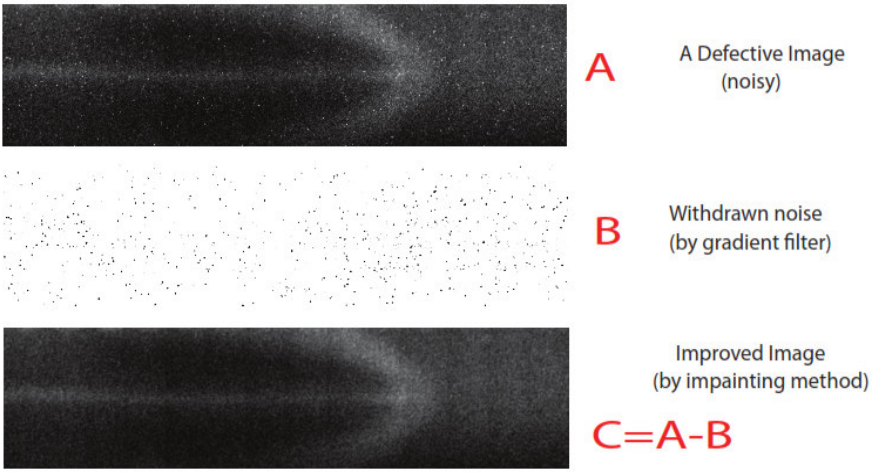

Figure 4.15: a sample showing application of impainting technique in recounstacted jet.

However, the proposed algorithm also can be used for the dark borders between reconstructedimages of the fast jets where the flowdoes not have enough overlap between frames. Figure 4.16 shows a sample of the jets which the borders can be inpainted with the directional median filter.

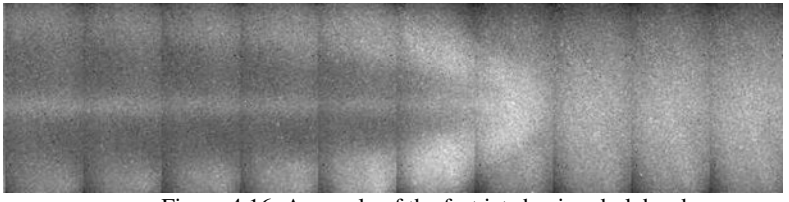

Figure 4.16: A sample of the fast jets having dark borders.

In this sample the reconstructed jet is not perfectly continuous and there is a undetected region between frames, so the border can be considered as damaged regions, as shown in figure 4.17, and then inpainting technique is used to fill the missed data.

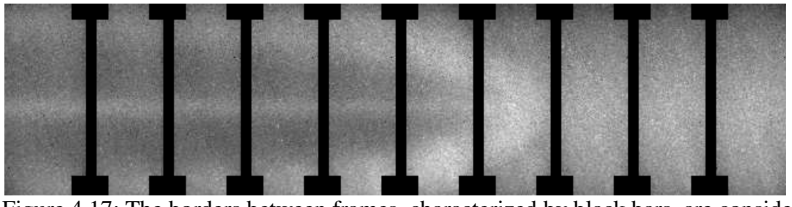

Figure 4.17: The borders between frames, characterized by black bars, are considered as the undetected region.

For this case, due to the horizontal movement of the flow, the vertical components of median algorithm are deactivated in all iterations; figure 4.18 shows the given principle of the median filter.

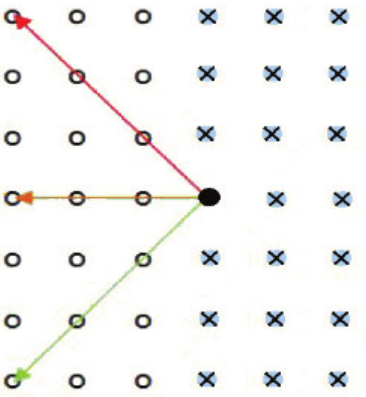

Figure 4.18: Aspect of a directional median filter based on almost horizontal directional median filters.

In the first iteration, the median value of three known pixels in the boundary of undetected columns in three directions is calculated, and then the unknown pixel is replaced by the median of the obtained values (figure 4.18). This process, limited to three directions, let data propagate longitudinally from both sides of the missed data so that the region under processing is filled. In the next iterations, this process is repeated again along these three directions and the obtained values are replaced. The output results obtained with the given directional median filter is illustrated in figure 4.19; as can be seen the resulting image does not seem real, is looks somewhat artificial. Nevertheless it is possible to apply this method for some fast jets, when undetected regions are very small with respect to the jet diameter, obtaining visualizations of reasonable appearance. This method instead has been not used for the quantitative results of chapter 5, that are based on juxtaposed frames with continuous borders.

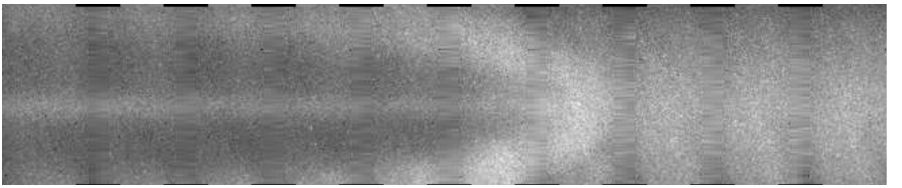

Figure 4.19: The same jet as shown in figure 4.16 but filling the undetected region between frames with median filter's algorithm illustrated in figure 4.18.

4.2.4. Inpainting and Fourier Filter

The last procedure,after filtering the noisesdue to the fluctuations of florescencephenomena, is to attenuate the smallerfluctuations. Hence a dynamic high pass filter, filtering low amplitude components in the Fourier space, is used to smoothen the reconstructed images. Figure 4.21 shows the effect of this filter, and as is clear, the image is smoothed by decreasing the random disparity between pixels.

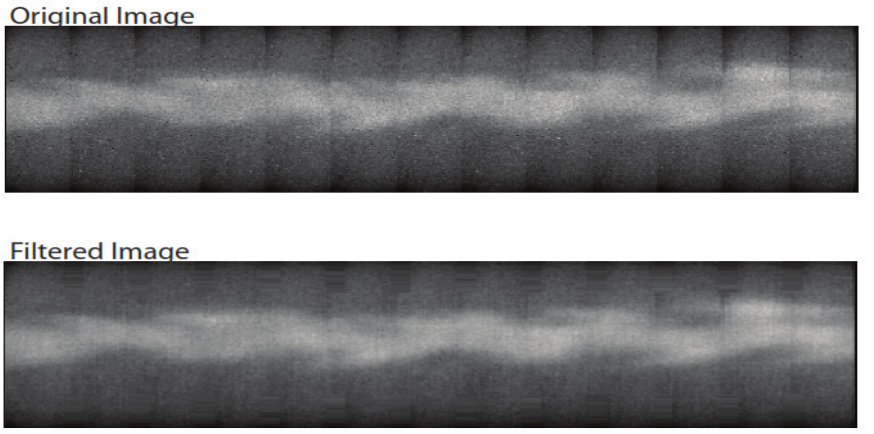

Figure 4.21: Two filters, dynamic high pass filter and inpainting are applied to the original image and yielded filter image

4.2.5. Spreading angles

After the reconstruction of the jet image, the spreading angle of the jet core can be measured. But for some jets it is so difficult to specify the jet core. Figure 4.22 shows one of these cases which backward flow has surrounded the jet beam.

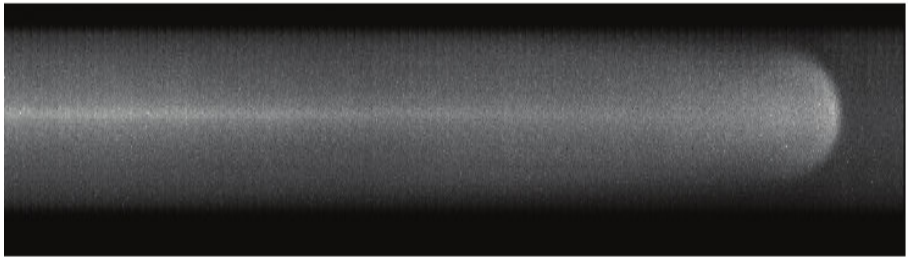

Figure 4.22: A sample of reconstructed heavy jet flow.

For this measurement, several columns of the reconstructed image, located just behind the jet head, are selected (figure 4.23). Then the averaged curve of pixel intensity of the columns is obtained (green curve in figure 4.24). In order to find the jet core, a special criterion is defined according to the derivative curve, based on the fact that, in the vicinity of the jet core, the derivative is high because of the sharp variations in the pixel intensity. So the boundary of the jet core is conventionally assumed to be bounded by the highest variations of intensity. In figure 4.24 the dashed lines show the places of the highest derivatives on both sides of thejet, and the distance between these vertical lines represents the jet core width. Then, the spreading angle can be obtained by comparison with a similar measurement of the jet core width at the nozzle exit.

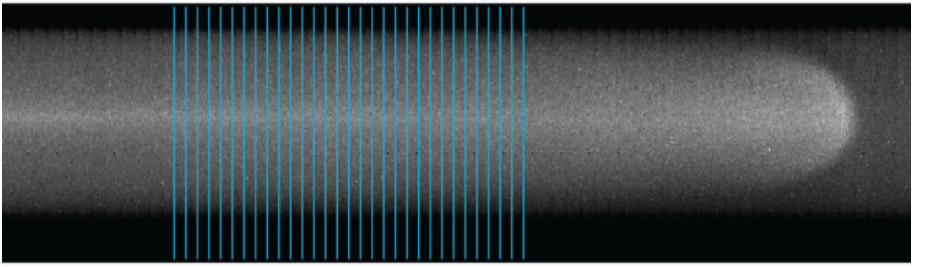

Figure 4.23: Lateral selected columns of reconstructed image, behind the jet head.

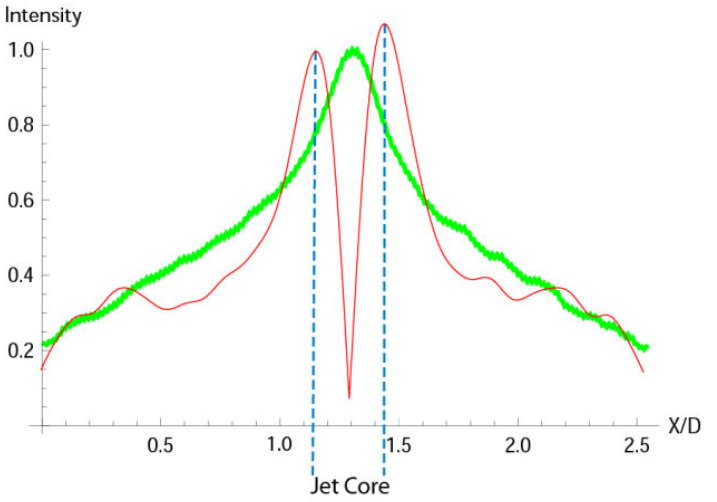

Figure 4.24: Green curve: averaged curve of pixel intensity, Red curve: derivative of green curve, absolute value.

4.2.6. Density measurements

The method for density measurements is based on the fluorescent emission from a gas excited by an electron beam.
Fluorescence occurs when the molecules excited by the electrons return to the groundstate and give back energy in the form of emitted light. The energy of incident electrons can also be transferred to translational molecular degrees of freedom or other molecular excited states (quenching collisions).
The relation between the radiation intensity I and the numerical density n of a gas can be defined as[48,72]:

$$I = \frac{k\,n}{1 + h\,n} \qquad (4.5)$$

In relation (4.5), the **k n**factor accounts for the proper fluorescence phenomenon where **k** is a constant that includes the sensitivity of the measuring system, whilst the term **h n** in the denominator accounts for the loss of fluorescence caused by quenching, and **h** is a specific coefficient of the nature of the gas which depends on the temperature:

$$h = 2\,n\,\sigma^2 P_{jk}^{-1} \sqrt{4\pi R_{gas} T} \qquad (4.6)$$

Where σ is the quenching collision diameter, $P_{mn}$the spontaneous transition probability, T the temperature and $R_{gas}$the gas constant). Figure 4.25 displays a typical fluorescent emission at constant T.

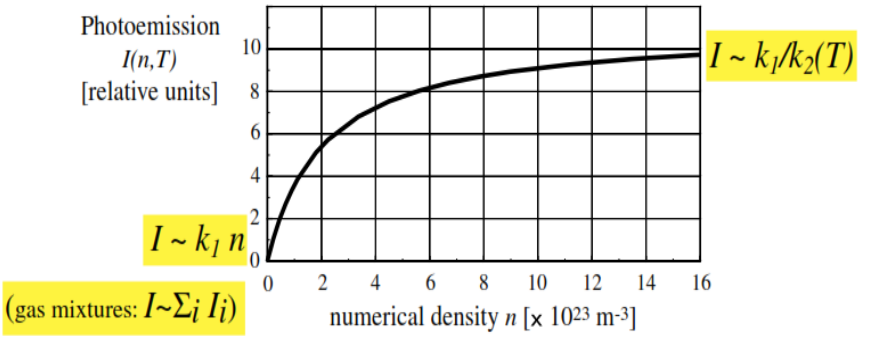

Figure 4.25: The typical fluorescent emission vs. Numerical density at constant T. [48]

For relatively rarefied gases, that is, those in the small numerical density limit, equation (4.5) shows that I is proportional to n, whilst for higher densities, the emission encounters an asymptotic limit (saturation):

$$I \propto n \quad as \quad n \to 0$$
$$\lim \to I = const. \qquad (4.7)$$

At the low pressures considered here (1.5 < p < 200 Pa), we can approximate equation (4.5) as:

$$I = k\,n \qquad (4.8)$$

Since **I** is a spectral superposition, this relation also holds for the three colours acquired and stored in the digital colour image yielded by the camera. Three constants depending on the spectral emission range associated to each colour (RGB) can be introduced, in a treatment based on the use of colour cameras, leading to information on the gas species present in a mixture [48,72]. In this study, however, we use monochrome images. Thus, it is possible to write Radiant intensity **I**vs numerical density n which is just **I** is gray level of fluorescent image. Radiant intensity **I**vs density ρ is similar, of course:

$$I = \frac{K_1 \rho}{1 + K_2(T)\,\rho} \qquad (4.9)$$

and for low densities the law can be approximated as:

$$\mathbf{I} = K_1 \rho. \qquad (4.10)$$

Real intensities are affected by a noise component, so that:

$$\mathbf{I} = \mathbf{I}_N + K_1\rho \qquad (4.11)$$

and in a real measurement, the intensity is related to the region of interest, which is a sector of angle α (opening of the electron blade), so

$$I = \frac{C}{\alpha}\left(h_N + h_1\rho\right) \qquad (4.12)$$

Both the noise component and the signal component are proportional to the beam current:

$$I = \frac{D_i}{\alpha}\left(h_N + h_1\rho\right) \qquad (4.13)$$

andfinally, the two h-constants are related to the MCP voltage of the light intensifier, in a way that can be expressed as

$$\begin{aligned} h_N &= \alpha_1 + \alpha_2 V + \alpha_3 V^2 \\ h_1 &= b_1 + b_2 V + b_3 V^2 \end{aligned} \qquad (4.14)$$

For measuring the density, the coefficientsD, α_i and $b_i$must be obtained by calibration on known gas densities. Finally, the density measurements are obtained by inverting formula (4.13).
Figure 4.26 illustrates a sample of density measurement along the middle line of the shown jet.

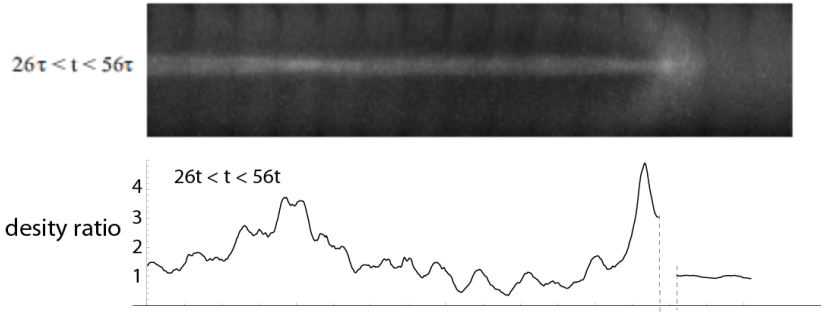

Figure 4.26: A sample of the light jet flow and its axial density for the jet; density is expressed in nondimensional form as density ratioreferred to the unperturbed ambient

Chapter 5

5. Results

5.1. Visualizations

A large set of the jets has been studied in this experiment: the Mach numbers range from 7 to 21, and the density ratio η from 0.5 to more than 100. Because there is no other experiments on long scale jets, in order to better exploration of jet morphology, a number of jets has been compared with the corresponding numerical simulations; the simulations are obtained by the astrophysics research group at the University of Torino; the employed code, PLUTO, is a freely-distributed software for the numerical solution of mixed hyperbolic/parabolic systems of partial differential equations (conservation laws) targeting the high Mach number flows in astrophysical fluid dynamics. These numerical simulations aregenerally obtained over a 2D cylindrical domain in the coordinates (r, z), normalized over the initial jet radius r_0 taken at the nozzle exit. 3-D simulation is possible, and performed in particular cases [73].

In the experimental visualizations, the light intensity is proportional to the localdensity, whereas in the corresponding numerical simulations the density maps are intentionally produced. Each experimental image is obtained by juxtaposition of time correlated frames (see section 4.2.2) on a short time range including the instant chosen for the corresponding numerical image.

Another point about the following results which in some cases compared with simulations is; the simulations generate snapshots of the whole jet,while they are compared with the mosaics of images taken at subsequent times. Hence to have a fair comparisonof simulations and experiments, and also to avoid producing 'frozen' reconstructions, the laboratory reconstructions are made ofa limited number of juxtaposed slices by considering the time scaleof the jet, i.e. the presented imagesdo not cover a time so longthat the jet shape can vary dramatically over it [76].

Figure 5.1 shows the parameter space of the density ratio via Mach number for different couple of jet and ambient gases.

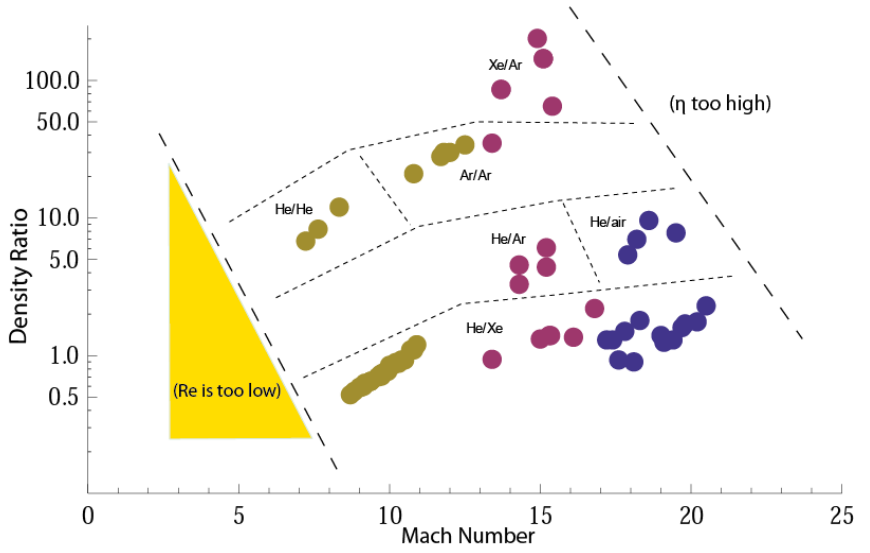

Figure 5.1.the parameter space, Mach number vs density ratio for different couple of jet and ambient gases

The yellow region in figure 5.1 is the experiments performed in the Mach 5 range, although the experiment in this range did not yield proper results as the long-scale jet, but highlights an important aspect of the physics of hypersonic jet flows.Let have briefly feedback to chapter two; three parameters influence on the morphology of "hypersonic pressure matched jets"; Mach number, density ratio and length ratio (length to diameter ratio). Hence to reduce the variables to two ones, the length ratio shall be kept in a fixed range (in order of 100). Regarding the Mach 5 nozzle, which hasa small diameter ($\approx$0.6cm), just two sections of the vacuum vessel were used (section 1 and 5 of figure 3.3). But experimental visualization shows even with decreasing the vessel length to the shortest possible one, the jet flow does not presentcoherently when reach to the electron sheet, and owing to the mixed turbulent layers, the jet collimation destroy. This result is also obtained by numerical simulation [74]. This behaviour is due tothe relatively low Reynolds number of Mach 5 jets; for the jets with low Mach numbers ($\leq$ 5), the Reynolds number is much lower than other ranges of Mach numbers (10,15 and 20), which leads the viscous forces overcome inertia forces along a short distance from the nozzle, and the mixed turbulent layers destroys the jet structure and prevent the jet collimation.

Hence, according to the first step of our experiments, done in the Mach 5 range, it is highlighted that for the jet with lower Mach numbers (M $\leq$ 5), due to relatively high viscous forces around the mixing layer, jet flow cannot last coherently for a long distance (long distance; length to diameter ratio more than 100).

Another no explored region in the parameter-space plane of figure 5.1 is the high density regions at Mach 20 range; the results ofMach 15, having a wide range of density ratio, shows the jet morphology changes with increasing the density ratio, but when the density ratio goes higher than 10, its morphologydoes not change. Therefore the experiments of the Mach 20 are performed for a shorter range of the density ratio (up to 10) which is in the range of interest.
In the following, a number of the reconstructed images of the flow visualization in the interesting range of Mach numbers and density ratio are taken.

5.1.1. Results showing effective parameters on the jet flow

Here several cases, having wide-ranging of density ratio and Mach number, are selected to analyse the morphology of the jet flow. In regard to the figure 5.1, the widest range of the density ratio is available at Mach 15 range. Therefore first this effect is investigated in the Mach 15 range; see figure 5.2.

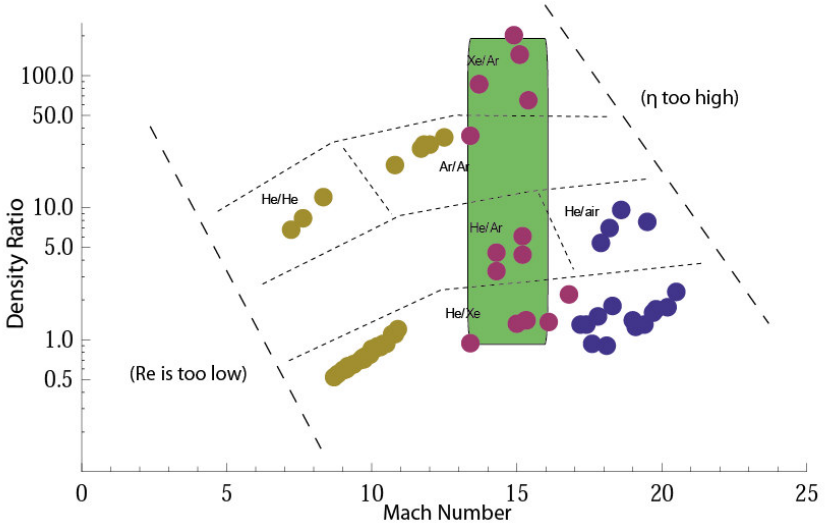

Figure 5.2. The selected region in the parameter space, for exploring the influence of the density ratio

In the first subsection, five cases of the jet flow with different jet-to-ambient density ratios at fixed ranges of Mach number (Mach 15), are compared; the first case is slightly under dense jet, the second is slightly overdense, the third is in the

intermediate range of density ratio, forth one is overdense jet flow and last case is highly overdense jet flow.
In the second subsection, three cases, having a similar density ratio of underdense jets, at different Mach numbers, are selected (figure 5.3), so the effect of Mach number has been studied.

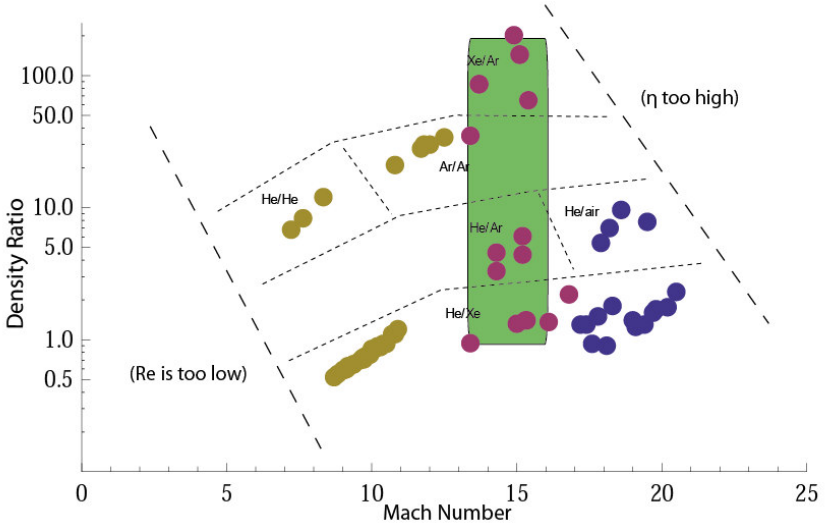

Figure 5.3. The selected region in the parameter space, for exploring theinfluence of the density ratio

In both of these subsections, the beam pumping phenomenon has been seen; to prove and better understand, in some cases the experimental results are compared with existing numerical counterparts [75,76].
As far as the jet evolution is concerned, in the following the physical time is expressed time units of τ , which is defined as the ratio between the jet radius at the nozzle exit r and the speed of sound inside the jet and in the nominal conditions. So the time scale depends on the jet under test and the given nozzle, and is variable; for instance of Mach 15, it is of the order of 1ms for the pressure-matched heavy jet (overdense) and 0.2 ms for the light jet (underdense). The lengths also are scaled in units of r, which is a constant due to the each given nozzle.

5.1.1.1. The effect of density ratio in fixed Mach number

Here five jets with different jet-to-ambient density ratios at a fixed range of the Mach number, Mach 15, are compared. In the first case, the experiment is performed for a slightly underdense jet; η=0. 9. Figure 5.4 shows a helium jet traveling in a xenon ambient, it is a slightly unmatched jet obtained by setting a stagnation/ambient pressure ratio $P_0/P_a=3.88\times10^4\pm 20\%$ and an ambient pressure P_a =10.0 ± 0.1Pa. These parameters lead to a jet with Mach number M=13.4 at the nozzle exit and a density ratio η=0.9, thus the jet is slightly underdense in comparison with the surrounding ambient. The space unit is the exit radius of the nozzle r= 0.03568m. Figure 5.4 shows this light jet before impact with the end of the chamber; one sees the bow shock, the thick cocoon extended along the jet beam which generates a shear that acts on the inner part of the jet. Here the backward flowing cocoon is very large in comparison with the size of the jet core, which is now surrounded in turn by a region of fast expanded jet gas (dark in the image) and by an unstable interface between jet gas and ambient gas. For this jet the core gas velocity v_g can be estimated about (2050±300) m/s, which is simply derived from the relation $v_g = \sqrt{\gamma P_{flow} / \rho_{flow}}$, whilst the measured value of the head structure, by correlation technique, is v_h = (340 ± 70) m/s, so the ratio v_g/v_h is 6.03.

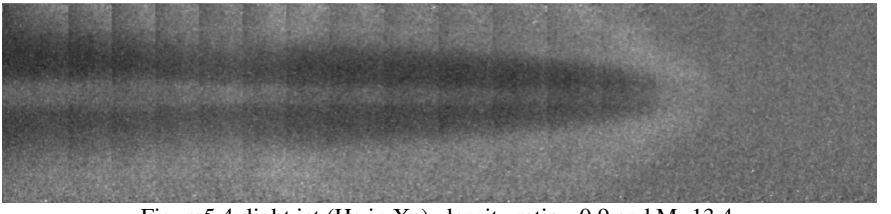

Figure5.4: light jet (He in Xe), density ratio= 0.9 and M=13.4.

The second kind of the jets shown in Figure 5.5 and 5.6 are slightly overdense jets. In the jet taken in figure 5.5, the jet head is so sharp, owing to the heavy xenon ambient which contrasts the light jet advancing.

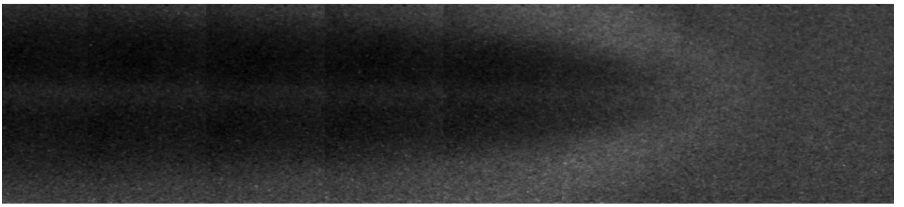

Figure5.5: slightly overdense jet (He in Xe), density ratio= 1.40 , M=15.3.

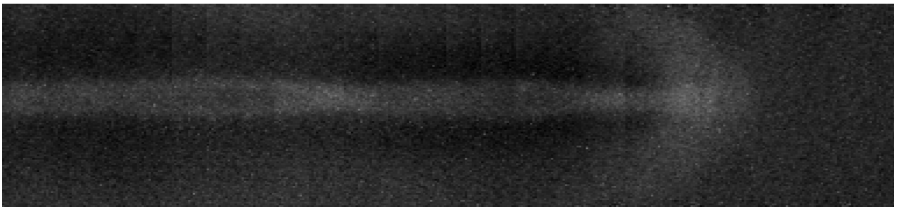

Figure 5.6: Slightly overdense jet (He in Xe) - density ratio= 1.35, M=16.1.

Figure 5.6 shows the jet with almost the same density ratio as one taken in figure 5.5, and roughly similar conditions; ambient pressure P_a=4.0 ± 0.1Pa, stagnation/ambient pressure ratio $P_0/P_a = 7 \cdot 10^4 \pm 30\%$ and Mach number at nozzle exit is 16.1, generating a slightly overdone jet; η =1.35. The jet in figure 5.5 has slightly different ambient pressure and stagnation/ambient pressure ratio which results similar conditions; density ratio 1.40 and Mach number at the nozzle exit 15.3. For the jet shown in figure 5.6 the core gas velocity v_g at the nozzle exit can be estimated the same as jet illustrated in figure 5.5, which is (2420 ± 330) m/s, and the measured value of the head structure is v_h = (490 ± 100) m/s, so the ratio v_g/v_h is 4.94 which is less than the jet in the last case (η =0.9, M=13.4).
As it is obvious, although the density ratios of these jets are similar, here the shape of the terminal/bow shock structure is remarkably different of the jet presented in figure 5.5; in the hypersonic jets, the head shape changes continuously with time, under both free-boundary and vessel-boundary conditions, because of the natural unsteadiness of the hypersonic flow behind the head. This phenomenon, often referred to as “beam pumping”, takes place even if the mass flow is perfectly constant, since it is an inherently unstable phenomenon [75]. Figure 5.7, showing head velocity vs time obtained from numerical simulation [76], indicates that the jet head displacement is not continuous or smooth, even with a regular mass flow, but has a periodic impulsive behaviour; the jet gas, after being decelerated by the terminal shock, is deflected sideways and form a small backward flowing region behind the bow shock, the so-called cocoon, which then mixes with the ambient gas. Again flow passes thorough acceleration phase till facing the next terminal shock, and this trend goes on to make impulsive behaviour.

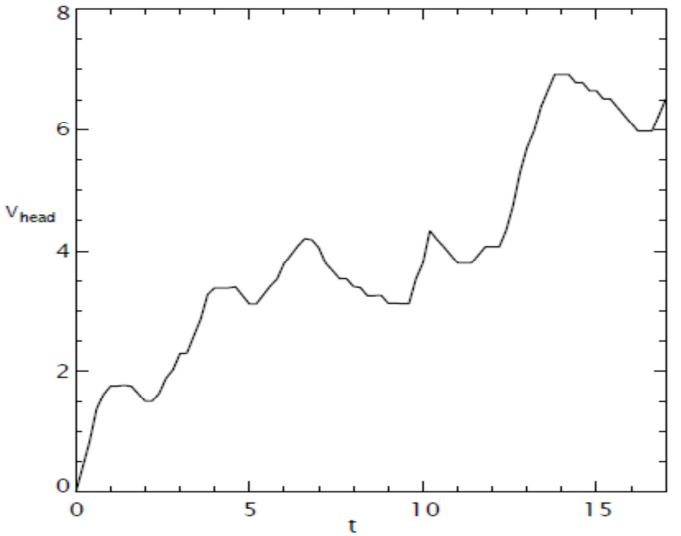

Figure5.7: Jet head velocity in dimensionless r_o/τ unitsvs dimensionless time for the light jet case and outflow lateral conditions [76].

In figure 5.8, the given jet (jet in figure 5.6) is numerically simulated according to the density map whichis normalized to the unperturbed ambient value, also the time unit for this light jet is τ = 0.18 ms[76]; Top panel indicates the jet at time instant t = 15τ. Second to forth panel indicates the jet progression of three time instants. The last panel of figure 5.8 shows the laboratory visualization, juxtaposition of scale correlated frames in a time range including the shown numerical simulations. Figure 5.7 shows the head velocity of this numerical simulated jet and illustrates the "beam pumping" phenomena, which jet head comes ahead by generating two lobes around its sides.

Because the jet head in figure 5.5 has less velocity v_h = (460 ± 100) m/s than one captured in figure 5.6, v_h = (490 ± 100) m/s, and also regarding their shape presented in these captured instances, it could be concluded as follows; the jet head in figure 5.5, having less velocity and sharper shape, is for the instance of the acceleration phase, which can be synchronized with t = 13τ in figure 5.7, and the jet head presented in figure 5.6, having higher velocity and blunter shape, is for the instance of the deceleration phase; synchronized with t = 15τ in figure 5.7.

It is also important to note that the experimental observation of the head structure and of the knots is difficult because of the finite, non-negligible exposure time of the camera, necessary for getting enough light (see section3.3.2).

Figure5.8: Jet head velocity in dimensionless r_0/τ unitsvs dimensionless time for the light

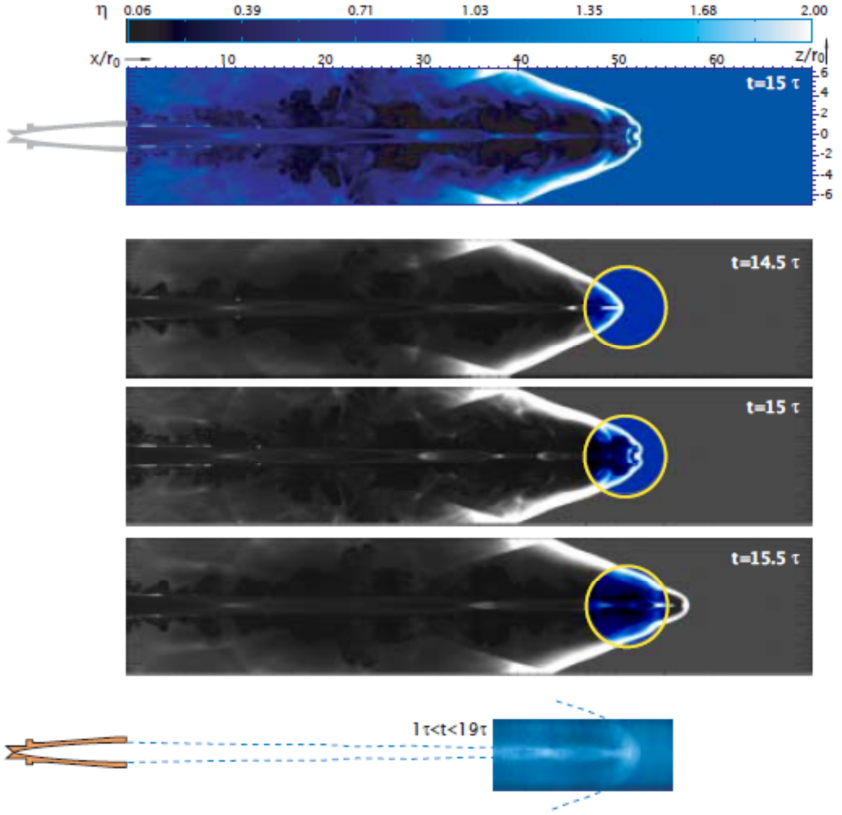

jet case and outflow lateral conditions [76].

The third case illustrated in figure 5.9 is in the intermediate range of the density ratio, η =4.6; Helium jet in Xenon ambient. Here to have a higher density ratio, ambient density and consequently ambient pressure are decreased to p_a =2.5±0.1Pa, which leads to a Mach number of nozzle exit, is 14.3. The measured value of the head structure is v_h = (580 ± 120) m/s and the core gas velocity v_g can be estimated = (2510 ± 250) m/s, so again the ratio v_g/v_h is 4.33 decreased due to the increasing density ratio. Here a bow shock is presented in front of the jet and after the bow shock is just a naked beam lacking cocoon altogether. This trend of losing the cocoon by increasing the density ratio is expected from mass continuity low on the working surface (see section 2.3).

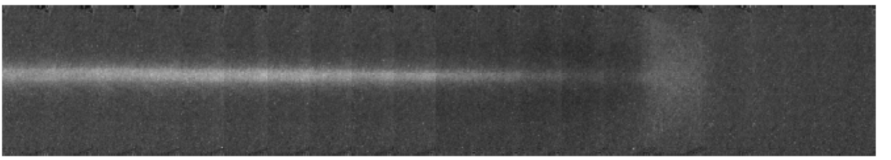

Figure5.9: moderate overdense jet (He in Xe), density ratio= 4.6, M=14.3

The fourth case is about a heavy jet. Figures 5.10 illustrates the evolution of a heavy jet, η=46, propagating through the ambient before hitting the vessel. Here the shape of the terminal/bow shock structure is remarkably different from the previous cases, owing to the heavy xenon ambient which contrasts the light jet advancing.

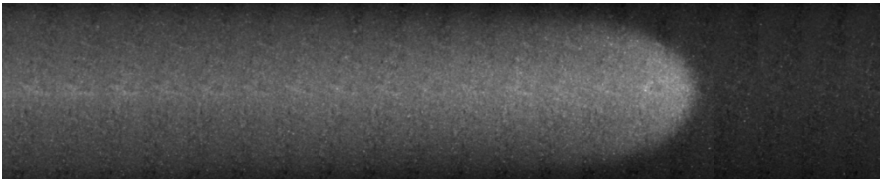

Figure5.10: heavy jet (He in Ar) - density ratio= 46, M=13.7

As it is expected from heavy jets, here we have just a naked beam without cocoon around the head. It is also obtained by the numerical simulations [74]. The estimated nozzle velocity at the exit v_g = (560 ± 60) m/s, and the measured value of the head structure is v_h = (150± 30) m/s, so the ratio v_g/v_h is 3.73 which again decreased by the increasing density ratio.
The last case is a highly overdense jet flow (η=77) in comparison with the surrounding ambient, Figure 5.11 shows the head of a xenon jet travelling in an argon ambient, and at the nozzle exit Mach number M = 15.1.

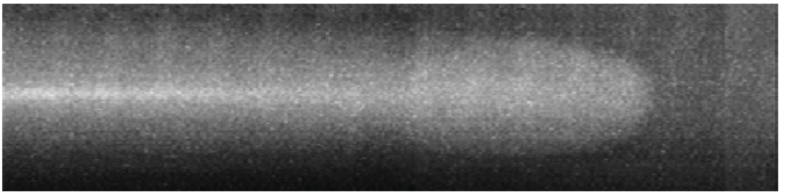

Figure5.11: very heavy jet - density ratio= 77, M=15.1

The jet structure visible in figure 5.11, which has η =77, is almost the same as overdense jet flow shown in figure 5.10 (η =46); it may be interpreted as follows: the jet head is made of a bow shock, travelling left to right, clearly visible in figure, followed by a terminal shock much smaller than the bow shock, and in this

case very close to it, so that it cannot be resolved in the image. On the right of the bow-terminal shock structure, only the unperturbed ambient gas is visible; on the left of this structure, the jet core is clearly visible, it is made of xenon travelling at a velocity v_g which can be estimated about (560±60) m/s. This velocity is larger than the one of the shock structure v_h = (210±50) m/s, measured by correlation techniques. The velocity ratio, v_g/v_h, which shows the jet acceleration along its development,is 2.66. The velocity ratioshows the rational trend as density ratio is increased; the jet acceleration decreases due to increasing the density ratio, because of the opposition of the ambient.
It is clear that the jet shape is getting steady among high density ratio; for confirmation, another sample of highly heavy jet (η=102), is illustrated in figure 5.12; although this jet is not so clear but has the same shape of the jet is figure 5.11 and 5.10, and prove this behaviour.

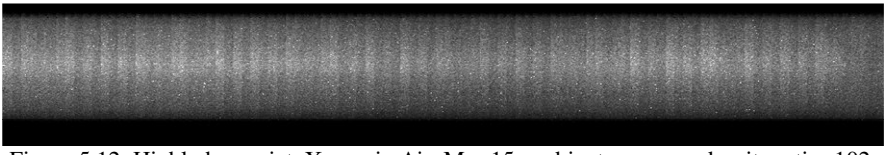

Figure 5.12: Highly heavy jet, Xenon in Air. M = 15, ambient pressure, density ratio=102

The results of these five cases in the Mach 15 range show clearly the effect of density ratio on the jet morphology. The jet with low density ratio, case one (η=0. 9), has a sharp jet head and thick cocoon of backward flowing gas around the jet beam, and with increasing the density ratio in the second case, (slightly overdense jet, η=1.4), the head shape is still sharp but slightly less than one in underdense jet, and also the thickness of cocoon faintly decreases. For higher density ratio in the third case, having an intermediate density ratio (η=4. 6), the bow shock in the jet front changes to the blunt one and the backward flow (cocoon), almost fade away and finally in the fourth and fifth cases, the jets with high density ratios (η =46, 77), it is just a naked beam lacking a cocoon altogether. The visualization of the jets confirms that the jets with density ratio more than 10, have almost the same head shapes [74,76].

5.1.1.2. Underdense jets having different Mach numbers

Here three underdense jets with similar density ratio and different Mach numbers; 9.9, 13.4 and 18.1 are compared to see the effect of the Mach number on the jet behaviour. In these cases to have a low density ratio, Helium was used as jet gas and Xenon as ambient gas and all figures have the same scale.

In the first case, shown in figure 5.13, a helium jet travelling in a xenon ambience, is a nearly matched jet obtained by Mach 10 nozzle. The control parameters (T1 and T2 yielding suitable P_0 and P_a) lead to a jet having at the nozzle exit a Mach number M = 9.9 and a density ratio η = 0.85. The core gas velocity v_g can be estimated about (2000 ± 100) m/s, whilst the measured value of the head structure is v_h = (280 ± 50) m/s, resulting the velocity ratio v_g/v_h = 7.14.

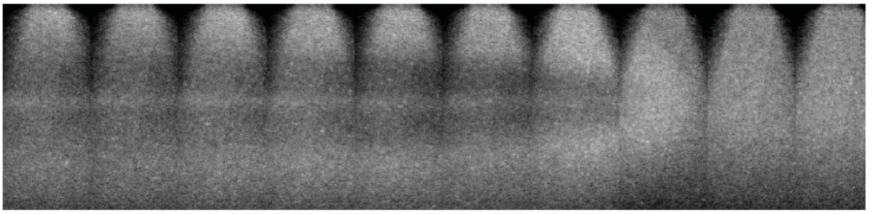

Figure 5.13: light jet (He in Xe), M=9.9 density ratio= 0.8

In this range of Mach number and density ratio (M=10 and η =0.85), several jets were captured and it is observed that the head shapes and also their velocity are not similar, even with the same parameters (same pressure ratio and density ratio);figure 5.14 shows the jet at M=10 and η =0.85, which has similar parameters of the jet taken in figure 5.12. The head shapes between these jets (figure 5.13 and 5.14) are different; in the jet captured in figure 5.14 the measured value of the head structure, having blunt shape, is v_h = (155 ± 40) m/s whilst for the jet in figure 5.13, the jet head velocity, having sharp shape, is measured about (280 ± 60) m/s.
This behaviour can be interpreted due to the beam pumping phenomenon [75], as follows: the jet head shown in figure 5.14, is the captured instance of the flow just after deceleration phase which facesthe terminal shock, and the jet head in figure 5.13, is for the instance at the end of acceleration phase, which have a maximum velocity among an impulsive phase. If we back to figure 5.7, illustrating a sample of the pumping effect on the jet head velocity, it is seen the velocity can jump around 40% among an impulsive stage which has good agreement with the current results.

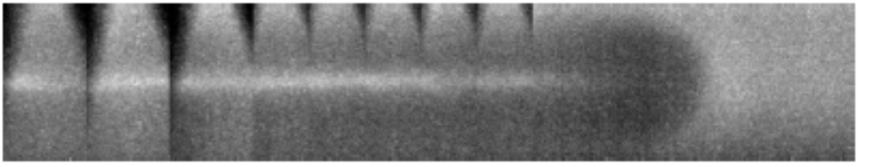

Figure 5.14: light jet (He in Xe), M=10, density ratio= 0.85

It is also important to note that the experimental observation of the head structure is difficult because of the finite, non-negligible exposure time of the camera, necessary for getting enough light. This produces an unavoidable image blur effect since the displacement of the structures under study is not negligible during a typical exposure time.
In the second case Mach number is increased whereas density ratio is kept in the underdense range. Figure 5.15 shows the given jet; by increasing Mach number in the next underdense jet η=0.8, the jet head is sharper and also the size of the cocoon, if compared with the size of the jet core, is smaller than the previous case (jet presented in figure 5.13). The obtained Mach number at the nozzle exit is 13.4. The core gas velocity is estimated 2050 ±200 m/s, and the measured value of the head structure is v_h = (340 ± 70) m/s, so the ratio v_g/v_h is 6.03 which is less than previous jet (M=9.9 and η =0.8).

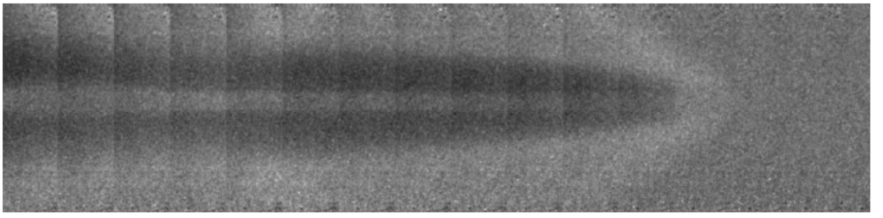

Figure 5.15: light jet, (He in Xe), M=13.4 , η =0.9

The last case in underdense jet generated by the nozzle Mach 20, figure 5.16 shows this jet which has density ratio 0.9 and Mach number at the nozzle exit is 18. Here the jet head gets sharper and also cocoon get thinner in comparison with two last cases. The core gas velocity is estimated 2300 ±300 m/s, and the measured value of the head structure is = (645 ± 130) m/s, so the ratio v_g/v_h is 3.56, it is seen that with increasing Mach number, this ratio decreases; in general it seems that although the jet head velocity is increased with the increase of thejet core velocity, but its velocity ratio, showing flow acceleration, decreases. In other word, the surrounding ambient does not let the flow proceeds proportionally to its initial velocity.

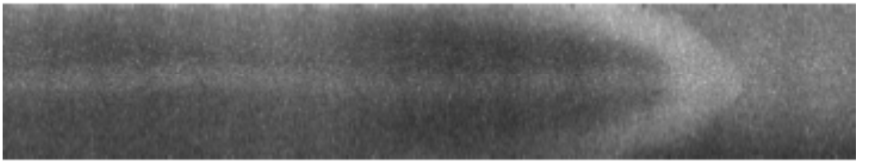

Figure 5.16: light jet, (He in Xe) M=18, density ratio=0.9

By comparison among these three jets it is seen that the lower Mach number leads to a new change in the jet behaviour; the general morphology of the terminal/bow

shock structure in Mach 10 appears similar to the ones at M=15 and 20, but the profile of the bow shock is blunter in Mach 10, as it can be expected for a lower Mach number. Furthermore, the size of the cocoon, if compared with the size of the jet core, is even larger than in higher Mach numbers, again this is an expected effect of the low Mach number.

5.1.1.3. Selected Results Showing General Morphology

In the previous sections the effect of density ratio and Mach number were seen separately, and it was concluded that for the jets with high density ratios, the flow behaviour is almost unchangeable.So the region of interest would be in the green region in the parameter space of figure 5.17.This range of density ratio also captures well the YSO jet, where the jet density is usually close in value to, or not much higher than, the ambient one.

Here the plan is to address the cases of intermediate density ratios for exploring its influence with a combination of Mach number on the jet evolution, therefore for each given Mach numbers (10, 15 and 20), three jets differing in their density ratios; slightly underdense, slightly overdense, and moderate dense, are selected. The analysis of these jets, with regard to the different density ratios and Mach numbers, will give the general morphology of the flow.

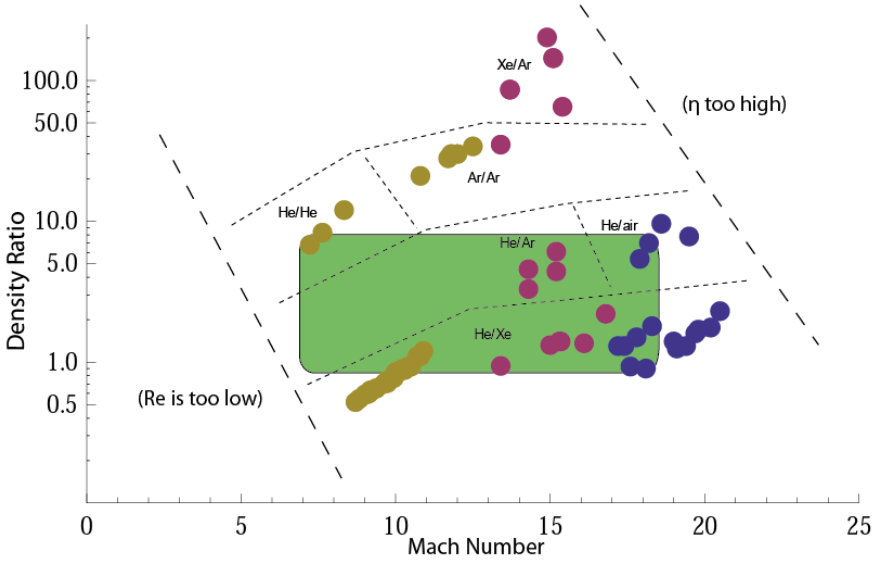

Figure 5.17: The selected region in the parameter space, for exploring the general morphology

The jets are illustrated in figures 5.18 to 5.20 included three sets of the jets. For each set, three different Mach numbers are selected. The resulting image is then compared to the corresponding existing numerical simulation [77].
The Figure 5.19 shows three light, underdense jets, having similar density ratios < 1 and Mach numbers from 10 to 18. Many known properties are visible both in the experiments and in the simulations, namely the presence of a large cocoon, the appearance of compression knots along the jet core and the increasing bluntness of the jet head for decreasing Mach numbers. However, the last property must be considered by keeping in mind that head shape changes continuously with time, owing to the beam pumping phenomenon (see section 5.1.1). In this set of light jets, the blunt shape of the Mach10 jet is considered.
In the laboratory images (figure 5.18) at Mach 10, the bluntest shape of the jet head is taken which has good similarity with the simulated one. At Mach 18, one can see a non-axial symmetric displacement of the jet core, which cannot be reproduced in the related numerical simulation (top panel). This case in explained in detail in the section 5.2.2.4.

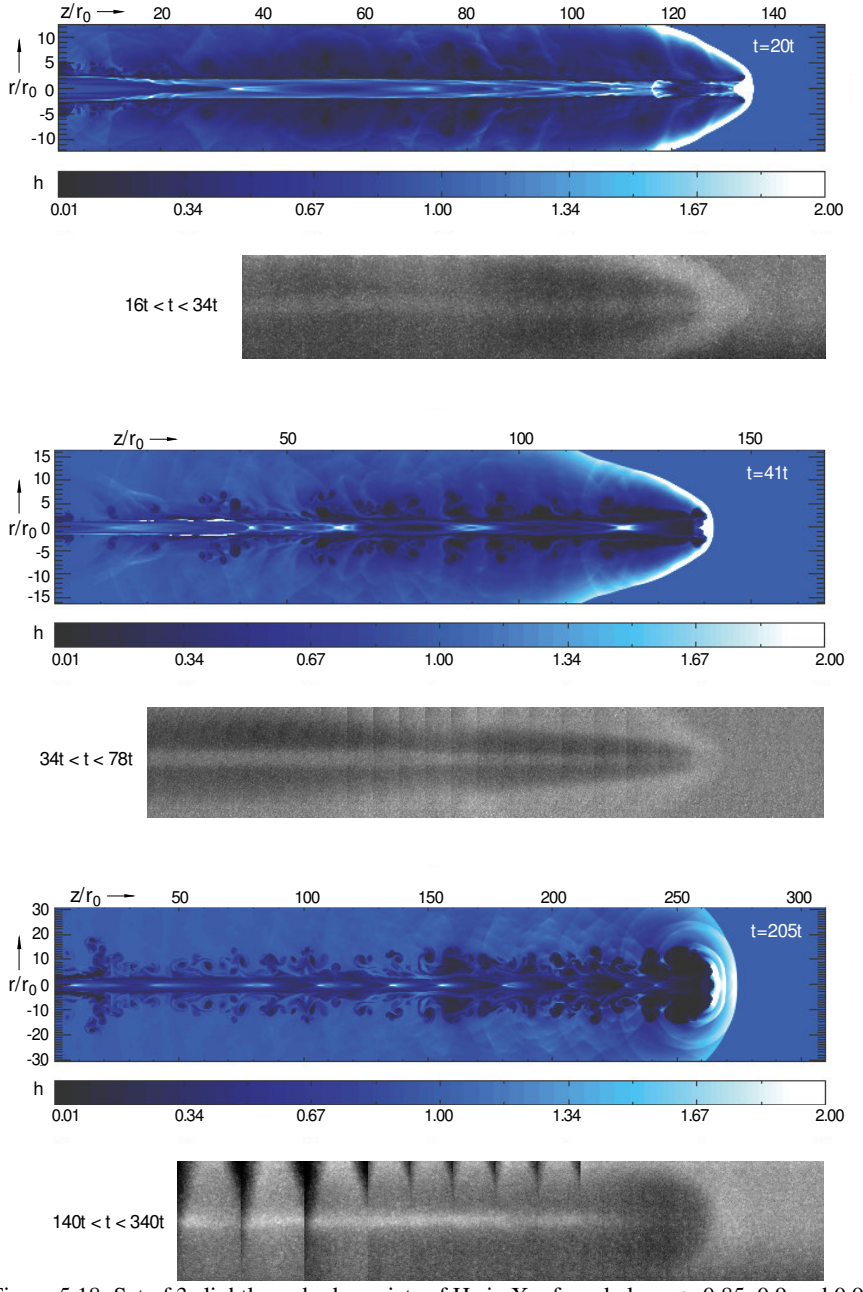

Figure 5.18: Set of 3 slightly underdense jets of He in Xe: from below, η=0.85, 0.9 and 0.9, Mach number = 10.0, 13.5 and 18.0 [77].

A simple quantitative comparison between experiments and simulations can be made by measuring the jet head velocity, the results are shown in Table5.1, and show a good agreement, slightly worsening at the lowest Mach number.

Table 5.1: Head velocities for the jets in figure 5.19

Case	V_{exp}[m/s], ± 20%	V_{num}[m/s], ±7%
Mach 10	155	200
Mach 13.5	340	350
Mach 18	645	750

The Fig. 5.19 shows three slightly overdense jets, having similar density ratios > 1 and Mach numbers from 11 to 18. Again, both in the experiments and in the simulations a cocoon and some compression knots are visible, whereas the jet head is blunter for the lower Mach numbers. With respect to the underdense jets, here the higher density ratio causes a slight decrease of the cocoon and jet head sizes. The comparison between experimental and numerical jet head velocities is shown in Table 5.2, even in this case there is a good agreement, worsening at the highest Mach number.

Table 5.2: Head velocities for the jets in figure 5.20

Case	V_{exp}[m/s], ±20%	V_{num}[m/s], ±7%
Mach 11	355	340
Mach 16	490	500
Mach 18	415	550

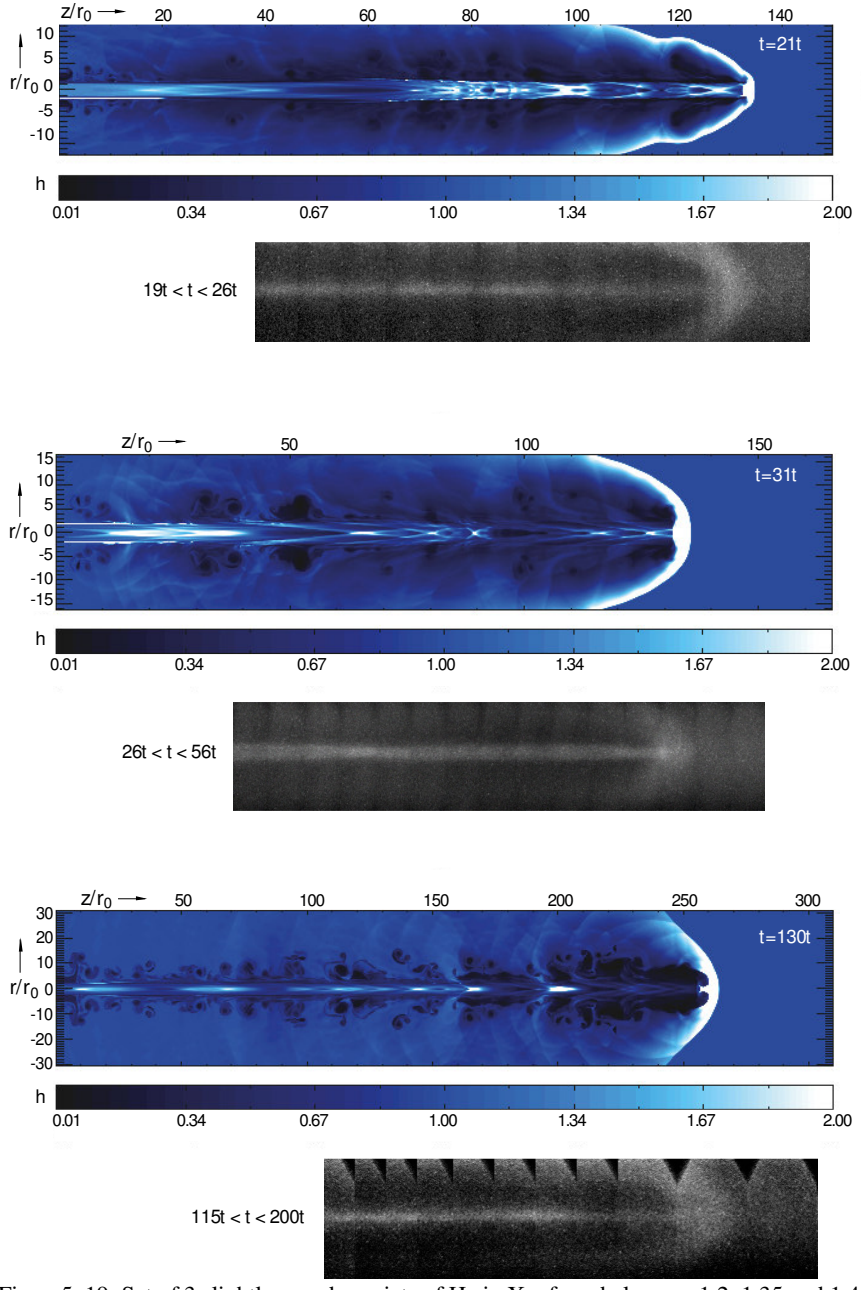

Figure5. 19: Set of 3 slightly overdense jets of He in Xe: from below, η=1.2, 1.35 and 1.4, Mach number = 11.0, 16.0 and 18.0 [77].

The Fig. 5.20 shows three overdense jets, having similar density ratios $\eta \approx 5$ and Mach numbers from 7 to 17.9.

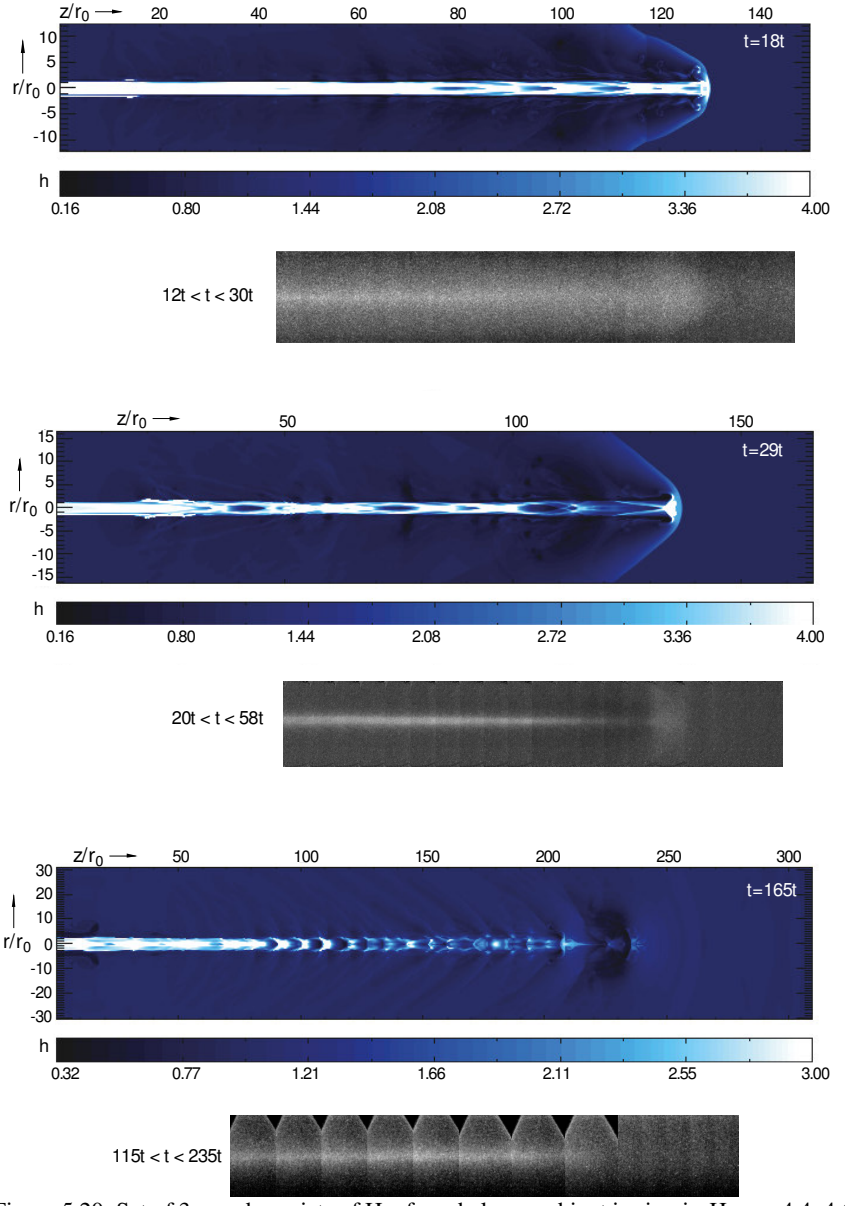

Figure 5.20: Set of 3 overdense jets of He: from below, ambient is air, air, He, η =4.4, 4.6 and 5.4, Mach number = 7.0, 14.3, 17.9 [77].

In this case, as expected, the backward flow zone related to the cocoon formation has a definitely smaller size and the compression zones, when present, are narrowly spaced, so that they cannot be resolved by the experimental technique. The jet head structure is smaller than in the previous cases it must not be confused with the bow shock, which reaches the boundaries of the domain. Unfortunately, at the lowest Mach number presented in this figure, the formation of a proper head structure is hampered by the pressure ratio P_0/P_awhich is, in this particular jet, close to the allowed limit for a nearly matched condition. The comparison between experimental and numerical jet head velocities is shown in Table 5.3, even in this case there is a good agreement.

Table 5.3: Head velocities for the jets in figure 5.21

case	V_{exp}[m/s], ±20%	V_{num}[m/s], ±7%
Mach 14.3	580	600
Mach 17.9	680	700

It is worth noting that pressure matched hypersonic hydrodynamic jets maintain their collimation up to large distances from the launching region, at least within the physical limits of the walls of the chamber.

5.1.1.4. A rare case

The top jet of figure 5.18 which is the jet at Mach 18, a non-axial symmetric displacement of the jet core is visible in experimental results. This jet is shown in figure 5.21 along its evaluation for a longer time (after impact the vessel and), here this sinusoidal movement is more visible. The interesting point is that this behaviour is presented just in thevery high Mach number of underdense jet and also cannot be seen in the corresponding numerical simulation (the below panel of figure 5.21). Actually the top panel of the figure 5.21 is an intentionally frozen reconstruction for the sake of showing some particular features of this jet (do not respect the principles exposed at the beginning of this chapter).

One reason for this non-axially symmetric presented in experimental results, is the nature of three dimensional instability of the flow, whereas the numerical results are simulated by considering a two-dimensional domain [74, 77]. At the moment, we might interpret this observation as an effect of the higher Reynolds number at the nozzle exit that disrupts the symmetry of the mean base flow. In particular, one must consider the effects associated to the viscous and turbulent boundary layer developing along the inner surface of the long de Laval nozzle necessary to

generate the Mach 20 jets; this boundary layer at the nozzle exit is about 65% of the nozzle diameter. This long layer can act as a source of excitation for the long transversal perturbation observed in this image. However, whether this behaviour at high Mach numbers is an effect of the injection mechanism adopted or is the result of the growth of intrinsically non-axially symmetric jet modes remains to be investigated.

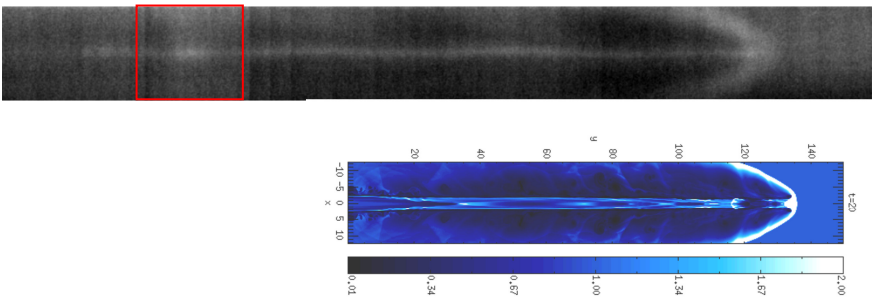

Figure 5.21: the propagation of a slightly underdense jets of He in Xe: η= 0.9, Mach number = 18.0 [77]

One must note that among the jets at Mach 20, just this underdense jet has the self-induced non-axisymmetric long wave instability, and other jets, ones their density is more than ambient one, ($\eta > 1$) do not behave the same.

In figure 5.21, besides the non-axisymmetric long wave instability of the jet, another phenomenon is noticeable; the intense knot which is visible on the jet axis in the rest of the jet (it is marked with a red rectangle in the rest of the jet in figure 5.21). Regarding the counterpart simulation of the free jet (the below panel of figure 5.21), theknot is presented after jet hitting at the end of the vessel, andit would be due to the interaction with the backward flow. Although this bright knot is not related to the free hypersonic jets, it opens another aspect of the interacting jet with the backward flow. The following section explores the rest of the jet which also indicates the effect of back warding flow on the jet.

5.1.2. Jet flow after Impact with the vessel end

In our experiments, the flow is free jet just before impact with the end of the chamber, and after the jet head hits the end of the vessel, it is the interaction of the forward flow with backward reflected one. In the following the morphology of these interactions for two kinds of the jets, light jet (slightly underdense/overdense jet) and heavy jet (highly overdense jest), are explored.

If we come back to the figure 3.8, the nozzle mass flow versus time is illustrated for a sample jet flow. As the piston works and the valve begin to open (t = 0), the outflow increases to a maximum value, then it diminishes as the gas contained in

the reservoir is used up. During the decreasing phase, the mass flow is determined by the natural decay in the amount of gas remaining in the piston chamber [76]. In the following for the light jets (slightly under/over-dense jets), the flowpropagation after impacting is synchronized to the output flow before the decreasing phase, and for the heavy jet is it synchronized to during the decreasing phase.

5.1.2.1. Light jet interaction

Here as the first case, the behaviour of a two light jets, a slightly overdense jet and a slightly underdensejet,after impacting the vessel end is investigated. The jet gas in the both is Helium into Xenon ambient gas, with different Mach number and density ratio; for the first jet $\eta = 1.35 \, and \, M = 16.5$, and for the second one $\eta = 0.9 \, and \, M = 18$. This range of density ratio also captures well the YSO jet, where the jet density is usually close in value to the ambient one.

The first part of the jets, before hitting the vessel, are shown and explained before in the section 5.1.1. This also captures well the YSO jet, where the jet density is usually close in value to the ambient one.

For the first jet, figure 5.21 shows the laboratory visualization of a jet with $\eta = 0.9 \, and \, M = 18$ included the jet after impact; herethe non-axisymmetric long wave instability of the jet is related to the jet before impacting (see section 5.1.1.4). But along the jet after hitting the vessel, a bright knot is presented which is marked with in the figure 5.21. This knot is interpreted due to the matter reflected at the vessel end; when the head jet impact the end of vessel, it reflects backwardly and can compress the rest of jet along its propagation. So the bright knot marked in figure 21, presents in the captured instance where the reflected flow meets the rest of the jet.

To prove this interpretation, second light jet, which is slightly overdense is investigated in more details and also compared with corresponding simulations [76]. Figure 5.22 shows the laboratory visualization of a jet with $\eta = 1.35 \, and \, M = 16.5$. Here also the flow is not free jet, and it is the interaction of backward flow created by hit jet head, and we focus on the part which is interacting with reflected flow. Again along the rest of the jet, an intense knot is presented which is marked in the figure 5.22.

Figure 5.22: Light jet, Helium in Xenon before the rest of the jet after impacting.

This intense knot is visible about ten jet radii from the vessel end and the interesting point is that this knot is also presented in the corresponding simulated jet along its propagation after impact (figure 5.23). Time unit for this light jet is t =0.18 ms.

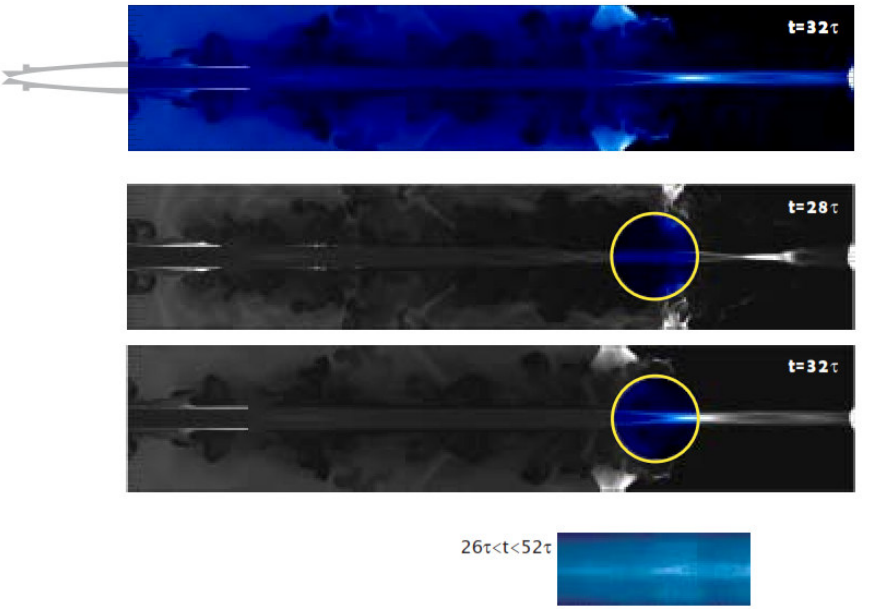

Figure 5.23: Light jet, Helium in Xenon, the same as figure 2.23, Here, the images shown were taken in a time range that came after the instant where the jet head hit the vessel end[76].

As is clear in the simulation, this knot is due to the matter reflected at the vessel end, and the difference in the simulated and experimental positions are for the most part due to measurement errors, but also to the uncertainties in the injection modelling, as our estimation for the output mass flow was used for the input in numerical simulation. So in the both flows of the light jets, the intense knot, due to the reflected flow created by hit jet head, is seen and the numerical results also prove our interpretation.
With a look at the experimental visualization of the jets in figure 5.21 and 5.22, it is realized that the jet is collimated for a time and after destroying by mixed boundary layer. For heavy jets, the rest of jet flow last collimated for much longer time (see the next subsection).

5.1.2.2. Heavy jet interaction

The second case is related to the heavy jets (which are almost ballistic). For two jets the flow is visualized in order to monitor a change in the flow patterns after impacting.

In the first jet, a xenon jet travelling in argon ambientis taken. Figure 5.24 shows the laboratory visualization of this heavy jet with $\eta = 77$ *and* $M = 15.1$. The first panel of this figure is the free jet, and the other panels are for the jet after hitting the jet head which are the interest of this section.The jet structurevisible in figure 5.24 may be interpreted as follows: The images presented here come from a movie made of 150 frames taken at 4300 frames per second; an outline of the movie converted in reconstructed parts of the jet is presented in this figure. Frame 15 to 30, show the free jet flow, i.e. practically not perturbed by the wallseffects. After image 30, the jet head impacts the vessel end, so that a strong backflow is generated andthe flow inside the vessel becomes a jet surrounded by a coaxial stream flowing backward. Under these conditions, the interface between the two flowsbecomes unstable, so that strong waves appear, and are particularly visible in the frames 61 to 90. These instabilities move forward at high velocities; the velocity of instabilities is greater than the head velocity($v_i > v_h$). The next panels ofthe figure 5.24, illustrate the rest of the jet; another interesting point is that here the jet beam is unperturbed for a much longer distance than light jet which means the duration of the heavy jets is longer than light jets.This big difference between light and heavy jetsis due to differentjet mass flowand also different jet velocityof heavy jets from the ones ofthe light jets. Here the backward flow cannot create bright and compressed knot as presented in the light jets. It would be due tocondense and collimated jet beam which the reflected flow cannot considerably affect on it.

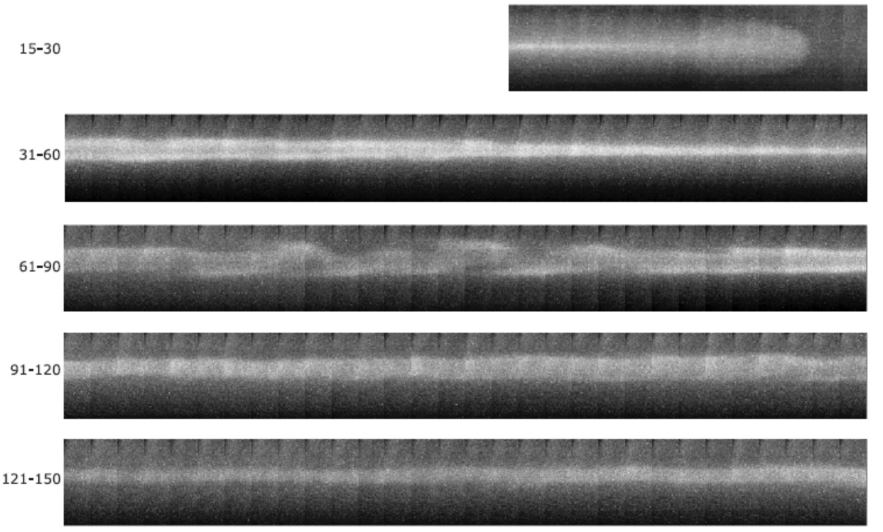

Figure5.24. Sequence of reconstructed images for the heavy jet Xe in Ar at $\eta = 77$ *and* $M = 15.1$; the numbers on the left refer to the frame positions in the movie[78]

The second heavy jet, which is highly overdense is investigated in more details and also compared with corresponding simulations [76] to confirm the morphology. Figure 5.25 shows the laboratory visualization of a xenon jet in air ambient with $\eta = 102$ *and* $M = 13.7$.

The evolution of this heavy jet propagating through the ambient before impact the vessel is illustrated previously in figure 5.12,and figure 5.25 is related to the jet flow after hitting the vessel end, which is compared with the corresponding simulation at several different time instants. This flow propagationshows the jet remains almost unperturbed by the interaction with the external medium. The time unit for this heavy jet is $\tau = 0.96$ ms.

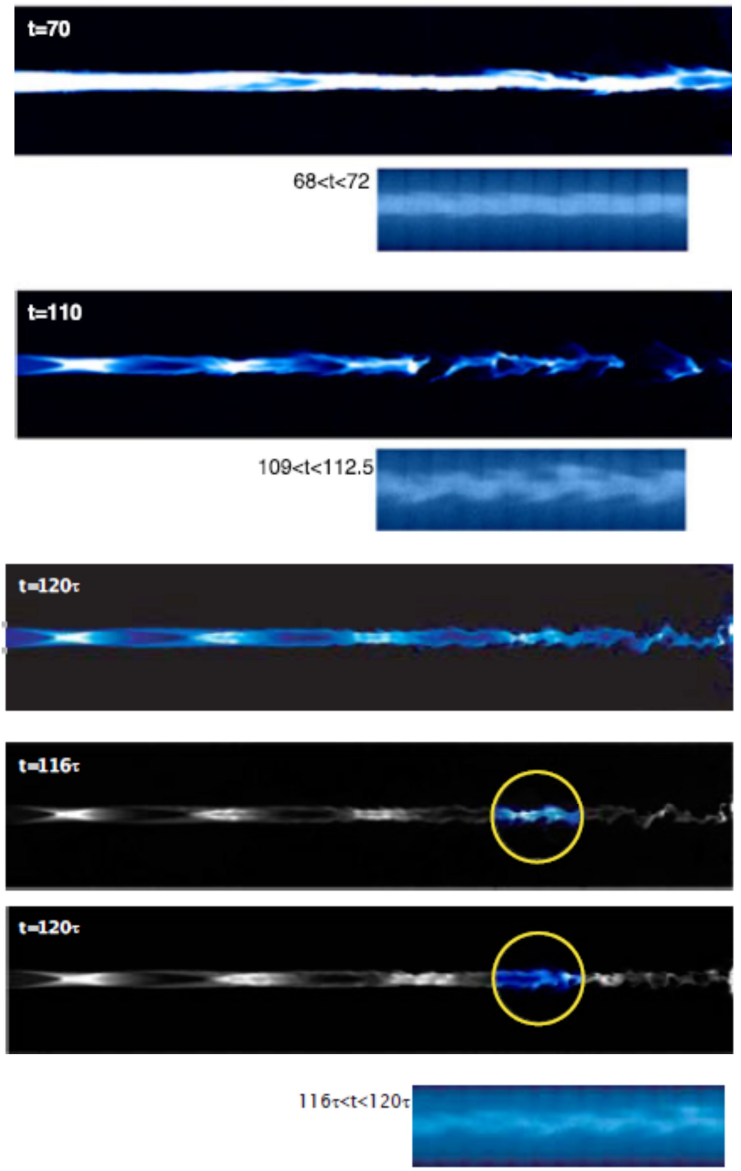

Figure 5.25: Heavy jet, Xenon in Air. Same jet of figure 5.25, the panels have the same meaning but the images are taken in a time range that comes well after the jet head hits the vessel end, during the mass flow decaying phase[76].

The interaction with the reflected flow eventually produces a finite perturbation, which non-linear interacts with the outflow. This is sufficient to spoil the axial-symmetry. However, it is not sufficient to spoil the collimation of the jet. At later stages, when the jet weakens according to the diminishing the jet gas; this interaction causes non-symmetrical oscillations that are visible in both simulated and real jets.
This suggests the possibility of a very large longitudinal extent of the heavy hypersonic jet and its related capability to transfer energy, momentum and mass to large distances (on the Earth, in space, impossible new applications).
In this jet, the flow velocity grows with time and the velocity of instabilities are greater than the head velocity ($v_i > v_h$), which has the same behaviour of the last heavy jet (figure 5.24) and also is in agreement with the numerical simulations [76]. In regard to the current observations for the velocity of instabilities, the Jet evolution can be sketched as in figure 5.26 under the hypothesis that the changes in structure properties are slow with respect to the exposure time;
At time $t = t_0$ the head enters the camera window, and travels through this window in some frames. The jet head is v_h. Then, the head is generally followed by a thin and stable core, becoming progressively more intense,
visible in many frames. At a certain time $t = t_a$ the head reaches the vessel end: in an ideal (infinite) ambient it would simply continue to travel (red sketches in figure), in the real case the head is destroyed and the jet gas begins to raise the ambient density by turbulent mixing, what changes the original jet/ambient density ratio.
This perturbation doesn't seem to give rise to reflected structures, since no reflected waves were observed in the whole experiment set.
Then, at a certain time $t = t_b$ periodic forward-travelling structures begin to enter the camera window,and their velocity v_S can be measured by correlation(see section 4.2.2) , with best accuracy when the wavelength is shortwith respect to camera window size (here v_S is intended as phase velocity of a wave crest and not as groupvelocity). Several kinds of structures were observed, similar to Kelvin-Helmoltz waves at the beginningand to multiple shocks at the end. These structures travel in the forward direction, and are generallyfaster than the head, but slower than the gas: $v_g > v_S > v_h$, so the waves tend to reach the head.

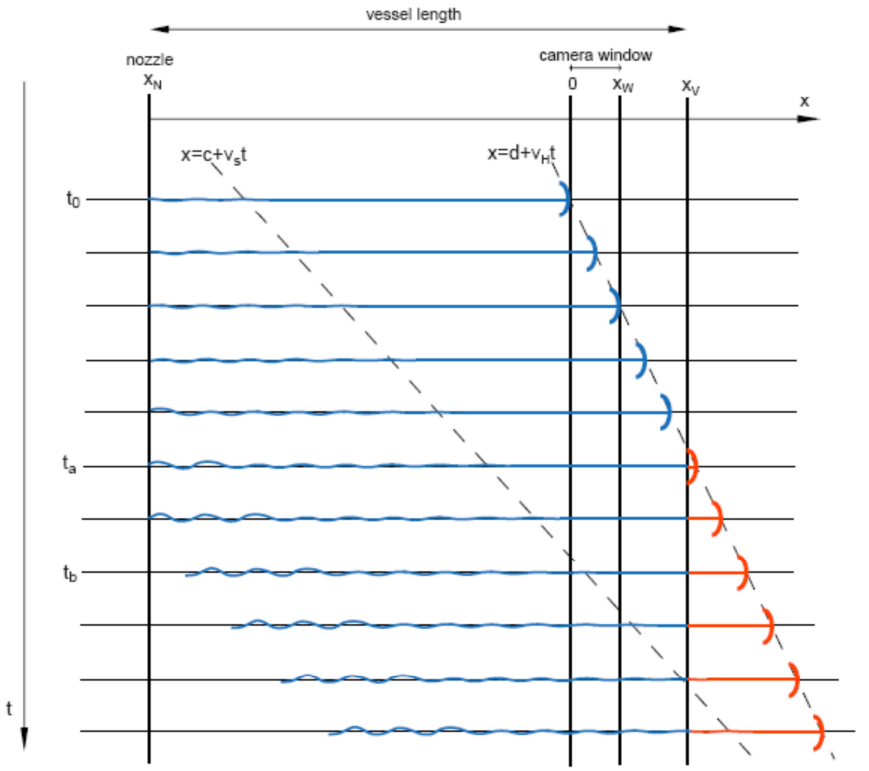

Figure 5.26:Schematic view for the flow velocity at heavy jets.

5.2. Spreading angle measurement

The spreading angle of the jet core is measured by the image processing method applied to the reconstructed images of the jets (see section 4.2.5). The measurement is based on a special criterion, defined according to the derivative curve of the pixel intensity of averages columns behind the jet head; because in the vicinity of the jet core, the derivative is high, the boundary of jet core is conventionally assumed to be bounded by the highest variations of the intensity. Figure 5.27 illustrates a sample of the taken columns behind the jet head. For the measurement in the following results, 200 columns behind the jet head are taken.

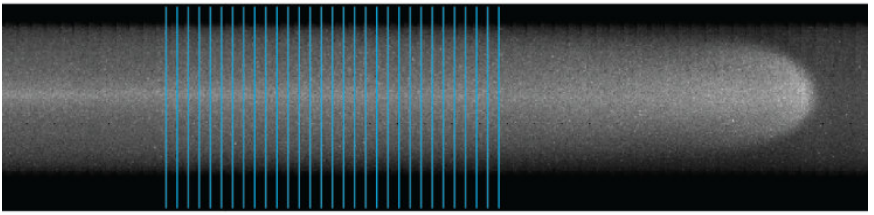

Fig. 5.27: Lateral selected columns of reconstructed image, behind the jet head.

In the section, the jet widths for three different jets are illustrated;
Figure 5.28 is related to an underdense jet at Mach 10.1 and density ratio 0.8; the green curve is the averaged curve of pixel intensity of the columns behind the given jet head, the red curve is the derivative of the counterpart green curve, and the dashed lines show the places of the highest derivatives on both sides of the given jet. The distance between these vertical lines represents the jet core width. Then, the spreading angle can be obtained by comparison with the jet core width at the nozzle exit.

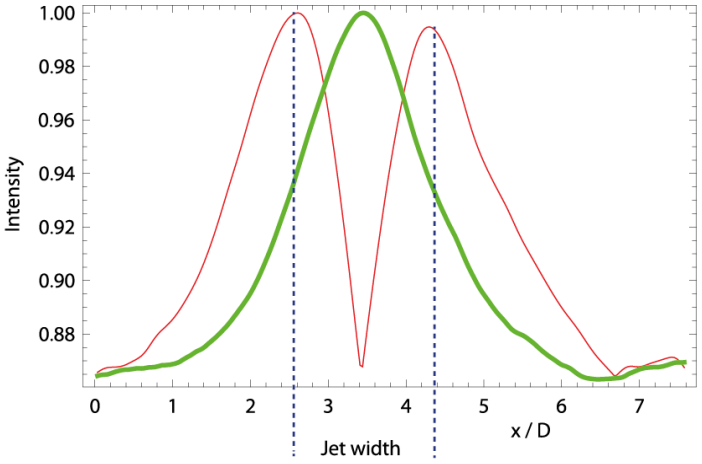

Figure 5.28: Mach 10.9 and density ratio 0.8; green curve: the averaged curve of pixel intensity of the columns behind the jet head, red curve: the derivative of the counterpart green curve, dashed lines: the places of highest derivatives.

Figure 5.28 results that the jet width is about 1.8 times of nozzle diameter. For measuring the spreading angle, the core width at the nozzle exit, as the reference jet width, is needed but it is not possible to measure by the same practical method, however it is obtained from the similar principle applied to the numerical simulation. A proper definition of the reference jet width at the nozzle output can be given by observing that in the present experiment the information is mainly

obtained from density-dependent measurements: for this reason, the jet width will be identified as the bounded diameter by the maximum steepness; where the second derivative along the increasing phase of the density curve is zero.
This definition of the reference jet width is one of the possible definitions among many other options. But if we have to deal with spending angle measures, we must use this definition, because measurements in the far jet like figure 5.28 are luminosity-based, i.e. density-based, so the same definition, generalized by the same criterion, must be applied also for the jet at the nozzle exit. Figure 5.29 shows the jet width boundaries at the nozzle exit, assuming as the points of maximum steepness, which are obtained numerically [77].

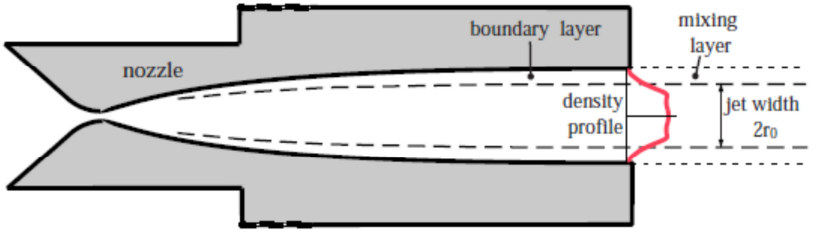

Figure 5.29: The jet width boundaries at the nozzle 10 exit [77]

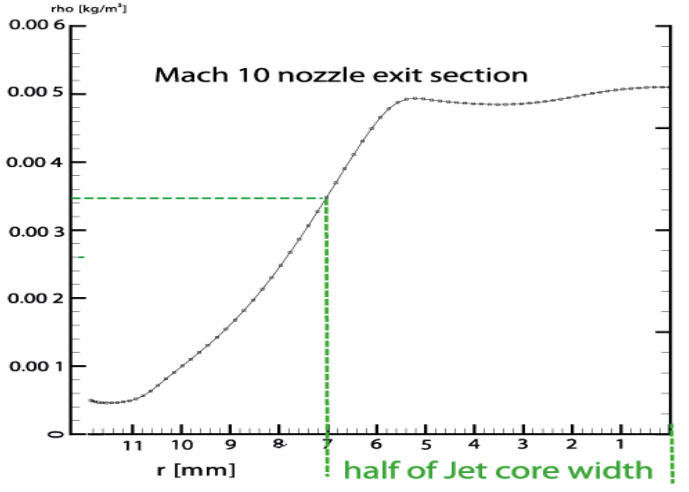

Figure 5.30: Simulated density profile at the exit of Mach 10;dashed line reports the thepoint of maximum steepness or zero 2nd derivative

Figure 5.30 shows simulated density profile at the exit of Mach 10, and as obvious the jet width is about 15.6 cm (twice of the core radius) which is 58% of the

nozzle diameter. By comparison the jet width at the nozzle exit (0.58 D) and jet width in the far field captured in front of electron sheet (1.8 D), and also the distance between them (31.3 D), the spreading angle is obtained which for this case it is about 2.23 degrees.

The second case is an overdense jet, $\eta = 4.4$ at Mach number 7, shown in figure 5.31. Here the jet width is about 1.6 times of the nozzle diameter, leading to have 1.86 degrees for spreading angle which is slightly less than one in previous jet (shown in figure 5.28). This comparison shows the effect of density ratio, slightly underdense and overdense, on the spreading angle, and as is expected increasing the density ratio leads to have more collimated jet and consequently smaller spreading angle.

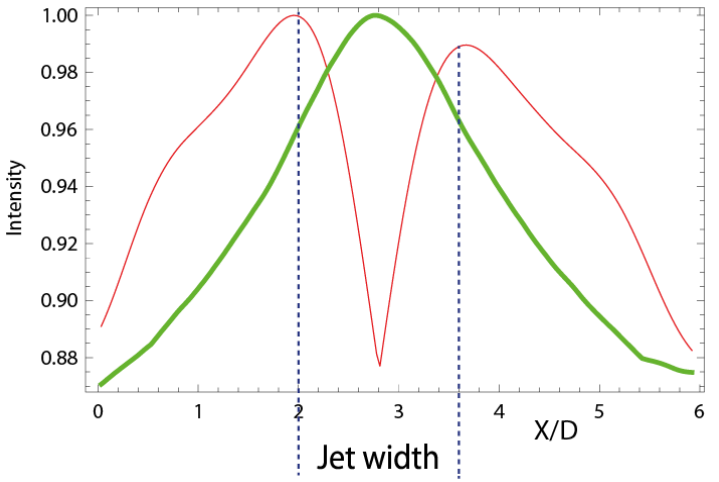

Figure5.31:η=4.4 at Mach number 7, green curve: the averaged curve of pixel intensity of the columns behind the jet head, red curve: the derivative of the counterpart green curve, dashed lines: the places of highest derivatives.

In order to know the effect of Mach number on spreading angle, a jet with density ratio ($\eta = 1.4$) at Mach number 18.9, illustrated in figure 5.32, is compared with the previous jets, being at Mach 10 range. In this jet, core width is about 0.32 times of the nozzle diameter, but for this given nozzle, Mach 20, the jet core at the nozzle exit is about 36% of its diameter, which means jets at high Mach numbers do not expand and their spreading angle is nearly zero. In other word, in the higher Mach numbers, the jet flow is much more collimated than lower Mach numbers.

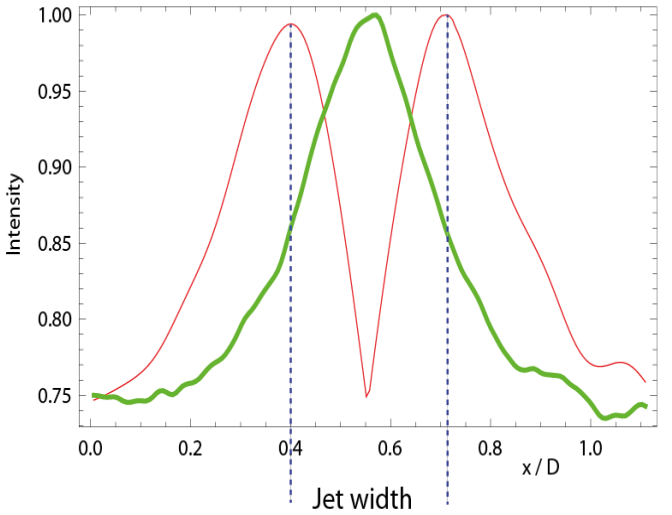

Figure 5.32: density ratio=1.4, Mach number = 18.9, green curve: the averaged curve of pixel intensity of the columns behind the jet head, red curve: the derivative of the counterpart green curve, dashed lines: the places of highest derivatives.

5.3. Density measurements

Another kind of quantitative result is about density measurement, using the proportionality law $I = k\,\rho$ between the light intensity due to fluorescent emission and the density (see section 4.2.6).

Whenever possible, the results are obtained by using different values of the constant **k** for different gas species. Here density values are measured along the axes of three jets, it should be noticed that the inner zone of the jet heads, namely the region between the bow shock and the terminal shock, cannot be analyzed because it contains two mixed gas species (see figure 2.1).

The output density values are corrected accounting for the image background noise and the final curves are compared with the relevant numerical ones. Figure 5.33, 5.34 and 5.35 show experimental and numerical results of the axial density for the three slightly overdense jets. Densities are expressed in non dimensional form as density ratios η referred to the unperturbed ambient.

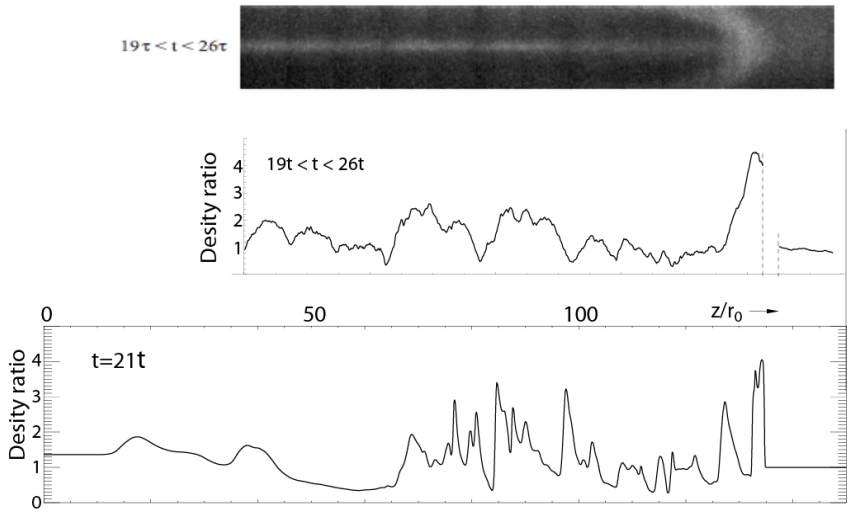

Figure 5.33: Experimental (upper panel) and Numerical (lower panel) axial density for a slightly overdensejets;M=18 and density ratio 1.4, Densities are expressed in non dimensional form as density ratios η referred to the unperturbed ambient[77].

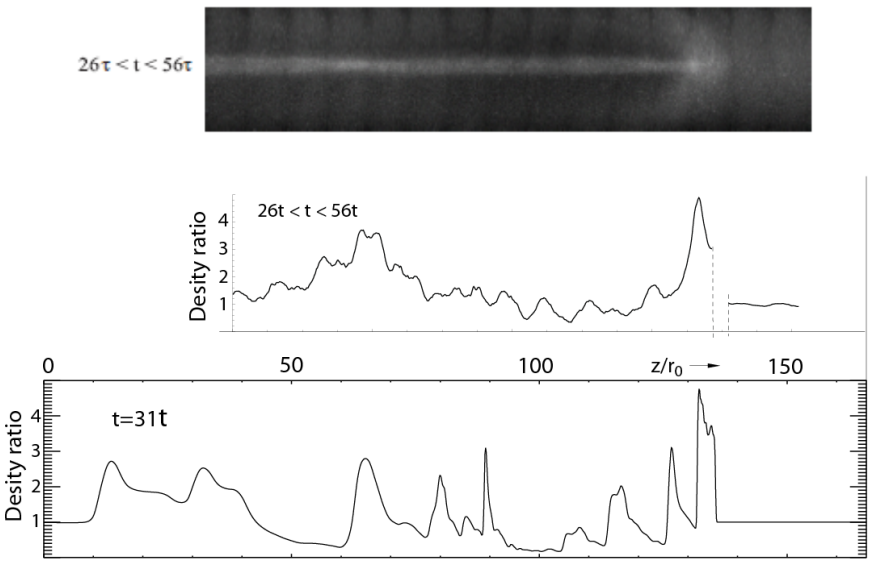

Figure 5.34: Experimental (upper panel) and Numerical (lower panel) axial density for a slightly overdense jets. M=16 and density ratio 1.35, Densities are expressed in non dimensional form as density ratios η referred to the unperturbed ambient[77].

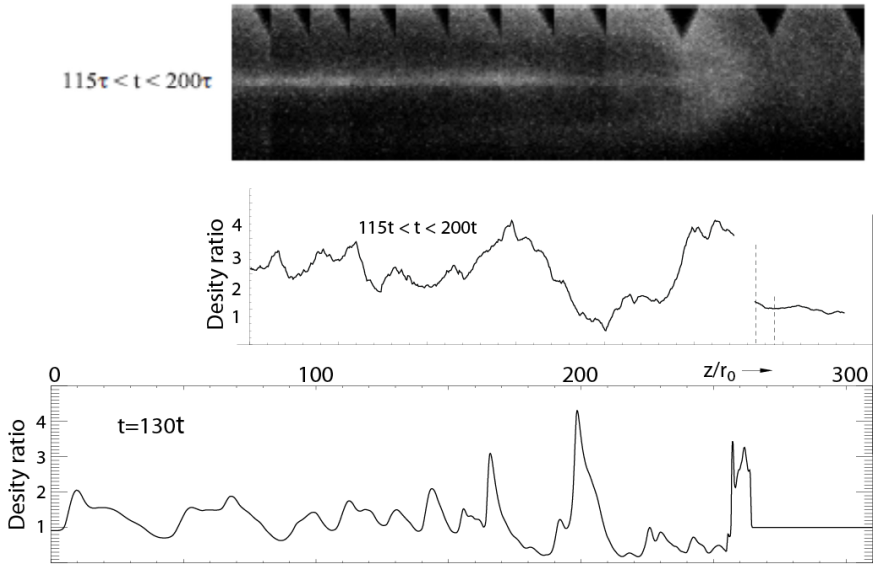

Figure 5.35: Experimental (upper panel) and Numerical (lower panel) axial density for a slightly overdense jets, M=11 and density ratio 1.2, Densities are expressed in non dimensional form as density ratios η referred to the unperturbed ambient [77].

The results, given in terms of the density ratio η referred to the unperturbedambient, show that the experimental technique is capable to reproduce the large scale density variations, whereas the small scale details are lost. However, it must be recalled that the small scale structures exhibit turbulent temporal variations scarcely reproducible. That is, even at higher time resolution of the camera producing less blur in the experimental images would probably reveal different small scale variations at each repetition of the same jet.

Conclusions

About experiment;The experimental facility and instrumentation has shown to fit the experimental requirements and to give valid results for the aim it was designed and assembled. The whole facility is reliable in the different configurations and usable in a wide range of Mach Numbers and density ratio, helping us to reach our goal; investigation of hypersonic jets in different conditions. The uses of matched or quasi-matched de Laval nozzles allow to have rather well known boundary conditions of the jets. The calibration procedures developed for the different Mach Numbers are also reliable. The distance of observation, as referred to the initial jet diameter, is far larger than any of the available experiment and is in the range of stellar jets, while it is not the only purpose of these facilities. Although real stellar jets are not generated in this way, the development of the jets and their observable structures and instabilities in the form of ”knots” are not related to boundary conditions but are part of the jet development itself.

About the imaging; several image processing techniques have been applied to the study of the jets morphology. Wide images of the jets were reconstructed by partial juxtaposition of denoised frames. Also an accurate technique to measure velocity of flow structures was introduced, based on modifications of standard correlation techniques. The spreading angle was measured by an inventive technique, and for the density measurement, the method based on the proportionality between the light intensity due to the fluorescent emission and the density, was used.

About the results, it has been shown that many of the facets of the stellar jets may be simulated in a pure fluid dynamic experiment, without the need of electromagnetic fields, what is an important issued in astrophysics; some facets of the jets are included the detailed aspects of the head bow shock, its bluntness and the shape of the cocoon as a function of the density ratio and Mach number. Both overdense and underdense jets have been visualized in a wide range of density ratios and this has allowed to have an insight on the change both in the jet and cocoon structures, and also in the instabilities that appear on streams interfaces. In this sense the use of gases of strong density difference, as Helium and Xenon has been of focal importance.

This methodology allows giving some insight on the behaviour of the free hypersonic jet flows and can also be usedas an important validation of the numerical tools.

Also the jet behaviour, after impact the vessel end, has been explored; the fact that the jet structure, after impacting, is still persistent, although is not part of the stellar jets effort of simulations, is interesting as it is a new piece of knowledge. In some cases, the visualized jets have been compared with the existing numerical simulations which are in good agreement in most cases. In General our experimental results highlight the following aspects:

I) The collimation of near-isoentropic jets over distances much larger that the initial radius.
II) The jet persistence (which, for the heavy jet, is maintained lengthy even after the impact with the vessel end-wall).
III) The presence of a cocoon surrounding the underdense jet, while this is not visible for the overdense one.
IV) Variation of the spreading angle with changing the density ratio and Mach number (increasing the density ratio or Mach number, leads to have more collimated jet and accordingly decrease in the spreading angle).
These aspects refer to experiments ruled by Newtonian dynamics, and do not need of the confining effect associated with the presence of magnetic fields. Some of these aspects are common to stellar jets, in particular the jet confinement and persistence over long distances, in units of the initial radius.

For future;

Although the quality of the images is not so good as desirable, due to the camera limits and also as a consequence of the intrinsic limits of the electron beam technique, they may be elaborated to get enough data, while the use of a camera with higher performances is the most urgent further development of the experimental setup.
Another progress in the facility could be moving the nozzle inside the vessel, closer to the electron sheet, to investigate the jet morphology for the lower range of Mach number, having less Reynolds numbers.
To explore the jet morphology in the thermal aspect, the facility would be developed to further heat the gas jet, while it will probably require major modifications to the full system and in any case a rather high cost.

Reference

[1] S. M. Prudhomme, H. Haj-Hariri, Investigation of supersonic underexpanded jets using adaptive unstructured finite elements,Journal Finite Elements in Analysis and Design , Volume 17 Issue 1, pp. 21 – 40, 1994.

[2] K.G. Klavuhn, G. Gauba and J.C. McDaniel, "High-resolution oh lif velocity measurement technique for high-speed reacting flows", AIAA Paper 92-3422, 1992.

[3] Birkinshaw M, E M Gouveia Dal Pino, A L Peratt, G A Medina Tancro and A C L Chian, Instabilities in astrophysics jets Advanced Topics on Astrophysical and Space Plasmas ed (Dordrecht: Kluwer) 17,1997.

[4] Ferrari A, Modelingextragalactic jets, Annual Review of Astronomy and Astrophysics,Vol. 36,pp 539-598 , September 1998.

[5]P. A. Rosen, B. H. Wilde, R. J. R. Williams, J. M. Foster, P. A. Keiter, R. F. Coker, T. S. Perry, M. J. Taylor, R. P. Drake, G. R. Bennett, D. B. Sinars and R. B. Campell, 'Recent experimental results and modeling of high-mach-number jets and the transition to turbulence', Astrophysics and Space Science, 298, 121, 2005.

[6] Gouveia Dal Pino E M, Astrophysical jets and outflows. deGouveia Dal Pino, Elisabete M. Advances in Space Research vol. 35 issue 5. pp. 908-924, 2005.

[7] Hester, J.J., Stapelfeldt, K.R., Scowen, P.A.: Hubble space telescope wide field planetary camera 2 observations of HH 1–2. Astron. J. 116, 372–395, 1998.

[8] Reipurth B and Bally J, Herbig-Haro Flows: Probes of Early Stellar Evolution, Ann. Rev.Astron. &Astrophys., 39, 403–455,2001.

[9] de Gouveia Dal Pino, E.M., 3-D Simulations of cosmic jets employing the smoothed particle hydrodynamics technique.Proceedings da, IV International Toki Conference Plasma Physics and Controlled Fusion, pp. 333-336, 1995.

[10] Reipurth, B., Herbig-Haro objects and their energy sources (publ. Danish Natural Science Research Council, 1999.

[11] de Gouveia Dal Pino, E.M, and Cerqueira, A.H.,The effects of magnetic fields on radiative cooling jets in Emission Lines from Jet Flows (eds. W. Henney, W. Steffen,L. Binette, A. Raga), RMAA, Conf. Ser. 13, 29, 2002.

[12] Raga, A.C, Velazquez, P.F., de Gouveia Dal Pino, E.M., Noriega-Crespo, A., and Mininni, P., ,Entrainment in Herbig-Haro objects Rev. Mex. AA conf. Series (eds. S.J. Arthur & W.J. Henney), 15, 115, 2003.

[13] de Gouveia Dal Pino, E.M. et al., in Open Issues in Local Star Formation (eds. J. Lepine and J. Gregorio- Hetem), 303, 2003.

[14] Cerqueira, A. H., and de Gouveia Dal Pino, E.M., MHD numerical simulations of proto-stellar jets Space Science Reviews 107 (1-2) , pp. 337-340, 2003

[15] Eds. E. M. de Gouveia Dal Pino, A. Lazarian& G. Lugones,Shibata, K. MHD flares and jets in the sun, stars, and accretion disks. In: de Gouveia Dal Pino, E.M., Magnetic Fields and Dispersion of Polarization Angles: IRAS Vela Shell, Pereyra, A. &Magalhães, A. M., in American Institute of Physics (AIP) Conference Proceedings, Magnetic Fields in the Universe: from Laboratory and Stars to Primordial Structures, Vol. 784, pp. 743, 2005.

[16] Pringle, J.E..in: Burgarella, D., Livio, M., O Dea, C. (Eds.), Astrophysical Jets. Cambridge University, Cambridge, MA, p. 1, 1993.

[17] Livio, M. Jets: some recent developments. In: Howell, S. et al. (Ed.), Wild Stars in the old West, ASP conf. Ser., pp. 137, 264–272, 1998. Livio, M. The Jet set. Nature 417, 125, 2002.

[18] Livio, M., Pringle, J.E. The Formation of Point-symmetric Nebulae. Astrophysical Journal Letters 465 (1 PART II) , pp. L55-L56, 1996.

[19] Mirabel, I.F., Rodriguez, L.F. Sources of relativistic jets in the galaxy.Annual Review of Astronomy and Astrophysics 37 (1) , pp. 409-443, 1999.

[20] Mirabel, I.F., Rodrigues, L. Formation of a black hole in the dark. Science 300 (5622) , pp. 1119-1120, 2003.

[21] Massaglia, S. Constraining the parameters of AGN jets. Astrophys.Spa.Sci. 287, 223–233, 2003.

[22] Codella, C., Cabrit, S., Gueth, F., Cesaroni, R., Bacciotti, F., Lefloch, B.,McCaughrean, M.J.: A highly-collimated SiO jet in the HH212 protostellar outflow. Astronomy and Astrophysics ; 462 ; L53, 2007.

[23] Reipurth, B., Heathcote, S., Morse, J., Hartigan, P., & Bally, J., Hubble Space Telescope Images of the HH~34~Jet and Bow Shock: Structure and Proper Motions, AJ 123, 362.2002.

[24] Khokhlov, A. and Höflich, P. in: H.-Y., Chang, C.-H. Lee and M. Rho (eds.), Explosive Phenomena in Astrophysical Compact Objects, AIP Conference Proceedings No. 556, New York: AIP, p. 301, 2001.

[25] Sikora, Marek; Begelman, Mitchell C.; Rees, Martin J. ,Comptonization of diffuse ambient radiation by a relativistic jet: The source of gamma rays from blazars Astrophysical Journal, Part 1 (ISSN 0004-637X), vol. 421, no. 1, pp. 153-162, 1994.

[26] Giannios D and Spruit H C, The role of kink instability in Poynting-flux dominated jets, Astrophysical processes. 450 887, 2006.

[27] Khokhlov, A.M., Hoflich, P.A., Oran, E.S., Wheeler, J.C.,Wang, L. and Chtchelkanova, A.Yu.Jet-induced Explosions of Core Collapse Supernovae,,The Astrophysical Journal Letters,V524, 107, 1999.

[28] Hester, J.J., Stapelfeldt, K.R., Scowen, J.A.: Hubble space telescope wide field planetary camera 2 observations of HH 1-2. Astrophys. J. 116, 372–395, 1998.

[29] Ha, Y., Gardner, C.L., Gelb, A., Shu, C.-W.: Numerical simulation of high Mach number astrophysical jets with radiative cooling. J. Sci. Comput. 24, 29–44, 2005.

[30] Gardner, C.L., Ha, Y., Hester, J.J., Krist, J.E., Shu, C.-W., Stapelfeldt, K.R.: Numerical simulation of high Mach number astrophysical jets. In: Analysis, Modeling and Computation of Hyperbolic PDE and Multiphase Flow. SUNY, Stony Brook, 2005.

[31] Youngsoo Ha. ,Positive Scheme Numerical Simulation of High Mach Number Astrophysical Jets, Journal of Scientific Computing, 03, 2008.

[32] Matel I. Radulescu, The transient start of supersonic jets, Journal of Fluid Mechanics, Volume 578,pp 331-369, 2007.

[33] Love, E. S. , et al., Experimental and Theoretical Studies of Axisymmetric Free Jets, NASA TR R-6, 1959.

[34] Ashkenas and Sherman, Rarefied Gas Dynamics, Academic, New York, Vol. 2, p. 84, 1966.

[35] Tesileanu, A. Mignone, S. Massaglia and F. Bacciotti, Numerical Simulations of Radiative Magnetized Herbig–Haro Jets: The Influence of Pre-ionization from X-Rays on Emission Lines, The Astrophysical Journal, 746, 2012.

[36] Belan M., De Ponte S., Tordella D., Massaglia S., Ferrari A., Mignone A., Bodenschatz E, Hydrodynamics of hypersonic jets: experiments and numerical simulations, Astrophysics and Space Science, 336, 2011.

[37] A. Mignone, P. Rossi, G. Bodo, A. Ferrari, S. Massaglia, High-resolution 3D relativistic MHD simulation of jets, Monthly Notices or the Royal Astronomical Society, 402, 2010.

[38] Ampleford D. J. et al., Laboratory modeling of standing shokes and radiatively cooled jets with angular momentum, Astrophys Space Sci 307, 51-56. 2007.

[39]J. M. Soures, R. L. McCrory, C. P. Verdon, A. Babushkin, R. E. Bahr, T. R. Boehly, R. Boni, D. K. Bradley, D. L. Brown, R. S. Craxton, J. A. Delettrez, W. R. Donaldson, R. Epstein, P. A. Jaanimagi, S. D. Jacobs, K. Kearney, R. L. Keck, J. H. Kelly, T. J. Kessler, R. L. Kremens, J. P. Knauer, S. A. Kumpan, S. A. Letzring, D. J. Lonobile, S. J. Loucks, L. D. Lund, F. J. Marshall, P. W. McKenty, D. D. Meyerhofer, S. F. B. Morse, A. Okishev, S. Papernov, G. Pien, W. Seka, R. Short, M. J. Shoup, M. Skeldon, S. Skupsky, A. W. Schmid, D. J. Smith, S. Swales, M. Wittman, and B. Yaakobi, Direct-drive laser-fusion experiments with the OMEGA, 60-beam, >40 kJ, ultraviolet laser system, Phys. Plasmas 3, 2108, 1996.

[40] Foster, J.M. Wilde, B.H., Rosen, P.A., Perry, T.S., Fell, M., Edwards, M.J., Lasinski, B.F., Turner,R.E. and Gittings, M.L.Supersonic jet and shock interactions, Phys. Plasmas 9, 2251. 2002.

[41] Kauffman RL, Suter LJ, Darrow CB, Kilkenny JD, Kornblum HN, Montgomery DS, Phillion DW, Rosen MD, Theissen AR, Wallace RJ, Ze F., High temperatures in inertial confinement fusion radiation cavities heated with 0.35 microm light., Phys. Rev. Lett., 73, 2320, 1994.

[42] Lindl, J.Development of the indirect-drive approach to inertial confinement fusion and the target physics basis for ignition and gain, Phys. Plasmas, 2, 3933, 1995.

[43] Sinars, D.B., Cuneo, M.E. Bennett, G.R.,Wenger, Cuneo, M.E. and Porter, J.L.Evaluation of Bent-Crystal X-Ray Backlighting and Microscopy Techniques for the Sandia Z Machine,:Applied Optics, Vol. 42, Issue 19, pp. 4059-4071, 2003.

[44] D. J. Ampleford, S. V. Lebedev, A. Ciardi, S. N. Bland, S. C. Bott, G. N. Hall, N. Naz, C. A. Jennings, M. Sherlock, J. P. Chittenden, A. Frank, E. Blackman,

Laboratory Modeling of Standing Shocks and Radiatively Cooled Jets with Angular Momentum.Astrophys Space Sci, 307, pp. 51–56, 2007.

[45] S. V. Lebedev1, J. P. Chittenden, F. N. Beg, S. N. Bland1, A. Ciardi1, D. Ampleford, S. Hughes, M. G. Haines, A. Frank, E. G. Blackman, and T. Gardiner, Laboratory Astrophysics and Collimated Stellar Outflows: The Production of Radiatively Cooled Hypersonic Plasma Jets, S. V. Lebedev et al. ApJ 564 113, 2002.

[46] Ciardi, A., Lebedev, S.V., Chittenden, J.P., Bland, S.N., Modeling of supersonic jet formation in conical wire array Z-pinches, Laser and Particle Beams, vol.20, no.2, pp. 255-261,2002.

[47] Belan M., De Ponte S., Massaglia S., Tordella D., Experiments and numerical simulations on the mid-term evolution of hypersonic jets. Astrophys Space Sci 293 (1-2):pp. 225-232 , 2004.

[48] Belan M., De Ponte S., Tordella D., Determination of density and concentration from fluorescent images of a gas flow, Exp in Fluids , vol.45 n3, 2008.

[49] B. Andr´e, T. Castelain1, and C. Bailly, Experimental exploration of an underexpanded supersonic jet, Published in 28th International Symposium on Shock Waves,pp. 629, Nantes, France, 2012.

[50] D. Mitchell, D Honnery and J. Soria, Study of Underexpanded Supersonic Jets with Optical Techniques, 16th Australasian Fluid Mechanics Conference,Crown Plaza, Gold Coast, Australia 2-7 December 2007.

[51] M.L. Norman, K.-H. A. Winkler, Supersonic Jets, Los Alamos Science, Spring/Summer 1985.

[52] M. V. Otugen, D.Bivolaru, E. Arik, K. Jensen, PIV Study of a Mach 1.6 Supersonic Jet, Proceedings of VSJ-SPIE98, Yokohama, Japan December, 1998.

[53] Tsuyoshi Yasunobu, Ken Matsuoka, Hideo Kashimura, Shigeru Matsuo, Toshiaki Setoguchi, Numerical Study for Hysteresis Phenomena of Shock Wave Reflection in Overexpanded Axisymmetric Supersonic Jet, J. of Thermal Science Vol.15, No.3.2007.

[54] A. Dauptain, B. Cuenot and L.Y.M. Gicquel, "Large Eddy Simulation of a Stable Supersonic Jet Impinging on a Flat Plate," AIAA Journal, 48(10), pp. 2325-2338, 2010.

[55]D. d'ambrosio, D.M. de Socio and G. Gaffuri, Physical and Numerical Experiments on an Under-Expanded Jet,Journal of Meccanica, Volume 34, Issue 4, pp 267-280, 1999.

[56] R. D. Blandford and M, J. Rees., A 'Twin-Exhaust' Model for Double Radio Sources, Monthly Notices of the Royal Astronomical Society 169, pp. 395-415, 1974.

[57] Belan M., Tordella D., De Ponte S., A system of fast acceleration of a mass of gas for the laboratory simulation of stellar jets. Proceedings of the ICIASF meeting , Cleveland, pp. 409-416, 2001.

[58] Belan M., De Ponte S., D'Ambrosio D., Tordella D., Design of an experiment on the spatial evolution of hypersonic jets. Atti XVI ConferenzaAIDAA , Palermo, 2001.

[59] M.Belan, Instruction Manual for the experimental system of hypersonic jets, Aerodynamic laboratory, aerospace department of politecnico di milano, 2012.

[60] A. Rosen, P.A. Hughes, G. Comer Duncan, P.E. Hardee, in: A comparison of the morphology and stability of relativistic and nonrelativistic jets, Astrophysical Journal, 516, 1999.

[61] R. Presura, S. Neff, L. Wanex, in: Experimental Design for the Laboratory Simulation of Magnetized Astrophysical Jets, Astrophys Space Sci, 307, 2007.

[62] C. D. Gregory, J. Howe, B. Loupias, S. Myers, M.M. Notley, Y. Sakawa, A. Oya, R. Kodama, M. Koenig and N. C. Woolsey N C, in: Astrophysical Jet Experiments with Colliding Laser-produced Plasmas, ApJ 676 420, 2008.

[63] D. J. Ampleford, S. V. Lebedev, A. Ciardi, S. N. Bland, S. C. Bott, G. N. Hall, N. Naz, C. A. Jennings, M. Sherlock, J. P. Chittenden, A. Frank, E. Blackman, in: Laboratory Modeling of Standing Shocks and Radiatively Cooled Jets with Angular Momentum, Astrophys Space Sci 307, 2007.

[64] P. Hartigan, J. M. Foster, B. H. Wilde, B. F. Coker, P. A. Rosen, J. F. Hansen, B. E. Blue, R. J. R. Williams, R. Carver and A. Frank, in: Laboratory Experiments, Numerical Simulations, and Astronomical Observations of Deflected Supersonic Jets: Application to HH110, ApJ 705,1073, 2009.

[65] Tropea, Cameron; Yarin, Alexander L.,Chapter 25 of the Springer Handbook of Experimental Fluid Mechanics, Volume package: Springer Handbooks; Foss, John F. (Eds.), 2007.

2007, XXVIII, 1557 p. 1240 illus. [66] H. Noori , SaeidSaryazdi , Image Inpainting Using Directional Median Filters, International Conference on Computational Intelligence and Communication Networks,2010.

[67] M. Bertalmio, G. Sapiro, V. Caselles, and C. Ballester, Image inpainting, Proceeding of SIGGRAPH, computer graphics processing. pp. 417-424, 2000.

[68] M. Bertalmio, A. Bertozzi, and G. Sapiro, Navier-stokes, fluid dynamics and image and video inpainting, presented at the IEEE CVPR, 2001.

[69] Y. Chen, Q. Luan, H. Li, O. Au,Sketch-guided texture-based image inpainting, IEEE trans. pp. 4244-048, 2006.

[70] M. Oliveira, B. Bowen, R. Mckenna, Y. S. Chang, Fast digital image inpainting, in proc. VIIP2001, pp. 261-266, [PUB], 2001.

[71] X. C. Tai, S. Osher, R. Holm, Image inpainting using a TV-Stokes equation, IEEE Trans. Image Process. 2005.

[72] Belan M., De Ponte S., Tordella D., Simultaneous density and concentration measurements on hypersonic jets. Abstract, EFMC6 KTH, Euromech Fluid Mechanics Conference 6 , Royal Institute of technology, Stockholm, 2006.

[73] Mignone, A., Bodo, G., Massaglia, S. et al. A. ,PLUTO: A Numerical Code for Computational Astrophysics,The Astrophysical Journal Supplement Series Volume 170 Number 1, 170, 228, 2007.

[74] http://plutocode.ph.unito.it/index.html

[75] Massaglia S, Bodo G and Ferrari, Dynamical and radiative properties of astrophysical supersonic jets. I: Cocoon morphologies Astron. Astrophys. 307 997–1008. 1996.

[76] Tordella D., Belan M., Massaglia S., De Ponte S., Mignone A., Bodenschatz E., Ferrari A., Astrophysical jets: insight into long term hydrodynamics, New J of Physics 13, 043011, 2011.

[77] M. Belan, S. Massaglia, D. Tordella, M. Mirzaei, S. de Ponte, The Hydrodynamics of Astrophysical Jets: scaled Experiments and numerical Simulations, Submitted to Journal of Astronomy and Astrophysics, January 2013.

[78] Belan M., Mirzaei M., De Ponte S., Tordella D., An experimental setup for visualizations and measurements on free hypersonic jets, EPJ Web of Conferences 25, 01056, 2012.